University of Alberta

FACTOR ANALYSIS WITH PRIOR INFORMATION - APPLICATION TO DYNAMIC PET IMAGING

by

Dong-Chang Lee

A thesis submitted to the Faculty of Graduate Studies and Research
in partial fulfillment of the requirements for the degree of

Master of Science
in
Medical Physics

Department of Oncology

Spring 2012
Edmonton, Alberta

Abstract

The conventional region-of-interest (ROI) method to evaluate dynamic Positron Emission Tomography (PET) images can be complex, time consuming, inaccurate (e.g. partial volume effect), and operator-dependent. To overcome these problems, an optimization-based factor analysis of dynamic structures (FADS) technique with *prior* information is proposed and validated using a computer-based simulation. The technique is then applied to eight sets of [^{11}C]-Dihydratetrabenazine (DTBZ) dynamic PET volumes to decompose the datasets into factor volumes (FV's) that represent the striatum and the non-striatum tissues of the brain, and associated factor curves (FC's), describing the uptake and the clearance rates (activity per unit time) of the DTBZ radiopharmaceutical for the two tissue types. The extracted FV's and FC's are used for stratifying the healthy subjects from patients with early Parkinson's disease. In conclusion, the proposed FADS technique has the potential to significantly aid in the review process for evaluating dynamic datasets by clinicians.

Acknowledgements

I am supremely grateful to my supervisors, Prof. Terence A. Riauka for his unflagging support, thoughtful encouragement, and discerning counsel throughout my Master's study at the University of Alberta. His sense of humor, perpetual energy and enthusiasm in research motivated everyone in the department and made the environment very comfortable and exciting place to work. In addition, he was very generous, kind, accessible and always willing to help.

My committee members Prof. Don Robinson and Prof. Hans Jans deserve special thanks for their indispensable guidance and continuous support. In particular, I sincerely enjoyed interacting with Prof. Jans outside as well as inside the classroom. His intellectual curiosity, wisdom, and keen knowledge of life have inspired me to be more optimistic.

I would like to thank Prof. Sandy McEwan, Prof. Gino Fallone, Prof. Sherry Connors and members of the medical physics group for their useful discussion and financial support.

I owe my deepest gratitude to my family for their endless love and support throughout my life; this dissertation simply would not been possible without them. I am indebted to my father, Kyung-Woo Lee, for his love and care. He worked extremely hard to support the family and devoted his life to provide me with the best possible education. He influenced me in every aspect of my life and inspired me to believe that nothing is impossible. It is his vision that brought me here, and I give him all the credits for my success and accomplishments. He, of course, could not have done this by himself– my mother, Young-Hee Yoon was beside him every step of the way. She has sacrificed so much for the family, and I thank her for the everlasting love given to me. She is simply a perfect and truly caring person. I remember many sleepless nights she spent with me during midterms, but I especially miss her delicious dishes! I am proud of my sister, Dong-Gum Lee, for her enthusiasm in life. She gave me countless times of laughter, and cheered me up

when I was going through difficult times. I love you.

Lastly, I am immensely grateful to all those who have supported me in all the many and varied respects as I strove to complete my Master's study at the University of Alberta. Thank you all.

Table of Contents

List of Tables

List of Figures

List of Symbols

$\boldsymbol{a}$	arbitrary vector
$\boldsymbol{A}$	arbitrary matrix
A_1	activity from the factor 1 (see equation 2.36)
A_2	activity from the factor 1 (see equation 2.37)
C_1	single count rate for detector 1
C_2	single count rate for detector 2
D	Accuracy parameter
$\boldsymbol{E}$	[m,n] noise matrix
f	objective function
f_{ls}	least-squares objective function
g	arbitrary function
$\boldsymbol{H}$	[q,n] factor curve matrix
$\boldsymbol{H}^{0}$	initial $\boldsymbol{H}$
$\boldsymbol{H}^{k}$	$\boldsymbol{H}$ at time step k
$\boldsymbol{H}_{opt}$	optimum $\boldsymbol{H}$
i	*voxel*

$\boldsymbol{I}$ [n,n] identity matrix

j factor

k iteration step

l_i lower bound for x_i

m number of voxels (equal to $\frac{M \times M \times N}{r \times r}$)

m_1 number of voxels (equal to $M \times M \times N$)

m_2 arbitrary number of voxels

m^k positive integer (1,2,3,...)

M number of columns or rows in a PET image

n number of time frames

n_2 arbitrary number of rows

N number of PET slices

P projection operator

q number of factors

$r \times r$ size of VA

$\boldsymbol{R}$ [n,n] rotational matrix

$\boldsymbol{s}$ [n,n] singular value matrix

$\boldsymbol{s'}$ noise-suppressed $\boldsymbol{s}$

t discrete time index

T number of time frames

$^{\mathbf{T}}$ transpose operator

$\boldsymbol{tTAC}$ $[q,n]$ true time activity curve matrix

$\boldsymbol{u}$ left eigenvector matrix

u_i upper bound for x_i

$\boldsymbol{v}$ right eigenvector matrix

$\boldsymbol{V_0}$ $[M\times M\times N,T]$ noise-reduced dataset

$\boldsymbol{V_0'}$ $[M,M,N,T]$ noise-reduced dataset

$\boldsymbol{V'}$ voxel-averaged $\boldsymbol{V_0'}$ with dimension $[\frac{M}{r}, \frac{M}{r}$,N,T]

$\boldsymbol{V}$ reshaped $\boldsymbol{V'}$ with dimension $[\frac{M\times M\times N}{r\times r}, T]$

$\boldsymbol{W}$ $[m,q]$ factor coefficient matrix

$\boldsymbol{W^0}$ initial $\boldsymbol{W}$

$\boldsymbol{W^k}$ $\boldsymbol{W}$ at time step k

$\boldsymbol{W_{opt}}$ optimum $\boldsymbol{W}$

$\boldsymbol{W_1}$ $[m_1,q]$ factor coefficient matrix

$\boldsymbol{W_1^0}$	initial $\boldsymbol{W_1}$
$\boldsymbol{W_1^k}$	$\boldsymbol{W_1}$ at time step k
$\boldsymbol{x}$	n-dimensional vector
$\boldsymbol{X}$	$[m_2,n_2]$ data matrix
$\boldsymbol{x^k}$	$\boldsymbol{x}$ at time step k
α_k	step size at time step k
α_H^0	initial step size for $\boldsymbol{H}$
α_w^0	initial step size for $\boldsymbol{W}$
β	arbitrary constant between 0 and 1
δ	global tolerance level
ϵ	tolerance level
σ	arbitrary constant between 0 and 1
∇	gradient operator
∇^2	laplacian operator
$\|\|C\|\|$	Frobenius norm of C

Abbreviations

ANLS	Alternating Nonnegative Least-Squares
AS	Apex-Seeking
Bq	Becquerel
CT	Computed Tomography
Ce	Cerium
DTBZ	Dihydrotetrabenazine
FADS	Factor Analysis of Dynamic Structure
FAZA	Fluoroazomycin arabinoside
FC's	Factor Curves
FDG	Fluorodeoxyglucose
FI's	Factor Images
FLT	Fluorothymidine
FV's	Factor Volumes
GUI	Graphical User Interface
LOR	Line of Response
LS	Least-squares

LSO	Lutetium Oxyorthosilicate
LYSO	Lutetium Yttrium Oxyorthosilicate
MBq	Mega -Becquerel
NMF	Nonnegative Matrix Factorization
NaI	Sodium Iodide
NECR	Noise Equivalent Count Rate
PCA	Principle Component Analysis
PD	Parkinson's Disease
PET	Positron Emission Tomography
PGM	Projected Gradient Method
PVE	Partial Volume Effect
Rn	Random
ROI	Region-of-Interest
Sc	Scatter
SI	International System of Units
SNR	Signal-to-Noise Ratio
SVD	Singular Value Decomposition

TA	Time-averaged
TAC's	Time Activity Curves
Tl	Thallium
Tr	True
VA	Voxel-averaging
eV	electron-Volt

Chapter 1
Introduction

1.1 Thesis Organization

This thesis is divided into six chapters (with several subsections) and a bibliography. Chapter 1 outlines the organization of this thesis. This thesis begins by introducing a brief history of the field of nuclear medicine and some background that is relevant to this research. Then, the physical and biological properties of radiotracers are introduced, and their clinical applications are discussed. A powerful imaging modality in nuclear medicine, Positron Emission Tomography (PET), is discussed and the concept of static and dynamic PET imaging techniques are introduced. Then, nomenclatures used in this thesis (e.g. an image, volume, and dynamic volume) are defined. The conventional region-of-interest (ROI) method for analyzing static/dynamic PET images is described and the disadvantages associated with the method are discussed. Then, the concept of time activity curves (TAC's) and its application to the functional imaging is introduced. To improve the quality of analysis and to reduce the problems associated with the traditional ROI approach, factor analysis of dynamic structure (FADS) is proposed as a possible solution. A brief introduction of FADS and the key concepts, like factor volumes (FV's) and factor curves (FC's), are introduced and the drawbacks of the standard FADS technique are discussed.

Chapter 2 starts by introducing a mathematically well-known data decomposition technique - singular value decomposition (SVD) - and its application to FADS (i.e. noise reduction and estimating the number of factors present in the dynamic dataset). The SVD technique is extensively used throughout this thesis for the data preprocessing and for estimating the number of factors in the dynamic dataset. In Chapter 3, various numerical simulations are carried out to emphasize the importance of the SVD technique in this work. The concept of nonnegative matrix fac-

torization (NMF) is introduced and its relation to FADS is discussed. Then, two well-known optimization techniques - projected gradient method (PGM) and alternating non-negative least-squares (ANLS) - are introduced and used to describe the NMF technique in detail. The proposed FADS technique, which minimizes the drawbacks of the standard FADS technique, is explained by a step-by-step procedure of the NMF technique with *priori* information. The remainder of Chapter 2 describes different methods used to investigate various factors affecting the SVD and FADS solutions.

In Chapter 3, simulation studies are preformed to investigate the effects of various factors on the SVD and FADS solution (by the proposed FADS technique) using three sets of three-compartment (tissue-specific) models. These factors include signal-to-noise ratio (SNR), shape of underlying kinetics, size of voxel-averaging (VA), and partial volume effect (PVE). The effects of prior information on the FADS solution (i.e. accuracy and convergence rate) are also examined.

In Chapter 4, the proposed FADS technique is applied to eight [^{11}C]-Dihydrotetrabenazine (DTBZ) dynamic PET datasets in order to obtain FV's (i.e. striatum and non-striatum tissues) and associated FC's for each subject's dataset. DTBZ is a positron emitting radiopharmaceutical and is developed to detect patients with early Parkinson's disease (PD) by targeting the dopamine receptors in the mid-region of the brain (e.g. nigrostriatal region). Based on the extracted FV's and FC's from each subject's dataset, in-house developed, factor-based metric is computed to stratify healthy subjects from early PD patients. For the ease of visualizing and comparing the extracted FV's against the original time-averaged (TA) volumes, a MATLAB^{TM}-based graphical user interface (GUI) is developed by the author. The GUI displays the time-averaged slice and the corresponding factor images from the FV's with the option of viewing the time frames of the selected slice. The results of the factor-based metric are in excellent agreement with the diagnostic results by the physicians for the eight subjects.

Chapter 5 summarizes the effects of aforementioned factors on the SVD and FADS solutions. In particular, the effects of prior information and of estimating the proper factor number (q) are emphasized. The advantages and disadvantages of the proposed FADS technique against the other techniques are briefly discussed.

In Chapter 6, conclusions of this work are given with possible future directions.

1.2 Introduction to Nuclear Medicine

Nuclear medicine is a branch of medicine that uses radionuclides (or radioactive atoms) in the diagnosis and treatment of disease. The development of this field goes back to the early 1900s when Hungarian-Danish chemist Georg Von Hevesey first suggested the tracer principle - one can rely on the decay process of a radioactive substance as an indicator to trace the movement of the radionuclide in a living organism [1]. He later validated his tracer principle using rabbits and showed the movement of a radioactive source (Radium-D) through the digestive tract and into the bones. He was awarded the Nobel Prize in chemistry for his work in 1943 and laid the foundation for the field of nuclear medicine. The idea of the tracer principle is extremely valuable to clinicians and researchers because it provides non-invasive way to obtain functional information about the underlying physiology of organs or structures of interest. The tracer principle has been used to identify various types of disease and some examples include: detection of nonmaligant bone lesions [2]; myocardial perfusion scan for evaluating coronary artery disease and risk of cardiac events [3]; hepatobiliary scan for the detection of gallbladder disease [4]; thyroid scan for evaluating hyperthyroidism [5]; and many other examples. The field of nuclear medicine continues to grow with the development of new technology and the availability of new radiotracers. The field has made significant impact and contributions toward performing medical diagnosis for the various types of diseases.

1.3 Radioactivity and Radiotracers

In nuclear physics, an atom (or element) is defined as the smallest structure that possesses physical and chemical properties. A radionuclide is an unstable atom that undergoes nuclear decay processes such as alpha decay, beta-minus decay, gamma decay, positron emission, or electron capture. It is outside of the scope of this work to define and describe all of the different decay processes but one can find detailed information about these processes in any of the standard nuclear medicine textbooks [6, 7]. A detailed discussion of positron emission is followed in the latter part of this section since positron-emitting radionuclides form the signal for the static/dynamic positron emission tomography (PET) imaging.

Radioactivity (or activity) is known as the rate at which given sample of radionuclide disintegrates per unit time. The commonly used *International System of Units* (SI) for radioactivity is Becquerel (Bq), named after Henri Becquerel who discovered mysterious ray: ("emanations" of the uranium) in early 1896, and it is equivalent to 1dps (disintegration per second). Radioactive decay is a random process (with statistical fluctuation) and follows Poisson statistics [8]. Macroscopically speaking, the decay process of a sample of radioactive material depends on the radionuclide's decay constant λ and is given by,

$$A(t) = A_0 e^{-\lambda t}, \tag{1.1}$$

where $A(t)$ and A_0 are the amount of radioactivity at time t and at time t=0, respectively. By defining, the half-life ($t_{1/2}$) as the time it takes for the original radioactivity of a sample to decrease by exactly one-half, one can write the relationship between the half-life and the decay constant as,

$$\lambda = \frac{0.693}{t_{1/2}}. \tag{1.2}$$

Equation 1.1 and 1.2 are useful in the later section of this Chapter for determining the decay correction factor for dynamic images produced by PET imaging.

Radiation emitted by the radionuclide can be largely divided into photons and charged particles. A photon is a packet or a quantum of electro-magnetic radiation that is massless and travels at the speed of light. X-rays and gamma rays are classified as photons with energy greater than 100 electron-Volt (eV) [6]. When a photon interacts with tissues it produces secondary electrons that deposit energy into tissues. Since it is the electrons that deposit the energy into the tissue, photons are referred to as indirectly ionizing radiation. On the other hand, charged particles (e.g. alpha and beta particles) directly deposit their energy into tissues and the likelihood of a charged particle interacting with tissues is much higher than that of photons interacting with tissues for the same amount of kinetic energy.

The positron is a very important radiation particle employed in nuclear medicine imaging. It is a by-product of proton-rich radionuclides undergoing nuclear decay. Positrons interact with any tissues by electrostatic ionization and lose most of their energy by following a tortuous path until their energies reach a thermal value (a few eV). The positively charged positron will then combine with a nearby electron to produce two (511 keV) annihilation photons (or gamma-rays) at approximately 180° apart. It is important to note that the production site of the annihilation photons is some distance away from the production location of a positron, generally less than a few millimeters.

Positron-emitting radionuclides (e.g. ^{11}C, ^{13}N, ^{18}F, ^{15}O) are combined with various chemical compounds to form different radiopharmaceuticals. Depending on the physical and chemical properties of the radiopharmaceuticals, it is possible to target various tissues and organs of interest for imaging. For example, fluorodeoxyglucose ([^{18}F]-FDG) is a glucose analogue attached to a positron-emitting radionuclide [^{18}F]. Since most tissues regulate glucose uptake in the body, the intensity level of positrons from [^{18}F] can be used to generate a map of glucose uptake. This type of drug is called a metabolic marker and is useful for detecting cancerous tumors since many of them have elevated metabolism (hypermetabolic

tumors) compared to the surrounding normal tissues. As a result, hypermetabolic tumors display increased intensity in PET images. This imaging technique is therefore especially useful for detecting metastatic disease. Another example is [^{11}C]-dihydratetrabenazine (DTBZ), which is developed and used for detecting patients with early Parkinson's disease (PD). It targets dopamine receptors in the mid-region of the brain (i.e. nigrostriatal region). For a diseased subject, the loss of dopaminergic neurons implies that there are smaller number of binding sites for the DTBZ tracer than for a non-diseased subject. Therefore, the uptake of the DTBZ tracer by the dopaminergic neurons for a healthy subject is much higher than that by the dopaminergic neurons for a diseased subject. The difference in the tracer uptake levels between the two groups (e.g. diseased vs. non-diseased) can then be used to distinguish healthy subjects from PD patients. In Chapter 4, eight DTBZ datasets are analyzed using the proposed FADS technique.

1.4 Static/dynamic PET Imaging Overview

Standard PET imaging produces a set of N trans-axial images representing the 3D activity concentration distribution (3D ACD) within the field of view of the scanner (e.g. N=45 for our scanner). In dynamic PET imaging, the 3D ACD is sampled at M successive time points (i.e. M=16 in our case), resulting in M representations of the 3D ACD. Most modern PET scanners are capable of acquiring either static or dynamic datasets. In dynamic PET imaging, the duration of each time point and the number of time points for sampling the PET volumes are carefully chosen after considering the physical and chemical properties of the radiopharmaceutical (e.g. half-life and molecular structure) and biological property of the tissues or organs of interest (i.e. uptake and clearance rates of the radiopharmaceutical). While both imaging techniques produce functional images for the tissues or organs of interest the dynamic imaging technique can provide additional, clinically relevant, information about the underlying physiology as compared to any single observation of the

3D ACD at a single time point. The uptake and clearance rates of the radiopharmaceutical by the organs or tissues of interest are used to diagnose any malfunction of the underlying physiology. For the case of dynamic volumes, the TA PET volume is used to identify and contour the structures of interest using the region-of-interest (ROI) method. Then, these masks are applied to the PET volumes at different time points to obtain the time evolution of the 3D ACD for the structures of interest. Even though the ROI method is a standard technique to obtain TAC's from the dynamic PET dataset there are several disadvantages associated with the technique. In the latter sections of this Chapter, the drawbacks of the ROI method and the possible solutions are discussed.

1.5 Nomenclatures of Images, Volumes, and Dynamic volumes

In a PET study, an image is an intensity distribution map of the radiopharmaceutical in a thin slice of a volume within the field of view of the scanner. A typical (trans-axial) image consists of 144 $\times$ 144 voxels and each isotropic voxel is 4 $\times$ 4 $\times$ 4 mm^3. Thus, each voxel represents the average 3D activity concentration of the radiopharmaceutical in a small (64 mm^3) volume with units of Bq/ml. The PET imaging technique used by our scanner produces 45 slices to represent the scanned volume within the field of view of the scanner. Therefore, identifying organs or tissues under study will often involve working with multiple slices in the PET volume. By sampling the PET volume at M successive time points dynamic PET volumes can be produced. The dynamic PET volumes describe the temporal variation of 3D ACD for the imaged volume and may provide additional clinical information compared to a PET volume imaged at a single time point. The time evolution of the 3D ACD (or time activity curve) for the tissues or organs of interest provides (extremely useful) functional information about the underlying physiology. The downside of these dynamic volumes is the large amount of data produced for analysis. For example, the data size of dynamic PET dataset with 20 TF's and 45 slices

is 20×45 images and the image reviewer needs to analyze these 900 images.

1.6 Positron Emission Tomography

It is out of scope for this study to describe the PET imaging technique and system in full detail, however; the principle and key ideas of the technique and the system are presented in this section. Detailed information about the PET imaging system can be found in any standard nuclear medicine textbook [6, 7]. While various imaging techniques are available, PET is important imaging modality and is becoming increasingly popular in the field of nuclear medicine. The PET imaging technique is emission-based and uses positron-emitting radionuclides (i.e. ^{11}C, ^{13}N, ^{18}F, ^{15}O, etc). It is based on the coincidence detection (several nano-seconds) of two 511-keV annihilation photons, generated when a positron combines with a nearby electron. A positron is positively charged electron and is produced when a proton-rich radionuclide undergoes a decay. During this process, a proton in the nucleus is converted into a neutron, a positron, and a neutrino. Excess energy in the nucleus is shared as kinetic energy by the positron and the neutrino.

To image different tissues or organs in the body, radionuclides are attached to various chemical compounds to target specific cells or tissues. For example, [^{11}C]-Dihydrotetrabenazine (DTBZ) radiopharmaceutical - used in this study - targets dopaminergic neurons in the substantia nigra of a brain (or striatum tissues). Other commonly used radionuclide for the PET imaging is ^{18}F and some examples of radiopharmaceuticals using ^{18}F include [^{18}F]-fluorodeoxyglucose (FDG) for measuring glucose uptake in the body, [^{18}F]-flurothymidine (FLT) for targeting actively proliferating cells, and [^{18}F]-fluoroazomycin arabinoside (FAZA) for targeting oxygen deprived cells (tumor hypoxia). The physical half-lives for ^{11}C and ^{18}F are 20 minutes and 110 minutes, respectively. The physical half-life of the radiopharmaceutical and the biological half-life for the tissues or organs of interest should be carefully considered when determining the number of time frames (TF) and the

duration of each TF for generating dynamic PET volumes.

PET images suffer from the low image quality (i.e. low spatial resolution) due to four well-known physical phenomena: first, a positron with kinetic energy goes through tortuous path until its energy becomes at thermal level and then combines with a nearby electron to generate two 511 keV annihilaton photons. Thus, the production site of the two photons are a few millimeters away from where the positron is actually created; second, the PET imaging technique relies on the coincidence detection of the two annihilation photons that are 180° apart. However, these paired photons are not exactly colinear (e.g. $180° \pm 0.25°$) due to small residual momentum of the positron at the time of the annihilation; third, the detector size (e.g. area of crystal face) greatly affects the spatial resolution of an image. Higher spatial resolution can be achieve by reducing the detector size (e.g. length of detector face) up to several millimeters. Further reducing the detector size will be meaningless due to the positron range and the non-colinearity of the annihilation photons; Fourth, the probability of annihilation photons interacting with two or more neighboring detectors decreases as the detector size gets small. This increases the spatial resolution in an image by introducing an error (several millimeters) in the localization of the detector pair responsible for the annihilation event. Another factor that can degrade the spatial resolution of an image is a type of filter used with a reconstruction algorithm. If the filter has a high cutoff frequency then it introduces noise in the image. Aforementioned factors contribute to the inaccuracy in the measured sinograms that are used for reconstructing static and/or dynamic PET images. This is the reason for the PET imaging technique to use relatively larger voxel size of 4^3 mm^3, compared to other imaging modalities such as Magnetic Resonance Imaging (typically 1 mm^3) or Computed Tomography (1.44^3 mm^3). By reducing the voxel size to 1 mm^3 from 64 mm^3 the SNR of the voxel decreases by a factor of 8 ($= \sqrt[2]{64}$). The manufacturer determined the optimum size of a voxel for our PET scanner is 4^3 mm^3 and the same voxel size is used for this study.

The fundamental idea behind the PET imaging technique is the coincidence detection (within several nano-seconds) of the two 511 keV photons from the same annihilation event. Unfortunately, there are multiple pathways that the annihilation photons can undergo before getting detected and this has an effect of reducing the signal-to-noise (SNR) in an image (or reduction of contrast in an image). Multiple scenarios can occur after the creation of the annihilation photons: they can reach the opposite detectors without being scattered (true event); one or both photons can undergo scattering before getting detected (scattered event); photons from the two separate annihilation events reach a detector pair (random event); both photons get absorbed (no event) or only one of them reaches the detector (single event); Thus, measured count rates consist of true (Tr), scattered (Sc), and random (Rn) count rates. Various methods to correct for random and scattered count rates can be found in the following nuclear medicine textbook [9, 10]. The noise equivalent count rate ($NECR$) is used to measure the image quality and is proportional to the SNR of the reconstructed images. It is defined as,

$$NECR = \frac{Tr^2}{Tr + Sc + Rn}. \tag{1.3}$$

The SNR's of the images increase by reducing the scattered and random count rates while maintaining the true count rate. The random count rate (R) is proportional to $\tau C_1 C_2$ where τ is the coincidence time window (in nan-seconds) and C_1 and C_2 are single count rates from a paired detector. The R grows exponentially with the increased amount of radioactive sample used in the study. Thus, it is critical to determine the optimum dosage of radionuclide to avoid excessive random count rate.

PET is a state-of-the-art system with sophisticated electronic components. The most important and complex components of the PET system is the detector system and it consists of several rings of small crystals (optically) coupled with photomultiplier tubes. The crystals convert a high energy gamma-ray into numerous lower

energy light photons (scintillation process). The crystals are doped with small amounts of impurities to increase the light output in response to the energy deposited (to the crystals) by the incident gamma-rays. The most widely used scintillation crystal for gamma-ray detection is sodium iodide (NaI) doped with thallium (Tl). However, modern PET systems employ LSO crystals doped with Ce or LYSO crystals doped with Ce because of the following reasons: shorter scintillation decay time (reduction in detector dead time); high atomic number and high density (high stopping power for the detector and high linear attenuation coefficient for 511keV photons); high yield of light output per keV of photon energy (higher light yield will improve the energy resolution of the detector); good energy resolution of the detector. The interaction between gamma-rays and crystals is a complex process but it can be briefly described as follows. After the crystal absorbs the energy imparted by the gamma-ray its electrons are temporarily left in an excited state. Shortly after the excitation, the electrons begin to return to their ground state and some of the excitation energy is released as light photons. These light photons are then detected and amplified by photomultiplier tubes to produce electric signals. These signals are further amplified and sent to pulse height analyzer for discriminating photons with energy outside of the specified energy window. For instance, scattered photons will have lower energy then 511 keV. In some cases, more than two photons can be absorbed by the crystal simultaneously and the corresponding energy will be higher than 511 keV. However, it is possible for photons from multiple annihilation events to reach the detector simultaneously and the sum of their energy fall within the specified energy window. Since there is no way to discriminate such events from the true events they form as a part of signal and reduces the SNR of the image.

When the paired 511 keV photons reach the two “opposite” detectors within the coincidence time window (i.e. electronic collimation is used to improve the detector sensitivity), the system considers that the two photons are from the same annihilation event (see figure 1.1). The event is then said to have occurred somewhere along

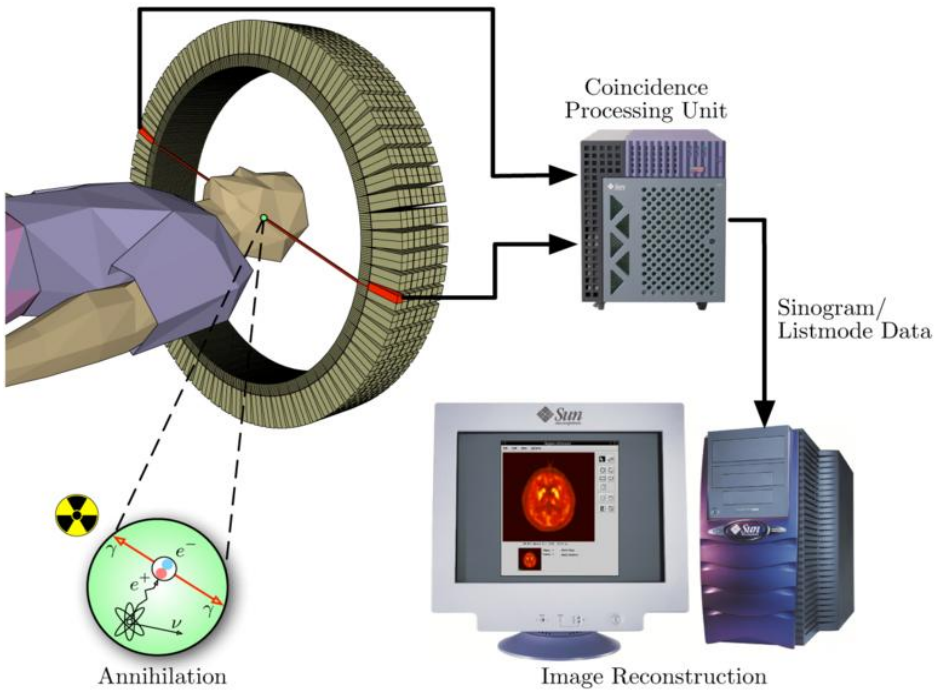

http://en.wikipedia.org/wiki/File:PET-schema.png

Figure 1.1. This figure illustrates a simplified data acquisition process for the Positron Emission Tomography system.

an imaginary line called the line of response (LOR) that connects the two "opposite" detectors. Errors in creating the LOR's (e.g. aforementioned factors in this section) will decrease the image quality (e.g. lower spatial resolution and lower image contrast). Since photons travel different thickness of tissues in the body to reach the detector pair each LOR is applied with the (photon) attenuation correction. These LOR's are binned in a special geometric fashion to create sinograms. A sinogram is function of radius (distance measured from the center of the bore) and angle (measured clockwise from the axis perpendicular to the coronal plane). Thus, each pixel point in the sinogram corresponds to the signal intensity (or measured activity) along a LOR. Modern scanners are capable of producing sinograms in both

2-dimensional and 3-dimensional modes. Each detector ring produces a sinogram in the 2D mode whereas non-redundant detector pair generates sinogram in the 3D mode. Hence, the detector sensitivity is significantly improved at the cost of introducing higher number of scattered and random events in the 3D mode. These sinograms are then used to construct 3-dimensional PET images using an iterative reconstruction algorithm [11, 12].

1.7 Region-of-Interest Analysis and Time Activity Curve

The conventional ROI method to evaluate static or dynamic PET images can be complex, very time consuming, and operator-dependent. In this approach, the operator first has to identify the organs or tissues of interest (in 3-dimensions) by visual inspection and then carefully create masks (i.e. ROI's) for the slices containing the structures of interest. In the case of dynamic PET imaging, the TA PET volume is used for identifying structures and creating the masks. These masks are then applied to the individual PET volumes at different TF's to obtain a TAC's (temporal variation of 3D ACD from a voxel or group of voxels). For dynamic PET images, it is difficult for clinicians to interpret the subtle changes and/or trends in the 3D ACD as a function of time due to the vast amount of information generated by the imaging technique. More importantly, the 3D ACD in a voxel may be a linear combination of activities from multiple physiological structures due to the finite voxel size of the PET scanner (i.e. isotropic 64 mm^3 voxel). This partial volume effect (PVE) and the subjectiveness of the ROI method make the manual approach less attractive for quantitative analysis. To overcome these problems, an optimization-based FADS technique is proposed in the next section. The proposed technique minimizes the PVE and is semi-automatic, computationally robust, and operator independent. As a result, the technique can significantly aid the review process and improve the quality of medical diagnosis.

1.8 Factor Volumes and Factor Curves

In nuclear medicine, the conventional ROI method, which requires manual identification of structures, is often used to understand the kinetics of underlying physiology or to identify physiological structures. To simplify the analysis and improve the quality of the analysis, Barber [13] introduced a principle-component based factor analysis technique that automatically decomposes the dynamic dataset into q factor curves (FC's) and factor images (FI's) such that the TAC of any voxel in the dataset can be represented by the linear superposition of q FC's with appropriate coefficients. These coefficients are then reshaped to form factor images (or volumes) that represent the underlying physiology and this technique can minimize the partial volume effect. His technique has been investigated by several authors [14, 15].

This technique assumes that noise in the dataset follows the Gaussian distribution and the structure defined by a factor image is homogeneous and the shapes of normalized TAC's (by the maximum value of each TAC) are all same within the structure. The number of factors in the dynamic dataset is denoted by q and must be determined prior to performing factor analysis. His technique is based on the principle component analysis (PCA) of the dynamic image data and application of the oblique rotation to obtain physiologically meaningful (nonnegative) FC's and FI's. The factor model does not make any assumption about the shapes of the FC's. Barber applied his technique to dynamic (gamma-camera) brain studies and extracted three factors that represent the arterial, venous and tissue components. His method was inspired by Schmidlin [16] who used principle components analysis to characterize the TAC's within the regions of the renogram (a dynamic renal study) by their rise and decay times. Paola et al [17] describes Barber's method in detail - especially the apex-searching algorithm where an apex corresponds to a factor curve - and Houston [18] investigated the effect of apex-finding errors on factor images. Barber's algorithm is an iterative method with relatively fast convergence but has a major drawback - the solution is not mathematically unique [18, 19, 20, 21] and this

has been a stumbling block for several years. To reduce the ambiguity and increase the accuracy of the solution, Nijran and Barber [22, 23] incorporated prior information to the factor analysis by providing exact temporal and spatial information of the known physiological structures. Unfortunately, this information is not available for every dataset and can be only applied to special cases. Later, Buvat *et al* [24] reported a newly improved way of incorporating (less-extensive) prior knowledge into the FADS technique. Detailed discussion of the non-uniqueness problem is included in the latter part of this section and in Chapter 2.

The idea of data decomposition is not new and various types of decomposition techniques are available (e.g. principle component analysis and singular value decomposition) [25, 26, 27]. However, such techniques alone are insufficient for the FADS analysis (e.g. finding factor curves and images) because they produce negative values as a part of their solutions. Since radioactivity cannot be negative, the solutions from these techniques are not in general physically meaningful. To comply with the factor model (refer to equation 2.4), factor curves and factor coefficients have to be non-negative. Unfortunately, non-negativity alone does not guarantee a unique solution [22, 23, 28] and additional constraints are typically required to reduce the ambiguities in the solution.

Different iterative methods have been developed for FADS analysis and they can be largely divided into two groups: apex-seeking (AS) algorithm and optimization-based least-squares (LS) method. Sitek *et al* [29] compared the two methods - that use completely different algorithms - using computer simulations, and 99^mTc-Teboroxime experimental canine and patient studies. He utilized *a priori* information to constrain the solution space (in order to obtain a unique solution) and showed that the results produced by the two techniques are very similar. The importance of appropriate constraints cannot be overemphasized as they heavily influence the quality of the solutions [29, 30]. Nakamura *et al* [31] and Sitek *et al* [32] applied the maximum entropy method [33, 34] to obtain unique solutions for the FADS

analysis. In their optimization-based techniques, weighted entropy terms consisting of factor curves and factor images, are subtracted from their objective functions. Maximizing the entropy terms can minimize the ambiguities of the FADS solution. The main problem of such a technique is the pre-determination of the weighting factor, which can vary between different datasets and with varying SNR's, for the entropy term.

It is important to remember that the unique solution is no guarantee for finding the true FC's and FV's (or true underlying physiological structures). So, it is crucial for the analyst to compare the factor analysis solutions with the known information about the dataset and to use common sense before making any decisions based on the FADS results. Depending on the shapes of TAC's in the dynamic dataset, the non-uniqueness effects can be significant or be nearly non-existent [28]. Nevertheless, several authors have successfully applied the FADS techniques (with various types of constraints) to different kinds of dynamic image data. Schiepers *et al* [35] implemented Barber's technique [13] without any additional constraint and successfully identified normal and abnormal lobes of the prostate gland from nine prostate cancer patients. They reported that the extracted FC's - which can be used for kinetic modeling - were comparable to the image-derived TAC's by the conventional ROI-based method. His technique has been successfully applied to other clinical areas such as renal studies [36, 37, 38], (gated) cardiac studies [39, 40] and abnormalities in the thyroid uptake studies [41]. In renal and cardiac studies, it is particularly difficult to perform the traditional ROI analysis because of the PVE's (due to voxels containing multiple tissue or kinetic information as a result of the finite spatial resolution of the scanner) and spillover effects (due to lung, heart or patient motions) in the datasets. Another possible application of the FADS technique is reducing noise in dynamic datasets [42].

After the successful application of FADS to human studies, various authors began to explore the feasibility of the technique in small animal (mouse, rat, and dog)

studies [43, 44, 45, 46]. Due to their small size and the limited spatial resolution of the micro-PET scanner (e.g. partial volume and spillover effects are much more prominent), the standard ROI method is not only harder to implement but also gives less accurate and reliable information about underlying tracer kinetics. Since small animal studies often involve the cardiac region where heart muscle (or myocardium) surrounds the left ventricle (or input arterial function) and is in periodic motion, the ROI method simply cannot extract accurate arterial input function (for quantitative analysis) [45, 46]. The manual extraction of blood samples is invasive and can be difficult to perform due to small amount of available blood in the animal. Instead of collecting multiple blood samples, Wu *et al* [43] showed that a single blood sample constraint could be applied to FADS for more accurate extraction of (left ventricle) arterial input function. In some cases, FADS works very well while in other cases, FADS fails to extract correct input functions with only the nonnegative constraint. This can be due to very large overlap of structures and/or low SNR. It is important to remember that FADS cannot separate (physiological) structures if they overlap completely. For FADS to work there must be enough voxels with "pure" functions or underlying kinetics [47]. The presence of noise in the dataset can play a major role in the FADS result and the effect of noise is extensively studied in Chapter 3.

More recently, optimization-based factor analysis techniques with uniqueness constraints (to obtain unique solutions) have become popular [28, 48, 49]. The advantage of optimization-based methods is that different types of constraints are readily available and can be easily incorporated into the method. Sitek *et al* [28] provides detailed discussion of estimating and embedding the uniqueness term to the objective function. He achieves the unique solution (i.e. a factor volume that represents a single physiological structure) by minimizing the overlaps between structures defined by factor volumes. The downside of such a technique is the estimation of a penalty parameter (which is a part of the uniqueness term) that depends on the noise level in the dataset and the type of dataset. He also claims that

his non-uniqueness correction either works, or does not work. These facts make the technique less quantitative and less desirable.

In this thesis, the optimization-based FADS technique is proposed in the framework of the nonnegative matrix factorization. The proposed techniques is semi-automatic proces and uses prior information about the known physiological structures (i.e. sample TAC's from the q structures by the standard ROI method) to warm start the optimization. The sample TAC's are rough estimate and can contain mixed tissue information. Our technique does not require any blood sampling or pre-determination of penalty constants. By providing a good starting point for the optimization, the technique significantly reduces the number of possible solutions and the resulting solution is much closer to the true solution in comparison to the solution without the prior information (see Chapter 3). The technique is computationally robust and operator-independent. It requires the minimum amount of work and most importantly, it can be used for the quantitative analysis. The technique is highly desirable for analyzing a sequence of medical images and has the potential to greatly improve the quality of medical diagnosis.

Chapter 2

Methods and Materials

2.1 Method

2.1.1 Singular Value Decomposition (SVD)

Singular value decomposition (SVD) is a powerful mathematical technique for decomposing a data matrix into two (left and right) orthogonal bases and singular values. The data matrix decomposition can be done by various techniques (i.e. PCA, SVD, LU decomposition, Gaussian elimination, cluster analysis) but SVD, which is very efficient and has nice mathematical properties (see below), is known to handle singular (or ill-conditioned) matrices much better than the other techniques [26]. SVD is particularly useful for this study: first, it estimates the number (q) of factors (or tissue-specific structures) in the dataset (q is a pre-requisite for the FADS); and second, it is used to reduce the amount of noise present in the dataset. As discussed in Chapter 3, the accurate estimation of q cannot be over-emphasized as it is crucial for the successful application of FADS. The SVD technique is more sensitive in finding the number of (hidden) factors from the noisy dataset than the PCA technique (see Chapter 3).

Suppose we have an [m_2,$n2_2$] data matrix $\mathbf{X}$ that represents a sequence of dynamic medical images such that m_2 and n_2 describe the total number of voxels and time frames, respectively. To estimate the number of pure functions (or underlying kinetics) in the dataset, SVD can be applied to the dynamic dataset,

$$\mathbf{X} = \begin{vmatrix} \mathbf{X}_{11} & \cdots & \mathbf{X}_{1n_2} \\ \vdots & \ddots & \vdots \\ \mathbf{X}_{m_2 1} & \cdots & \mathbf{X}_{m_2 n_2} \end{vmatrix}.$$

$$\mathbf{X} = \mathbf{u} \cdot \mathbf{s} \cdot \mathbf{v}^T, \tag{2.1}$$

where **u**, **s** and **v** are [m_2,n_2], [n_2,n_2] and [n_2,n_2] matrices, and ^{T} denotes the transpose operator. The columns of **u** and **v** denote left and right eigenvectors, respectively. The diagonal matrix **s** contains information about the contribution (or importance) of the left eigenvectors (columns of **u**). This can be seen by projecting the data matrix **X** onto the right orthogonal bases **v** as follow,

$$\mathbf{X}\cdot\mathbf{v} = \mathbf{u}\cdot\mathbf{s}, \tag{2.2}$$

since $\mathbf{v}^T \cdot \mathbf{v} = \mathbf{I}$ where **I** is identity matrix. Notice that k^{th} column ($k = 1, \cdots, n$) of **u** is multiplied by the k^{th} diagonal singular value of **s** (e.g. weighting factor for k^{th} principle image or volume). This means that n_2 resulting column vectors in the right side of equation 2.2 represent n_2 principle images or volumes (i.e. uncorrelated images or volumes). Generally speaking, the eigenvectors corresponding to small singular values are considered as noise and can be eliminated from the dataset. The noise contribution can be reduced by simply replacing small singular values in **s** of equation 2.2 by zeros and re-projecting both sides of the equation by $\mathbf{v}^T$. From the orthogonality condition of **v**, the noise reduced data matrix $\mathbf{X}'$ can be written as,

$$\mathbf{X}' = \mathbf{u}\cdot\mathbf{s}'\cdot\mathbf{v}^T, \tag{2.3}$$

where $\mathbf{s}'$ is the [n_2,n_2] diagonal matrix after replacing low singular values in **s** with zeros. In the later part of this section a direct application of the SVD technique to a dynamic sequence of medical images is provided. Detailed discussion of the SVD and its numerical algorithms can be found in the book of "Numerical Recipes in C" [26].

For future reference, **V** is used to describe the dynamic image data instead of **X**. Both **V** and **V**' represent the same noise-reduced (by the SVD technique) dataset. The former is 2-dimensional matrix (i.e. $[\frac{M\times M\times N}{r\times r}, T]$) and the latter is 4-dimensional dataset (e.g. $[\frac{M}{r}, \frac{M}{r}, N, T]$).

2.1.2 Factor Model: Least Squares Approach

Factor analysis of dynamic structures (FADS) is extremely useful mathematical technique for decomposing complex dynamic medical images into factors that represent the "pure" underlying kinetics (FC's) and associated physiological structures (FV's) [17, 22]. It has the potential to significantly aid the review process (by clinicians) and thus improve the quality of medical diagnosis. The key assumption of the factor model is that the TAC of a given voxel (from the noise-free dataset) can be represented by a linear combination of q FC's with appropriate coefficients. These coefficients are then used to generate factor images or volumes - that represent the physiological structures. Before the FADS technique can be applied to the dataset, the appropriate factor number q must be determined from the dataset.

Let the [m,n] data matrix $\mathbf{V}$ represents a dynamic sequence of medical images such that values in each row of $\mathbf{V}$ represent TAC. Under the assumption of the factor model, V_{it} (3D ACD of i^{th} voxel at t^{th} TF) can be written as [28, 49],

$$V_{it} = \sum_{j=1}^{q} W_{ij} H_{jt} + E_{it}, \tag{2.4}$$

where q is the total number of factors in the dataset and E_{it} is the noise in i^{th} voxel at t^{th} TF. $\mathbf{W}$ and $\mathbf{H}$ are [m,q] factor coefficient and [q,n] factor curve matrices, respectively. Then, each column of $\mathbf{W}$ and each row of $\mathbf{H}$ represent FV's and associated FC's, respectively. If we assume that the noise in the dataset $\mathbf{V}$ follows a Gaussian distribution then the least-squares method provides the optimum solution by minimizing the least squares error (see equation 2.4). The least-squares objective (f_{ls}) is given by,

$$f_{ls}(\mathbf{W}', \mathbf{H}') = \frac{1}{2} \sum_{i=1}^{m} \sum_{t=1}^{n} (\sum_{j=1}^{q} W'_{ij} H'_{jt} - V_{it})^2, \tag{2.5}$$

where $\mathbf{W}'$ and $\mathbf{H}'$ are the least-square solutions. For the solutions to be physically meaningful, the elements of $\mathbf{W}'$ and $\mathbf{H}'$ matrices are forced to be nonnegative (e.g.

TAC's cannot be negative). Two popular methods (iterative [13] and optimization-based [28]) are commonly used to solve equation 2.5. Depending on the type of method, different ways of implementing non-negativity constraint is used (i.e. penalty- [48] or iterative-methods [49]).

As previously mentioned, the main drawback of FADS technique is that its solution is not mathematically unique, which can be seen from the following equations:

$$\mathbf{V} \cong \mathbf{WH}, \tag{2.6}$$

$$\mathbf{WH} = (\mathbf{WR}^{-1})(\mathbf{RH}), \tag{2.7}$$

where $\mathbf{R}$ is [n,n] rotational matrix. As long as $\mathbf{R}$ is chosen such that ($\mathbf{WR}^{-1}$) and ($\mathbf{RH}$) satisfy the non-negativity constraint, it is also a suitable solution for equation 2.6. Depending on the type of dataset and size of $\mathbf{R}$, it is sometimes quite difficult to find a rotational matrix ($\mathbf{R}$) that satisfies the non-negativity constraint. For example, principle component-based factor analysis [13] initially produces factor curves ($\mathbf{H}$) that are orthogonal to each other. As a result, elements of both $\mathbf{W}$ and $\mathbf{H}$ include negative values, and so the solution is not physically meaningful. To obtain non-negativity in the solution, an oblique rotation (e.g. similar to $\mathbf{R}$ and $\mathbf{R}^{-1}$) must be applied to $\mathbf{W}$ and $\mathbf{H}$. It is, however, impossible to find such rotational matrix in some cases, which led to the development of optimization-based FADS [28, 48].

Equation 2.7 clearly shows the possibility of having more than one solution. This is an inherent limitation of FADS. Such a problem has been recognized for years and various investigators have applied different techniques (e.g. blood sampling, maximum entropy method, minimization of overlap between structures defined by factor images) in order to obtain unique solutions. However, such techniques have several disadvantages (i.e. invasive, estimation of parameters that varies with the type of dataset and dependence on the signal to noise ratio) and do not provide practical solutions in many situations (see Section 1.5 of Chapter 1).

On the other hand, the proposed FADS technique - that utilizes prior information (e.g. sample TAC's from the dataset) - is much more practical and can significantly reduce the number of possible solutions. Nevertheless, there is no guarantee that the proposed method will produce a unique solution that represents the true underlying physiology and, in fact, this is true for any other known FADS techniques to date. Nevertheless, the effectiveness of prior information on the FADS solution can be seen from the computer-based simulation study (using digital phantoms) in Chapter 3 and the clinical study in Chapter 4.

The problem of solving equation 2.6 with the non-negativity constraint is essentially the same as performing non-negative matrix factorization (NMF) - a recent method developed by Paatero and Tapper [50] and Lee and Seung [51]. The goal of the NMF is to decompose complex data into parts-based representation for easier understanding and interpretation of the data. There are several advantages to using the NMF instead of the principle component-based FADS (or Barber's technique) for solving equation 2.6. First, the NMF provides a better fit to the data and second, it guarantees to satisfy the non-negativity constraint [50]. Various types of NMF algorithms are available and some of them have greater computational efficiency than others [52, 53]. Hoyer [54] describes a method to implement a sparseness constraint to the basic NMF algorithm for improving parts-based feature extraction of the data. The downside of the technique is that the sparseness coefficient can vary with different types of datasets and the SNR's of the dataset. For our study, the NMF technique proposed by Lin [53] is used with prior information to obtain FC's and FV's that represent the underlying physiology for the organs or tissues of interest.

2.1.3 Alternating Non-negative Least-Squares (ANLS)

Even though there are many existing methods for performing the NMF [52, 55, 56], alternating non-negative least-squares (ANLS) method is worth noting. It uses a

different approach to solve the NMF problem and has very attractive optimization properties [52, 53] (see below). The minimization of equation 2.5 requires partial derivatives from the two "block variables" (**W** and **H**) and the gradients of f_{ls}(**W**,**H**) can be written as [48, 53],

$$\nabla_W f_{ls}(\mathbf{W},\mathbf{H}) = (\mathbf{WH}-\mathbf{V})\mathbf{H}^T, \tag{2.8}$$

$$\nabla_H f_{ls}(\mathbf{W},\mathbf{H}) = \mathbf{W}^T(\mathbf{WH}-\mathbf{V}). \tag{2.9}$$

Notice that $\nabla_W f_{ls}$ and $\nabla_H f_{ls}$ have the same dimension as **W** and **H**.

The main questions concerning any optimization technique are the number of local minima, convergence, algorithm efficiencies, stopping conditions, ability to handle very large datasets. These questions are more prominent for large-scale problems. For example, the typical matrix size of our clinical [^{11}C]-DTBZ dataset (144 $\times$ 144 voxels with 45 slices and 16 TF's) is 233280 $\times$ 16 after applying the 2 $\times$ 2 $\times$ 1 in-plane (or transverse) voxel-averaging technique (see Chapter 4). So, it is very important to use an optimization technique that can address these questions. In optimization theory, convexity is an extremely useful property for the following reasons: the local minimum is the global minimum; the convergence is guaranteed; efficient numerical algorithms exist. Therefore, every effort should be made to convert the problem (see equation 2.5) into the convex problem. Fortunately, the minimization problem becomes a convex problem if the two block variables (**W** and **H**) are treated separately [53, 54] and the ANLS method does exactly that.

Unlike many other optimization techniques, where the two block variables are improved simultaneously, the ANLS method alternatively fixes one block variable while improving the other (e.g. find the optimum **W** for a given **H** and then find the optimum **H** for given **W** at every iteration step). As a result, the ANLS method requires solving two sub-problems (see equation 2.10 and 2.11) at every iteration step instead of solving single optimization problem. Since the technique requires solving two sub-optimization problems at each iteration step with non-negativity

constraint, an efficient numerical algorithm is highly desirable to speed up its convergence. For this reason, the projected gradient method (PGM) [53, 57] is used for solving each sub-problem and this method is discussed in the following section.

The goal of the ANLS algorithm is to find **W** and **H** that minimize the least square error given by equation 2.5 under the non-negativity constraint (to obtain physically meaningful solution). The algorithm can be described as,

1. Initialize $\mathbf{W}^0$ and $\mathbf{H}^0$ such that $W_{ij}^0 \geq 0$ and $H_{jt}^0 \geq 0$ for all i, j and t.

2. For k = 0,1,2,$\cdots$

$$\text{find } \mathbf{W}^{k+1} \text{ such that } f_{ls}(\mathbf{W}^{k+1}, \mathbf{H}^k) \leq f_{ls}(\mathbf{W}^k, \mathbf{H}^k), \tag{2.10}$$

$$\text{find } \mathbf{H}^{k+1} \text{ such that } f_{ls}(\mathbf{W}^{k+1}, \mathbf{H}^{k+1}) \leq f_{ls}(\mathbf{W}^{k+1}, \mathbf{H}^k), \tag{2.11}$$

where k is a discrete time index. Initial starting points for $\mathbf{W}^0$ and $\mathbf{H}^0$ can include negative elements but the solution converges faster by restricting the solution space to be non-negative. The ordering of equation 2.10 and 2.11 is important in our case because the prior information (or sample TAC's) is used to produce starting point for **H**. By the convexity of the problem, the improved **W** (or factor coefficient matrix) in equation 2.10 is then good starting point for improving **H** in equation 2.11. The algorithm continues to iterate until predefined stopping condition is met. The PGM is used to solve equation 2.10 and 2.11. It is computationally efficient and allows the non-negativity constraint to be easily applied to the solution.

In optimization theory, a convex problem guarantees finding the global minimum. Our NMF problem consists of not one, but two convex problems, and so the NMF solution (by the ANLS method) does not guarantee the global minimum. It is, however, advantageous to use the ANLS method because prior information provides a good starting point for **H**. Since each sub-problem is a convex, the solution (by equation 2.11) is guaranteed to be a global minimum for given **H**. If **W** and **H**) are improved simultaneously then it will require good starting points for both

W and **H**. Standard ROI method has to be employed to create masks for different physiological structures associated with each of the sample TAC's.

While it is not trivial for us to visualize the error function for equation 2.5 (due to high dimensionality of the problem), it is not difficult to comprehend that the solution by the ANLS method depends on the initial starting point. For example, figure 2.1 shows an image of arbitrary error function g(x,y) where x and y are the two arbitrary axis. From visual inspection, it can clearly be seen that there exists several local minima.

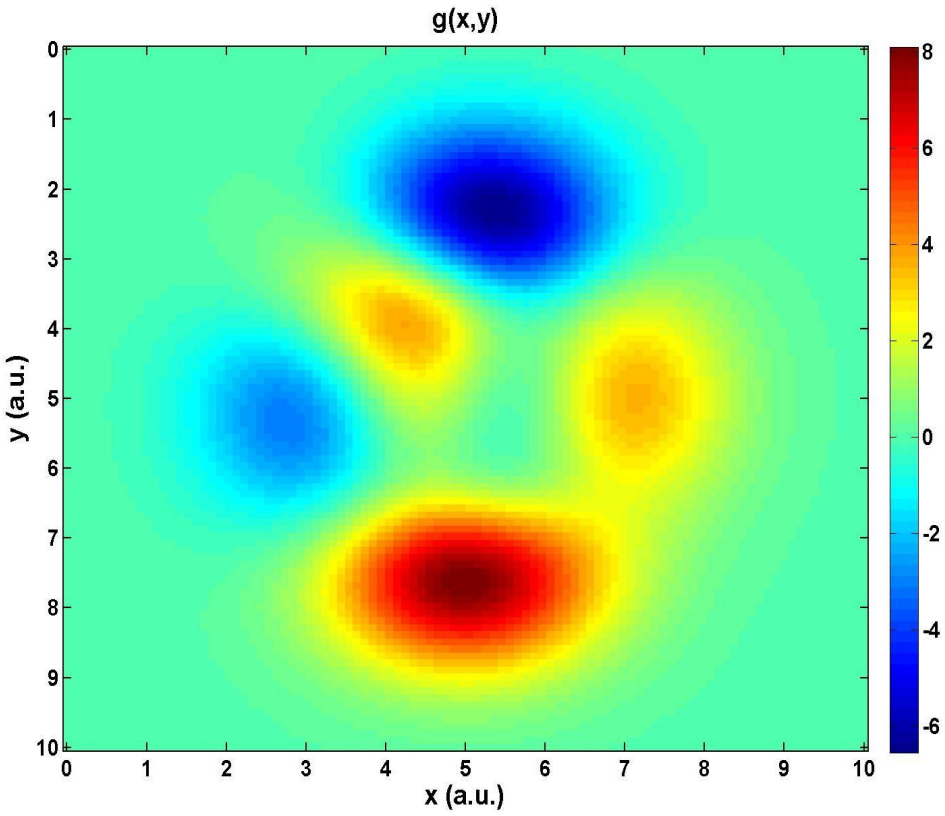

Figure 2.1. This figure shows an image of arbitrary error function g(x,y) with several local minimums. Depending on the starting point, the ANLS method can produce different solutions (see text for details).

Depending on the starting point, the ANLS method produces different solutions.

This example clearly shows the importance of the need for a good starting point. Therefore, prior information is utilized to warm start the optimization in this work. In practice, the presence of noise in the dataset and high dimensionality of the problem makes the problem much more complicated by adding a significantly larger number of local minima to the system. As a result, there is no guarantee that the solution (provided by the ANLS method even with prior information) is the global minimum; nevertheless, a warm start is a good option and provides a solution that is in close proximity to the global minimum. In Chapter 3, the effect of a warm start on the result of FADS is illustrated using a simulation study.

2.1.4 Projected Gradient Method (PGM)

The key to successful FADS depends on the ability to solve sub-problems (equation 2.10 and 2.11) efficiently under the non-negativity constraint. Even though there are many existing methods for solving this type of problem, the projected gradient method (PGM) is particularly useful: first, the method converges very fast; and second, bounded-constraints are easily applied. Similar to many optimization algorithms, the PGM is a gradient-based method, and it applies the constraints by restricting the solution space. It is very simple and effective technique for solving bounded-constraint optimization problems.

Suppose we want to minimize $f(\mathbf{x})$, subject to $l_i \leq x_i \leq u_i$, $i = 1, \cdots, n$, where l_i and u_i are lower and upper bounds for the i^{th} elements of $\mathbf{x}$, respectively. Note that f is a scalar and $\mathbf{x}$ is n-dimensional vector. Then, the PGM improves the current solution $\mathbf{x}^k$ to $\mathbf{x}^{k+1}$ using the following update rule:

$$\mathbf{x}^{k+1} = P[\mathbf{x}^k - \alpha_k \nabla f(\mathbf{x}^k)], \tag{2.12}$$

where k and α_k are the iteration step and step size, respectively. The letter P is the projection operator and is defined as,

$$P[x_i] = \begin{cases} x_i & \text{if } l_i < x_i < u_i, \\ u_i & \text{if } x_i \geq u_i, \\ l_i & \text{if } x_i \leq l_i. \end{cases} \tag{2.13}$$

The projection operator essentially forces the solution point back to the bounded-region. The only question now is the determination of the step size α_k. Bertsekas [58] proposed a simple yet effective way to estimate the step size in order to sufficiently decrease the function value at each iteration step. The condition used to check for sufficient decrease of the function value is given by,

$$f(\mathbf{x}^{k+1}) - f((x)^k) \leq \sigma \nabla f(\mathbf{x}^k)^T (\mathbf{x}^{k+1} - \mathbf{x}^k), \tag{2.14}$$

where σ is arbitrary constant between 0 and 1. The step size α_k in equation 2.12 is selected from β^{m_k} where β is arbitrary constant between 0 and 1, and m_k is positive integer (1,2,3,$\cdots$). Since β is less than one, the step size α_k (in equation 2.12) decreases with increasing value of m_k. The most computationally inefficient part of the PGM is finding the optimum step size α_k, and Lin [53] suggests an efficient way to compute the optimum step size, which significantly improves the convergence speed of the standard PGM. The optimum step size is determined by utilizing equation 2.12 and 2.14, and the improved PGM should execute the following strategy to obtain the optimum α_k:

1. Set $\alpha_k = \alpha_{k-1}$,

2. If the choice of α_k satisfies equation 2.14 (see also equation 2.18 and 2.19), then repeatedly increase α_k ($\alpha_k = \alpha_k/\beta$) until the choice of α_k does not satisfy equation 2.14 (see also equation 2.18 and 2.19).

3. Else repeatedly decrease α_k ($\alpha_k = \alpha_k\beta$) until the choice of α_k satisfies equation 2.14 (see also equation 2.18 and 2.19).

Such a selection of α_k is guaranteed to converge while improving the convergence speed [53]. The improved PGM continues to improve the current solution using equation 2.12 and 2.14 until predefined stopping condition (discussed in the latter part of this section) is met.

While combining the ANLS with the improved PGM provides an efficient and an effective way to solve the NMF problem, see equation 2.5. Lin [53] proposes another strategy to further reduce the computational cost. This involves converting equation 2.14 into a different form using the quadratic expansion in order to replace computationally expensive term ($f(\mathbf{x}^{k+1}) - f(\mathbf{x}^k)$ in equation 2.14) with a computationally inexpensive term. For a quadratic function $g(\mathbf{x})$ and vector $\mathbf{a}$, the expansion can be written as:

$$g(\mathbf{x}+\mathbf{a}) = g(\mathbf{x}) + \nabla g(\mathbf{x})^T \mathbf{a} + \frac{1}{2}\mathbf{a}^T \nabla^2 g(\mathbf{x})\mathbf{a}, \tag{2.15}$$

where $\mathbf{a}$ has the same dimension as $\mathbf{x}$ and ∇^2 is the Laplacian operator. If we substitute $\mathbf{x}$ and $\mathbf{x} + \mathbf{a}$ in equation 2.15 with $\mathbf{x}^k$ and $\mathbf{x}^{k+1}$, and assume that f in equation 2.14 is a quadratic function, then the following relationships can be obtained,

$$\begin{aligned} f(\mathbf{x^{k+1}}) - \mathbf{f}(\mathbf{x^k}) = \nabla \mathbf{f}(\mathbf{x^k})^{\mathbf{T}}(\mathbf{x^{k+1}} - \mathbf{x^k}) + \\ \frac{1}{2}(\mathbf{x^{k+1}} - \mathbf{x^k})^{\mathbf{T}} \nabla^{\mathbf{2}} \mathbf{f}(\mathbf{x^k})(\mathbf{x^{k+1}} - \mathbf{x^k}) \qquad (2.16) \\ (1-\sigma)\nabla f(\mathbf{x^k})^{\mathbf{T}}(\mathbf{x^{k+1}} - \mathbf{x^k}) + \\ \frac{1}{2}(\mathbf{x^{k+1}} - \mathbf{x^k})^{\mathbf{T}} \nabla^{\mathbf{2}} \mathbf{f}(\mathbf{x^k})(\mathbf{x^{k+1}} - \mathbf{x^k}) \leq \mathbf{0}, \qquad (2.17) \end{aligned}$$

where k and ^{T} are the discrete time index and the transpose operator, respectively. Notice that equation 2.14 is now transformed to equation 2.17 and no longer needs to calculate the function f values. This can be a huge advantage for computationally expensive objective function (e.g. the product of large matrices).

The NMF problem (see equation 2.6) must solve two sub-problems (equation 2.10 and 2.11) at every iteration step. Since the objective function of each sub-

problem is quadratic, equation 2.16 can be utilized to find the optimum α_k for each sub-problem. Thus, two versions of equation 2.17 are needed due to the two block variables ($\mathbf{W}$ and $\mathbf{H}$). By substituting equation 2.8 and 2.9 into equation 2.17 (with $\mathbf{x}^k$ being replaced by either $\mathbf{W}^k$ or $\mathbf{H}^k$), the following relationships are obtained with some algebra work,

$$\begin{aligned}(1-\sigma)\langle[\mathbf{W^k H^k}-\mathbf{V}]\mathbf{H^{kT}},(\mathbf{W^{k+1}}-\mathbf{W^k})\rangle+\\ \frac{1}{2}\langle(\mathbf{W^{k+1}}-\mathbf{W^k})(\mathbf{H^k H^{kT}}),(\mathbf{W^{k+1}}-\mathbf{W^k})\rangle\leq\mathbf{0},\end{aligned} \tag{2.18}$$

$$\begin{aligned}(1-\sigma)\langle\mathbf{W^k}^T[\mathbf{W^k H^k}-\mathbf{V}],(\mathbf{H^{k+1}}-\mathbf{H^k})\rangle+\\ \frac{1}{2}\langle(\mathbf{H^{k+1}}-\mathbf{H^k}),(\mathbf{W^{kT}W^k})(\mathbf{H^{k+1}}-\mathbf{H^k})\rangle\leq\mathbf{0},\end{aligned} \tag{2.19}$$

where $\langle\mathbf{A},\mathbf{B}\rangle$ represents the sum of the element-wise product of matrices $\mathbf{A}$ and $\mathbf{B}$. Note that $\nabla^2_W f_{ls}(\mathbf{W}^k,\mathbf{H}^k)=\mathbf{H}^k\mathbf{H}^{kT}$ and $\nabla^2_H f_{ls}(\mathbf{W}^k,\mathbf{H}^k)=\mathbf{W}^{kT}\mathbf{W}^k$ from equation 2.8 and 2.9. These two equations are the key to the improved PGM, and they are used to find the optimum step sizes for solving equation 2.10 and 2.11. Note that equation 2.18 and 2.19 are based on time step k, and should be changed accordingly with different time step.

The PGM for improving $\mathbf{W^k}$ and $\mathbf{H^k}$ are then given by,

$$\mathbf{W}^{k+1}=P[\mathbf{W}^k-\alpha^k_W\nabla_W f(\mathbf{W}^k,\mathbf{H}^k)], \tag{2.20}$$

$$\mathbf{H}^{k+1}=P[\mathbf{H}^k-\alpha^k_H\nabla_H f(\mathbf{W}.\mathbf{H}^k)], \tag{2.21}$$

Equation 2.18 and 2.19 are used to find the optimum step sizes for $\mathbf{W^k}$ and $\mathbf{H^k}$ in equation 2.20 and 2.21. Note that the projection operator P is defined in section 2.1.4 of this chapter, and the lower and upper bounds for both $\mathbf{W^k}$ and $\mathbf{H^k}$ are 0 and 1, respectively. Note that equation 2.20 and 2.21 are based on time step k, and should be changed accordingly with different time step.

Unlike many other optimization problems, the NMF problem (using the ANLS and PGM methods) requires three stopping conditions because two sub-problems have to be solved at every iteration step. The two local stopping conditions are required for each sub-problem (i.e. optimizing $\mathbf{W}$ and $\mathbf{H}$) and one global stopping condition is required for terminating the optimization process. For the PGM, a commonly used stopping condition is suggested by Lin and More [59] and is given by,

$$\|\nabla^P[f(\mathbf{x}^k)]\| \leq \varepsilon \|\nabla f(\mathbf{x}^0)\|, \tag{2.22}$$

where ε is the tolerance level and $\|\mathbf{A}\|$ is the Frobenius norm of matrix $\mathbf{A}$. The projected gradient $\nabla^P f(\mathbf{x})$ is defined as,

$$\nabla^P f(\mathbf{x}_i) = \begin{cases} \nabla f(\mathbf{x}_i) & \text{if } l_i < x_i < u_i, \\ \min(0, \nabla f(\mathbf{x}_i)) & \text{if } x_i = l_i, \\ \max(0, \nabla f(\mathbf{x}_i)) & \text{if } x_i = u_i. \end{cases} \tag{2.23}$$

The global and the local stopping conditions used for the NMF problem are then given by,

$$\|\nabla^P[f_{ls}(\mathbf{W}^k, \mathbf{H}^k)]\| \leq \delta \|\nabla f_{ls}(\mathbf{W}^0, \mathbf{H}^0)\|, \tag{2.24}$$

$$\|\nabla^P_W[f_{ls}(\mathbf{W}^{k+1}, \mathbf{H}^k)]\| \leq max(10^{-6}, \delta) \|\nabla f_{ls}(\mathbf{W}^0, \mathbf{H}^0)\|, \tag{2.25}$$

$$\|\nabla^P_H[f_{ls}(\mathbf{W}^{k+1}, \mathbf{H}^{k+1})]\| \leq max(10^{-6}, \delta) \|\nabla f_{ls}(\mathbf{W}^0, \mathbf{H}^0)\|, \tag{2.26}$$

where δ is the global tolerance level. Notice that all stopping conditions are based on the Frobenius norm of the initial gradients and the two local stopping conditions are the same. In the following section, the FADS algorithm is discussed in detail (e.g. using a flowchart) by combining all the optimization techniques described in this chapter.

2.1.5 Factor Analysis of Dynamic Structures (FADS)

In this section, the proposed FADS algorithm and the technique to generate FV's and FCs are described using a flow chart. Consider a dynamic PET dataset that consists of N transverse slices and T TF's such that there are total of $N \times T$ images. Each image consists of $M \times M$ pixels and each pixel represents 3D ACD (i.e. the average activity of a 3D voxel) within the field of view of the scanner. As discussed before, the standard ROI method can not only be complex (i.e. identification and delineation of 3D structure) but also inaccurate in extracting time activity information (e.g. partial volume and spillover effects) from the organs or tissues of interest. The proposed FADS algorithm effectively handles and minimizes these problems. The algorithm includes dual-stage optimization and two sets of colored variables are used to indicate inputs to the two optimizations: red colored variables ($\mathbf{V}$, $\mathbf{W^0}$, and $\mathbf{H^0}$) are input to the stage 1; cyan colored variables ($\mathbf{V^0}$, $\mathbf{W_1}^0$, and $\mathbf{H_{opt}}$) are input to the stage 2. During the first stage of the optimization, the goal is to find the optimum factor curve matrix ($\mathbf{H_{opt}}$) and so the voxel-averaged dataset is used for added benefit (e.g. reduced data size and improved signal-to-noise ratio). For the second stage of the optimization, the $\mathbf{H_{opt}}$ from the first stage optimization is used and the dataset $\mathbf{V^0}$ has the same number of voxels as the original dynamic PET data. Remember that the number of rows in $\mathbf{V}$ and columns in $\mathbf{W}$ much be the same (see equation 2.6). This facilitates the comparison between the extracted FV's and the time-averaged PET volume.

Figure 2.2 summarizes the procedure of the proposed FADS algorithm using a flow chart.

(a) Reshaping the 4D [M,M,N,T] dynamic PET dataset is required to perform SVD for estimating the total number of factors q and apply the SVD-based noise reduction technique to the dataset. The reshaped data is [$M \times M \times N$,T] matrix.

(b) Identify q singular values that are well above the noise levels (i.e. singular

values corresponding to the signals have distinctively higher values compared to those for the noise).

(c) Perform SVD-based noise reduction technique to the data matrix. q+1 singular values corresponding to the noise (in the dataset) are suppressed to zero and noise reduced data ($\mathbf{V_0}$) is computed using equation 2.3. Replace negative values in $\mathbf{V_0}$ by zero.

(d) Reshape data ($\mathbf{V_0}$) back to 4D [M,M,N,T] form and call it $\mathbf{V_0'}$. This step is necessary to identify physiological structures and obtain approximate (sample) TAC's that are used to warm start the first stage of the dual-stage optimization. These TAC's can contain mixed tissue information. Normalize each TAC by its maximum value and assign them as the initial factor curve matrix ($\mathbf{H_{opt}}$). To avoid stalling of the optimization, TAC's in the $\mathbf{H_{opt}}$ cannot be identical.

(e) Apply $r\times r\times 1$ in-place voxel-averaging (VA) $\mathbf{V_0'}$ and call it $\mathbf{V'}$. The VA technique reduces the data size while improving the SNR of the dataset. The optimum size of r depends on various factors (e.g. type and SNR of the dataset, extent of partial volume and spillover effects, and the shapes of the underlying kinetics) and these effects are investigated using computer simulation in chapter 3.

(f) Reshape $\mathbf{V'}$ to matrix form $[\frac{M\times M\times N}{r\times r},T]$ and call it $\mathbf{V}$. Reshaping the data is necessary to comply with the factor model (see equation 2.4). Normalize $\mathbf{V}$ by its maximum value. The normalization here is simply for convenience since the PGM constrains the solutions for the $\mathbf{W}$ and $\mathbf{H}$ to be between 0 and 1.

(g) Initialize factor coefficient matrix ($\mathbf{W^0}$) using the MATLAB^{TM}'s built-in random number (between 0 and 1) generator. Note that the row dimension of $\mathbf{W^0}$ has to be the same as that of $\mathbf{V}$. For given $\mathbf{V}$, $\mathbf{W^0}$, and $\mathbf{H^0}$, find the optimum factor curve matrix ($\mathbf{H_{opt}}$). Compute the local and global stopping conditions

using δ value of 10^{-8} and equation 2.24-2.26. Optimization parameters include $\alpha_H^0 = \alpha_W^0 = 1$, $\sigma = 0.01$, and $\beta = 0.1$. Run the ANLS algorithm (defined by equation 2.10 and 2.11) described in section 2.13 using the PGM (see equation 2.18-2.21) in section 2.14.

(h) Normalize $\mathbf{V^0}$ by its maximum value and keep the normalization constant (required to obtain FADS results in Bq/ml). Initialize factor coefficient matrix (textcolorcyan$\mathbf{W_1^0}$) using the MATLAB^{TM}'s built-in random number (between 0 and 1) generator. Note that the row dimension of $\mathbf{W_1^0}$ is the same as that of $\mathbf{V_0}$. For given $\mathbf{V^0}$, $\mathbf{H_{opt}}$, and $\mathbf{W_1^0}$, find the optimum factor coefficient matrix ($\mathbf{W_{opt}}$). Compute the global stopping condition using δ value of 10^{-8} and equation 2.25. Use the same optimization parameters defined in the previous step. Run the PGM using equation 2.18 and 2.20 in section 2.14.

(i) Column of $\mathbf{W_{opt}}$ and rows of $\mathbf{H_{opt}}$ then represent FV's and FC's, respectively. For ease of comparison each FV is normalized by its maximum value and the inverse normalization is applied to the appropriate FC. The normalization constant (in step h) is applied to every row of $\mathbf{H_{opt}}$ so that each FC has unit of Bq/ml. Reshape $\mathbf{W_{opt}}$ to 4D data [M,M,N,T] so that q FV's are easily compared against the time-averaged PET volume. If possible, co-register FV's with associated MRI or CT dataset.

2.2 Materials

2.2.1 Computer Simulation: digital phantom study

Before the FADS algorithm can be applied to clinical datasets, the algorithm must be thoroughly tested by phantom or simulation studies to understand its behavior against various factors such as SNR's, shapes of underlying kinetics, availability of prior information, severity of partial volume and spillover effects. In theory, the proposed FADS method can extract the true underlying TAC's if the technique

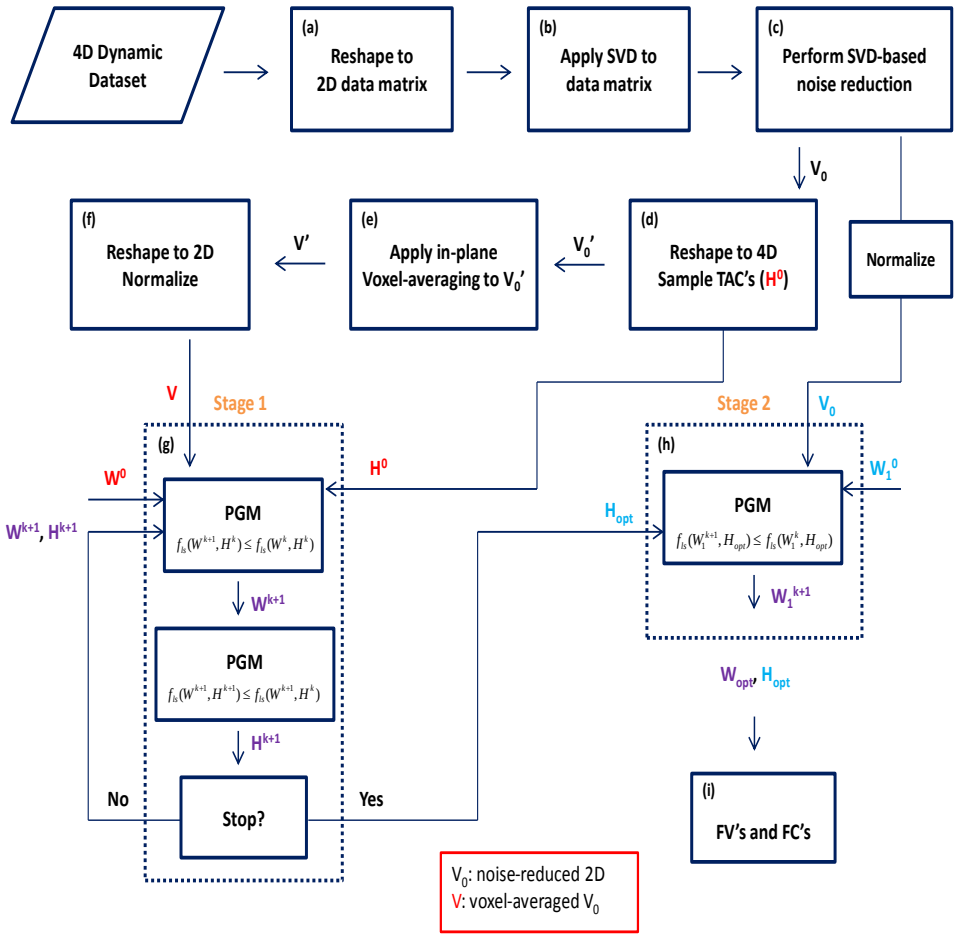

Figure 2.2. This diagram illustrates the procedure of the proposed FADS algorithm. See text for details.

is applied to noise-free dataset, consisting of partially overlapping structures, with the appropriate factor number q and a good starting point for the optimization. In reality, every dataset is corrupted by some-kind of noise and this can severely affect the SVD analysis and FADS results. First, the effects of noise (White and Poisson) and of underlying kinetic shapes, and of VA size on estimating q (by the SVD technique) are studied. Then, the effects of those factors as well as the effects of partial volume and prior information on the FADS results are investigated using computer simulated dynamic datasets.

To simulate a sequence of dynamic (medical) images, three sets of digital phantoms are generated. For simplicity, each phantom consists of three rectangular structures with varying degrees of overlap to simulate the partial volume effect. Figure 2.3 shows the three sets of digital phantoms: (case I) no PVE; (case II) small amount of PVE; (case III) large amount of PVE. Each dynamic image consists of 144×144 pixels. The clock-wise numbering (1-3) in each phantom indicates the compartment number, and it is used to assign an arbitrarily TAC to each compartment.

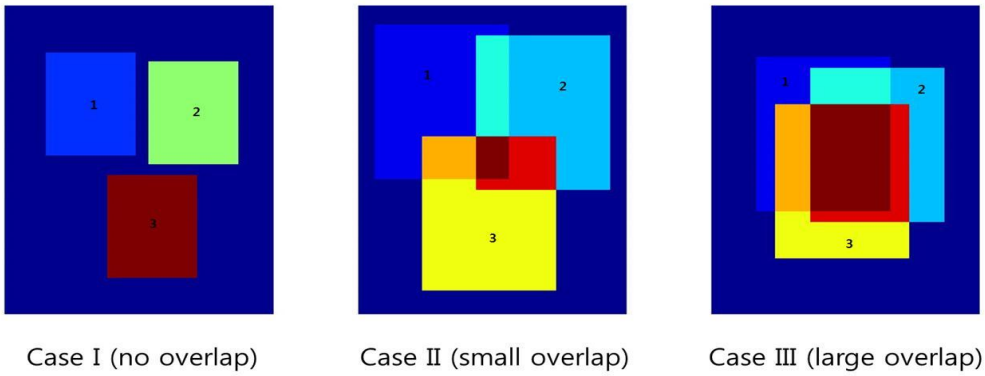

Figure 2.3. This figure depicts the three sets of digital phantoms used for the simulation study. Each phantom consists of three rectangular structures that are tissue-specific with varying degrees of PVEs. The clock-wise numbering (1-3) in each phantom is used to assign a TAC to each compartment.

Each compartment is assumed to be tissue-specific and possess a unique TAC. To comply with the factor model assumption, each compartment is assumed to have homogeneous uptake and clearance rates of the tracer so that TAC's from pixels within the compartment are the same. Figure 2.4 shows the three TAC's (e.g. TAC1, TAC2, and TAC3 describe TAC's for tissue, arterial input, and some organ) used to model the dynamic time dependency for the three compartments in each of the three digital phantoms. Each curve has an arbitrary unit and is sampled at 15 time points. Thus, each digital phantom produces 15 dynamic images, and they form the basis for the simulation study. The three sets of dynamic images are referred to as

noise-free dynamic datasets.

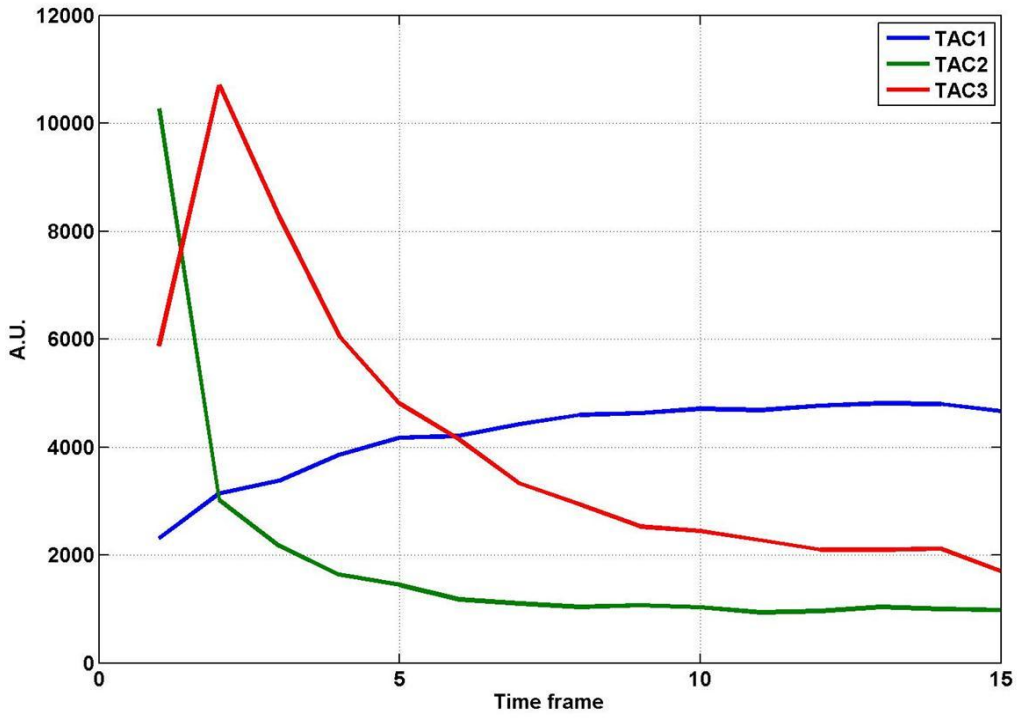

Figure 2.4. This figure shows the three arbitrarily TAC's used to model the dynamic time dependency for the three compartments in each phantom. Each curve has an arbitrarily unit and is sampled at 15 time points.

To make the simulation more realistic, electronic noise (e.g. thermal noise from electronic components and fluctuation in the number of light photons produced by a crystal interacting with 511-keV annihilation photon) is introduced to the three sets of dynamic images (e.g. cases I, II, and III datasets) using White (random signal with flat power spectrum) and Poisson (fluctuation of a variable that follows Poisson distribution) noises. To generate White noise in an image, MATLAB^{TM}'s rand function, which produces random number between 0 and 1, is used. Generated random numbers have the same matrix size as the image being corrupted and are then scaled by 5% of the maximum intensity value in the image. Poisson noise is based on the intensity value of an individual voxel in an image [26], and is gen-

erated for each voxel by the MATLAB^{TM}s built-in imnoise function (with scaled value of 10^{-10} and "Poisson" option). Each dataset is first corrupted by Poisson noise followed by White noise. These datasets are then used throughout the simulation study and are referred to as noisy datasets. The signal-to-noise ratio (SNR) is computed by taking the ratio of the mean signal value (mean pixel value in a small region of compartment) to the standard deviation value of noise (small region outside of the three compartments in an image). For the noisy (case II) dataset the SNR varies from 1 to 30 between different slices in the dataset.

The first step to successful FADS is the accurate estimation of the factor number q for the factor model (in equation 2.4). As discussed before, the SVD technique is used to identify q singular values that are well above the noise level. In some cases, it can be quite difficult to find the optimum q value if the dataset has low the SNR. To improve the SNR of the dataset, a VA technique is applied to the dataset prior to performing SVD. To investigate the effect of VA on the singular values, the SVD technique (using MATLAB^{TM}s built-in svd function) is applied to the three sets of noise-free and noisy datasets with and without the application of the VA technique. Three large singular values (out of 15 singular values) are expected and obtained without the VA, with 4×4 VA and 8×8 VA options for both noise-free and noisy cases. In each case, the three sets of singular values (e.g. without VA, 4×4 VA and 8×8 VA) are normalized to the maximum value in each set and compared with each other. The relationship between the number of unique TAC's and the number of significant singular values in the noisy dataset are also examined. If multiple structures share similar TAC's (e.g. metastatic cites) then they should be classified as a single factor. The dataset used for this study is generated with case II digital phantom and 2 unique TAC's (TAC1 and TAC3): the compartment 2 of the (case II) phantom is filled with TAC3 (at 10% of its maximum intensity) instead of TAC2. Noise is added to the dataset according to the aforementioned noise-adding technique in this section.

Once the factor number q is determined, the SVD-based noise reduction technique (equation 2.3) can be used to reduce the amount of noise in the dataset. The (case II) noisy dataset from the previous study is used, as an example, to show the effectiveness of the SVD-based noise-reduction technique. The noise-reduced dynamic images are compared against the noisy dynamic images. The noise-reduced, noisy and true TAC's from the three compartments are normalized and compared against each other.

From here on, the focus is on various factors that affect our FADS algorithm. First, the effect of VA and of prior information on the FADS result is investigated using the three sets (case I, II and III) of noise-free and noisy datasets. To improve the SNR's of the datasets, the SVD-based noise reduction technique is applied to the datasets with 4×4 VA technique prior to running FADS. To obtain prior information, the conventional ROI method is used to obtain sample TAC's from the three compartments in the (noise-reduced) datasets. Those TAC's are then used to warm start the first stage of optimization in the algorithm. The extracted factor images and curves from these datasets are then graphically compared against the known factor images and curves.

To better understand the affect of prior information, a statistical study is performed using the result of FADS. First, a total of 5000 (case II) noisy datasets are created using the same noise-adding technique (described earlier in this section). The FADS technique is applied to each dataset with the same pre-processing steps (SVD-based noise reduction and 4×4 VA technique). The resulting FC's and the true TAC's are then used to compute the accuracy (defined by equation 2.27) and also used to generate accuracy histograms. For each dataset, two sets of FC's and two D values are obtained: one set of FC's is produced with the prior information; the other set of FC's is generated from a random starting point. The same ROI method (described earlier in this section) is used to obtain prior information for the datasets. The accuracy (D) of extracted FC's is defined as,

$$D = \frac{\sum_{i=1}^{q}\sum_{t=1}^{n}|(\mathbf{tTAC})_{\mathbf{it}} - \mathbf{H_{it}}|}{\sum_{i=1}^{q}\sum_{t=1}^{n}(\mathbf{tTAC})_{\mathbf{it}}}, \tag{2.27}$$

where rows of **tTAC** and **H** represent the (normalized) true TAC and the extracted factor curve matrices, respectively. To illustrate the meaning of the D value, we select an example from the ensemble of the statistical study. The extracted factor images and curves are compared against the known factor images and curves.

The algorithm is also tested for its ability to accurately classify different structures with similar TAC's (e.g. metastatic cites should be identified as a single factor, see section 3.7). As long as different structures share the same (or relatively similar) TAC's, they will be classified as the same factor regardless of their uptake levels (or intensity). For this study, the (case III) digital phantom with two (instead of three) TAC's are used: the compartment 2 of the phantom is filled with TAC3 (at 30% of its maximum intensity) instead of TAC2. The reason for the selection of this dataset is because it has the maximum amount of partial volume effect. The same aforementioned noise adding technique discussed in this section is used.

Until now, the benefit of VA (especially for reducing the amount of noise in the dataset) is discussed, but the accuracy on the result of FADS might suffer from the selection of VA size as well. To investigate this, various VA sizes (1×1, 4×4, 8×8, 16×16, 48×48, and 72×72) are applied to the (case II) noisy dataset and the six sets of factor images and factor curves are generated for comparison. The accuracy value (D defined by equation 2.27) is also computed for each VA dataset and compared against each other.

The proper estimation of factor number q is critical step in the FADS algorithm. To study the effect of improper estimation of q, the FADS analysis is applied to the noisy (case II) dataset assuming $q = 4$ with the 4×4 VA technique. The sample TAC's from the dataset (using prior information) is used to warm start the optimization process in the FADS algorithm. Two different starting points are generated for the extra factor: one is produced with the random number generator; the other is

similar to sample TAC from the compartment 3. The resulting factor images and factor curves are compared against the known images and the true TAC's.

Finally, the least square errors are computed for the first stage of the dual stage optimization in the FADS algorithm since the most computationally inefficient and important part of the algorithm is finding the optimum FC's (see figure 2.2). The least square errors (defined by equation 2.5) are calculated for both the warm and the random starting options as a function of the size of VA. For this study, the noisy (case II) dataset is used with $q = 3$ and 4×4 VA option.

2.2.2 Clinical Study: detection of early Parkinson's disease

Parkinsons disease (PD) is a medical disorder that is related to the loss of dopaminergic neurons within the substantia nigra (center region of the brain). Figure 2.5 shows various anatomical structures that compose the substantia nigra. The dopaminergic neurons are mainly located in the blue and the dark organs (e.g. Nucleus caudatus and Putamen). Thus, patients with PD will have a decreased number of dopaminergic neurons in these organs. To measure the loss of those neurons [^{11}C]-Dihydrotetrabenzine (DTBZ) radiotracer - that targets dopaminergic neurons - has been developed and is used to diagnose patients with the early stage of PD [60]. Therefore, PD patients will have reduction of binding site for the radiotracer (i.e. decreased uptake of the radiotracer in those tissues).

The typical symptoms of PD are movement-related (i.e. trembling, slowed movement, stiffness and loss of balance) but can accompany cognitive and behavior problems in the later stage of the disease. While there is no known cure for the disease, accurate and early diagnosis of PD plays an important role for improving the quality of life of the patients and caregivers. With early detection, the disease can be effectively managed by various medical treatments and programs that are designed to alleviate the symptoms of PD and slow down the progression of the disease.

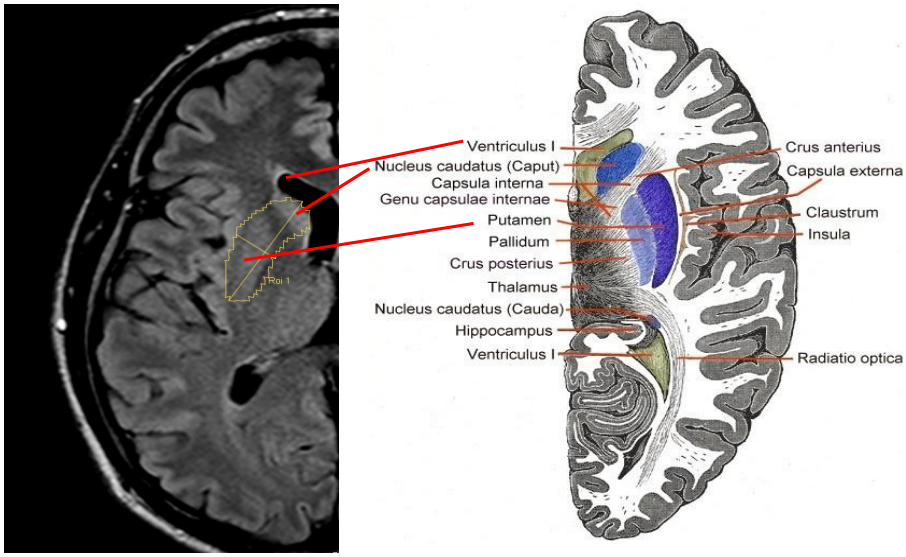

Figure 2.5. This figure shows various anatomical structures that are part of the substantia nigra (middle region of the brain). See text for details.

In this clinical study, a total of 60 subjects (20 healthy and 40 diagnosed with PD) undergo dynamic PET scans with DTBZ radio-tracer. The tracer combines with the dopaminergic neuron receptors and can be used to measure the change in the uptake of dopaminergic neurons (in the substantia nigra) to identify early, untreated PD patients against the healthy subjects. For unbiased analysis, recruited healthy subjects were carefully selected to match age and sex (see Appendix). All patients with PD met the standard criteria for clinical diagnosis of PD from the Movement Disorders Program using the Unified Parkinsons Disease Rating Scale [61]. At the time of writing this thesis, only ten dynamic PET datasets (4 healthy and 6 diseased subjects) were available. Unfortunately, two subjects (dtbz5 and dtbz7) were removed from FADS analysis in this work due to a quality control failure that only became apparent after the subject's datasets were acquired. Before the analysis, clinical datasets were anonymized accordingly.

Each of the ten subjects underwent the dynamic PET scan by administering 185

$\pm$ 18.5 MBq of the [^{11}C]-DTBZ by following the dynamic protocol [62, 63, 64]. Dynamic PET volumes were acquired using a Philips Gemini GS PET/CT scanner at the Cross Cancer Institute. Each PET volume consisted of 144 $\times$ 144 $\times$ 45 isotropic 4mm voxels. To apply attenuation and scatter corrections to the obtained PET volume, a low-dose CT transmission scan was also acquired. Following the dynamic protocol, the subject was positioned with head-first-supine scanning option and imaged for 60 minutes post injection. A simple decay (equation 1.2) and aforementioned attenuation corrections are applied to the obtained datasets. Then, these datasets are grouped and summed together according to the following: four 1-min, three 2-min, eight 5-min, and one 10-min windows starting at tracer injection. Finally, a sequence of 16 (dynamic) PET volumes is generated by applying reconstruction algorithm to these datasets.

The proposed FADS technique is applied to the eight DTBZ datasets assuming two factors (q = 2) with 2 $\times$ 2 $\times$ 1 in-plane VA option and prior information (e.g. sample TAC's from the striatum and non-striatum tissues). Each dynamic dataset is then decomposed into two FV's, representing the striatum and non-striatum tissues, and associated FC's. Since diseased subjects have lower tracer-uptake in the striatum tissues in comparison to healthy subjects due to loss of dopaminergic neurons in the substantia nigra (or middle region) of the brain. The extracted FV's and FC's are then compared against each other within the group and also between the two groups. The FV's are also compared against the time-averaged PET volume. Since the major difference of the tracer-uptake lies in s few slices (near the center of PET volume), these slices are used for the comparison. In addition, a factor-based metric is developed to stratify early, untreated PD patients from the healthy subjects. The metric is based on the extracted FV's and FC's, and is defined as,

$$Ratio = \frac{A_1}{A_2}, \tag{2.28}$$

where A_1 is defined as,

$$A_1 = (\frac{\sum_{t=1}^{n} H_{1t}}{n})[\sum_{i>threshold} W_{i1}]_{mean}, \tag{2.29}$$

and A_2 is defined as,

$$A_2 = (\frac{\sum_{t=1}^{n} H_{2t}}{n})[\sum_{i<0.4} W_{i1}]_{mean}, \tag{2.30}$$

and *threshold* lies between 0 and 0.9 with increment of 0.1 and $[\cdot]_{mean}$ operator is the mean of the sum of selected voxels in the FV. Since each FV is normalized to one, voxel selection is easily made for the calculation of the metric by setting the *threshold* value (0-1). The variables A_1 and A_2 have units of MBq, and depend on factor 1 and 2, respectively. Based on the analysis of the eight DTBZ datasets, the optimum threshold value is recommended for our in-house developed metric.

Chapter 3

Result I (Simulation Study)

3.1 Digital phantoms: three-compartment models

By using three sets of digital phantoms (cases I, II and III in figure 2.3) and of TAC's (see figure 2.4), three sets of noise-free and noisy dynamic datasets are simulated. Each dataset consists of 15 dynamic images, describing the time evolution of 3D ACD's for the three compartments. Each image contains 144×144 voxels. These datasets are then used for investigating various influences on the result of FADS. Figure 3.1 shows sample images produced with the three sets of digital phantoms. The images in the top and the center rows are time-averaged (over 15 TF's) slices for the noise-free and the noisy datasets. The images in the bottom row show slices at the 5^{th} time frame (TF) for each of the three cases. The numberings (1, 2, and 3) in the top row images indicate the compartment numbers, and they are used to label the extracted FC's for future reference.

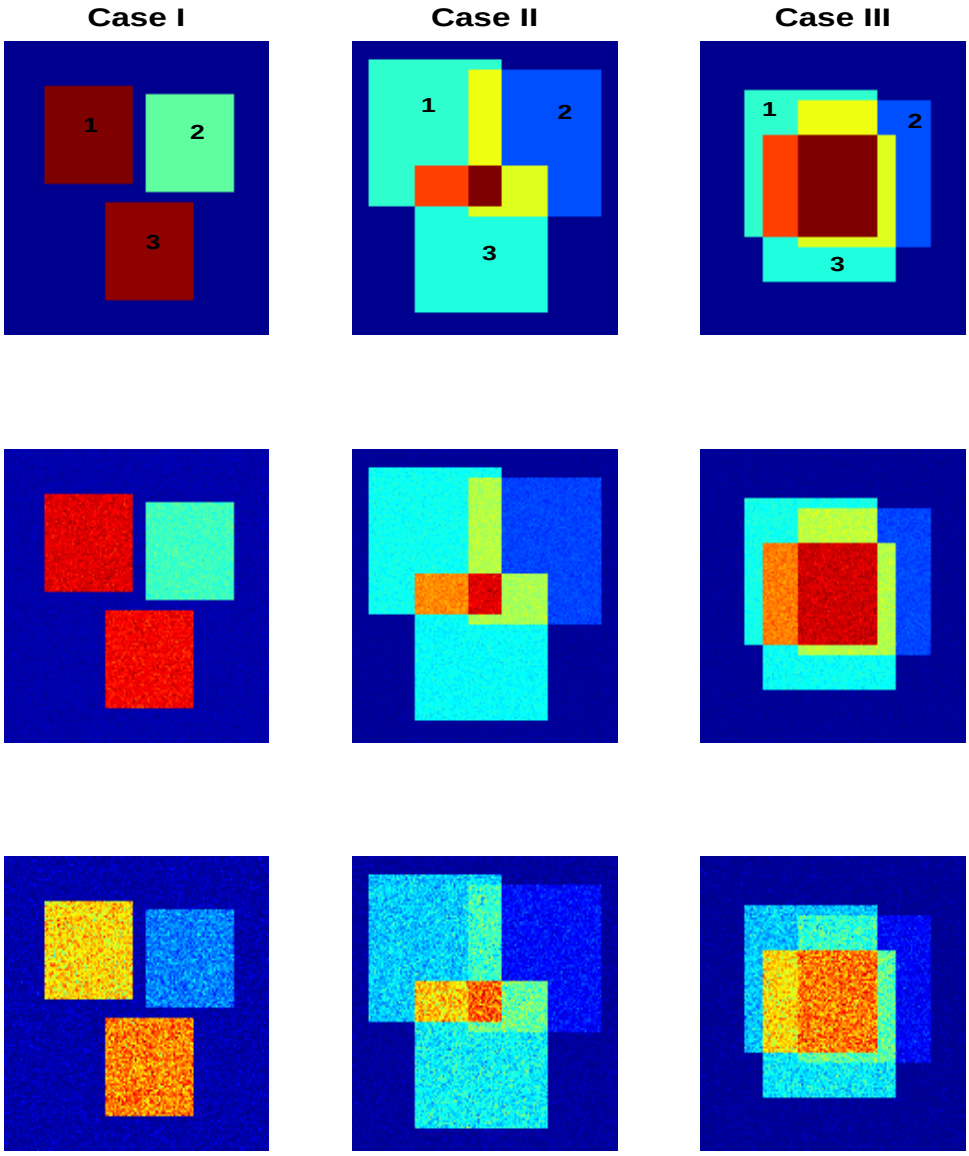

Figure 3.1. This figure shows sample of images produced by the three sets of digital phantoms and of TAC's (see figure 2.3 and 2.4). Each column represents three different cases of the dynamic datasets. The images in the top and center rows are time-averaged (over 15 TF's) slices for the noise-free and the noisy datasets. The images in the bottom row show slices at the 5^{th} TF for each of the three cases. The numberings (1, 2 and 3) in the top row images indicate the compartment numbers, and they are used to label the extracted FC's for future reference.

3.2 Singular Value Decomposition: effects of partial volume, voxel-averaging and noise

Figure 3.2 depicts normalized singular values for the noise-free (case I) dataset before and after applying the 4×4 and 8×8 VA techniques. Three large singular values correspond to the three principle images that, in general, do not represent the "pure" underlying structures. However, they can be used to estimate the number of underlying kinetics in the dataset. Notice that the application of VA has almost no effect on the resulting singular values in the absence of noise.

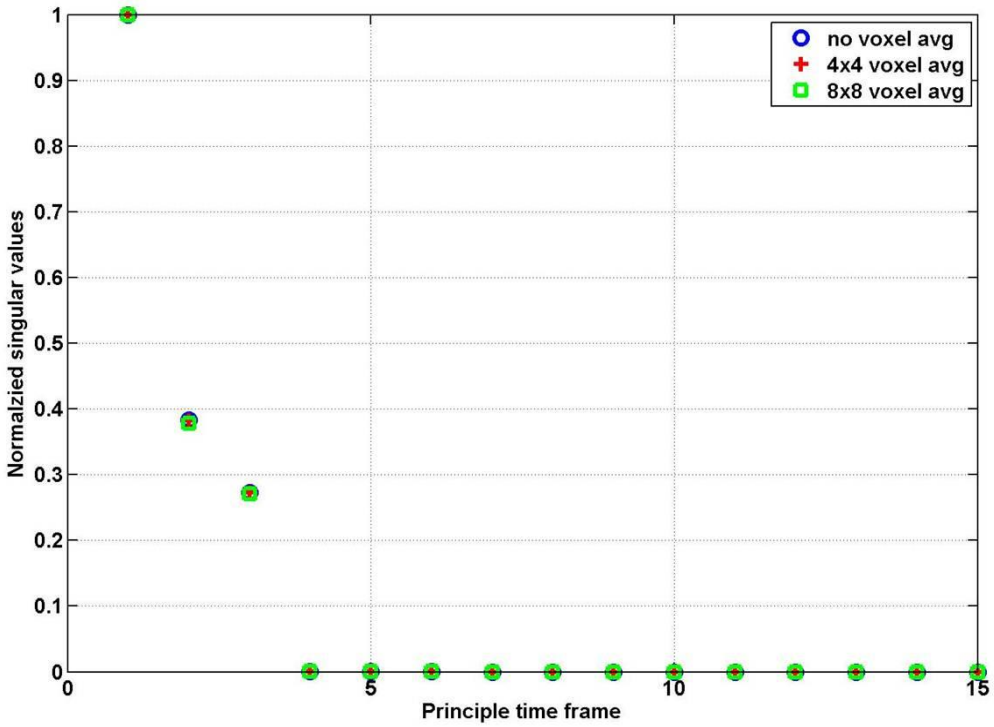

Figure 3.2. Shown are the normalized singular values for the noise-free (case I) dataset before and after the (4×4 and 8×8) VA techniques. Three large singular values are observed and they represent the three underlying kinetics in the dataset. Notice that the application of VA has almost no effect on the resulting singular values in the absence of noise.

Figure 3.3 and 3.4 depict normalized singular values for the noise-free (case I and II) datasets before and after applying the 4×4 and the 8×8 VA techniques. As

for figure 3.2, the three large singular values (out of 15 values) represent the three underlying kinetics in each of the datasets. It is evident that the VA technique has a negligible effect on the resulting singular values in the absence of noise. However, the PVE on the SVD result can be seen by comparing the normalized singular values in figure 3.2 with either figure 3.3 or 3.4. Note that the second and the third singular values decrease, as the overlap between the compartments increases. For example, the second and the third normalized singular values for the noise-free (case I) dataset in figure 3.2 are approximately 0.38 and 0.27, respectively, whereas the second and the third normalized singular values for the noise-free (case II) dataset in figure 3.3 are roughly 0.29 and 0.21, respectively. The second and the third normalized singular values are even lower for the noise-free (case III) dataset in figure 3.4 (approximately 0.12 and 0.18, respectively). The noise-free (case III) dataset with 8 $\times$ 8 VA decreases the second and the third normalized singular values even further, showing that the VA technique reduces the contribution of non-dominant principle components relative to the dominant principle component. As the amount of overlap between the structures increases, there are fewer of "pure" voxels available to differentiate between the three different types of kinetics in the dataset. Therefore, the VA technique should be avoided in datasets known to have a large amount of overlapping structures.

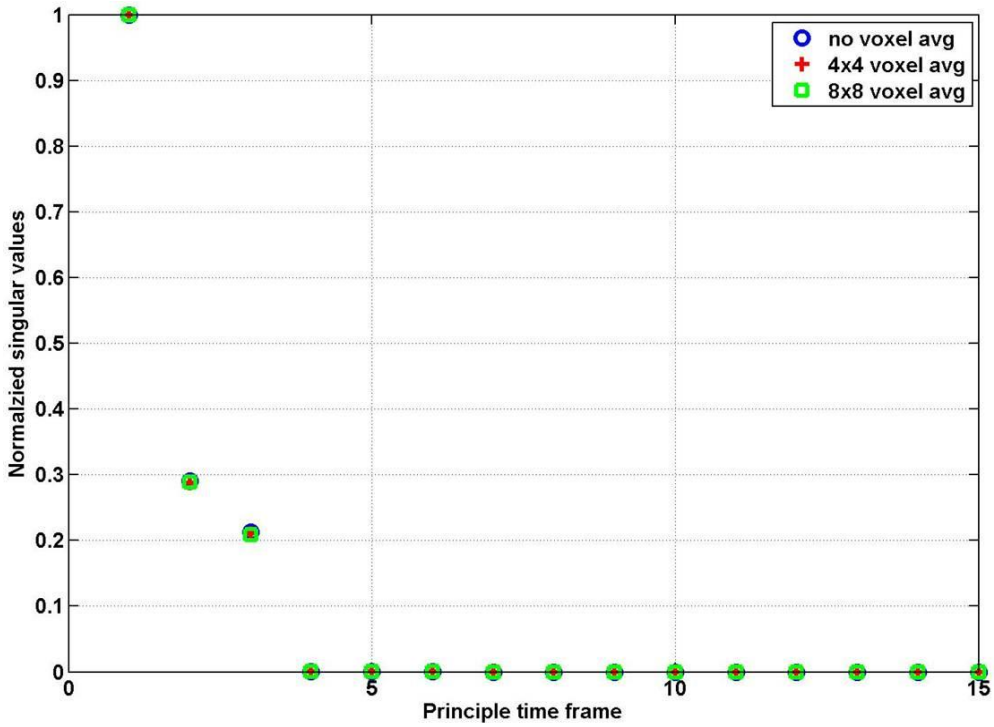

Figure 3.3. Same as for figure 3.2 except for noise-free (case II) dataset. Notice that the voxel-averaging has negligible effect on the resulting singular values. In comparison to figure 3.2, the second and third singular values are slightly lower. See text for details.

Figure 3.5 to 3.7 illustrate the effect of Poisson and White noise on the resulting singular values using the noisy (case I, II and III) datasets before and after applying the 4×4 and the 8×8 VA techniques. In all three cases, three large singular values are observed which correspond to the three underlying kinetics in each of the datasets. While the VA technique can be an effective way to suppress singular values that correspond to the noise, it can also decrease the singular values that correspond to the underlying kinetics or factors (see figure 3.5 to 3.7). The contribution of the second and third singular values relative to the first singular value decreases with the larger VA. Increasing the size of VA has the similar effect as increasing the PVE. Unfortunately, there is no method to find the optimum size of VA for any given dataset, and the size must be determined by the trial and error. Finally, the

identification of the third factor (or third singular value) in figure 3.7 can be very difficult without the application of 4×4 or 8×8 VA techniques.

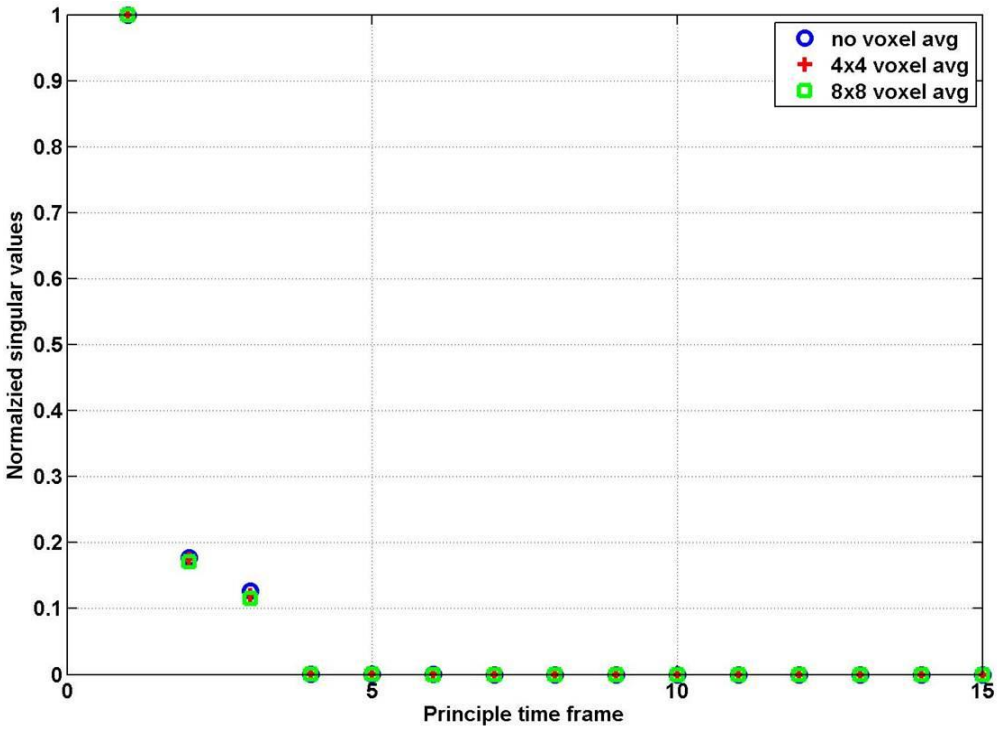

Figure 3.4. Same as for figure 3.2 except for noise-free (case III) dataset. Notice that the application of VA slightly decreases the resulting singular values. In comparison to figure 3.2 and 3.3, the second and third singular values are much lower. See text for details.

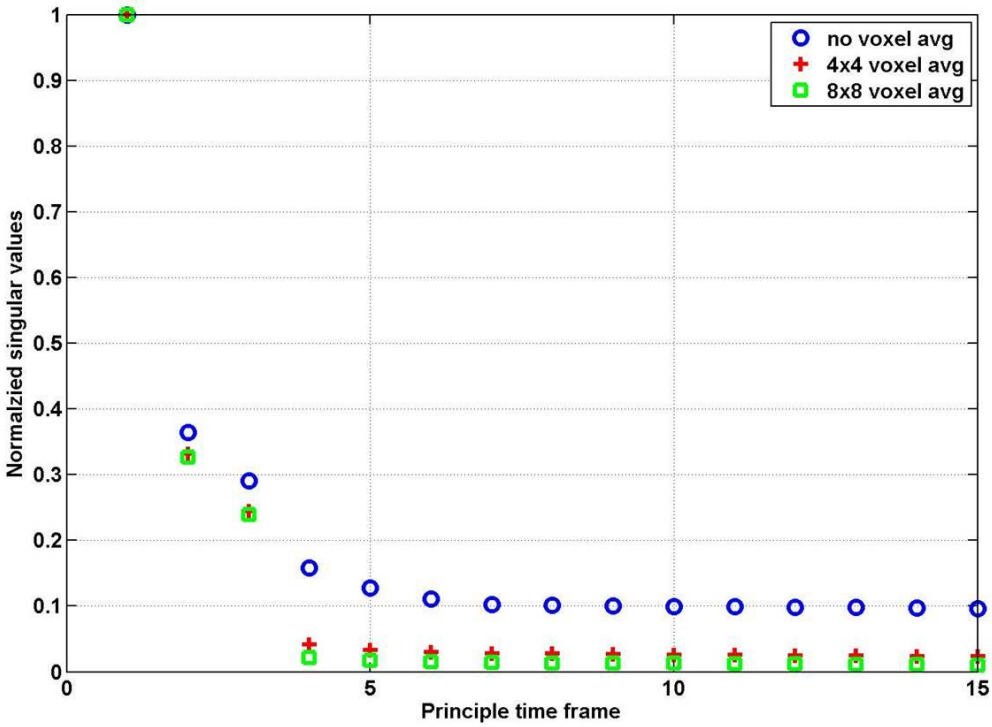

Figure 3.5. Same as figure 3.2 except for noisy (case I) dataset. Notice that the normalized singular values corresponding to the noise are significantly reduced after the application of VA technique. The SNR of the dataset can be further improved by applying the larger size of VA.

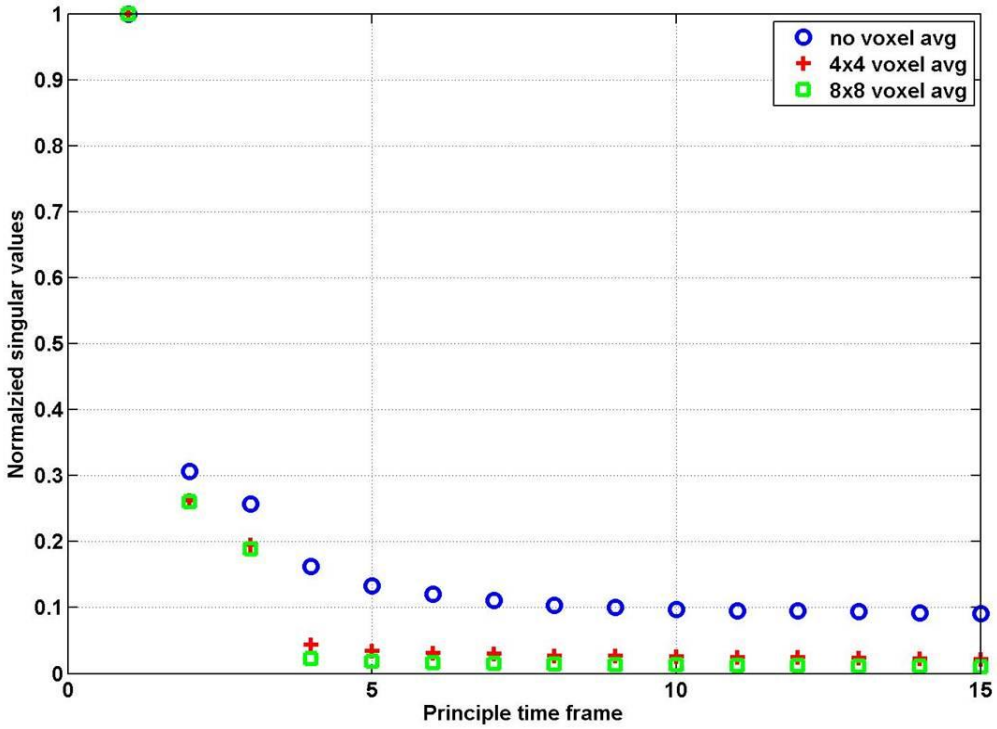

Figure 3.6. Same as figure 3.5 except for noisy (case II) dataset. The larger the size of VA, greater noise suppression is achieved. In comparison to figure 3.5, the second and the third normalized singular values are lower.

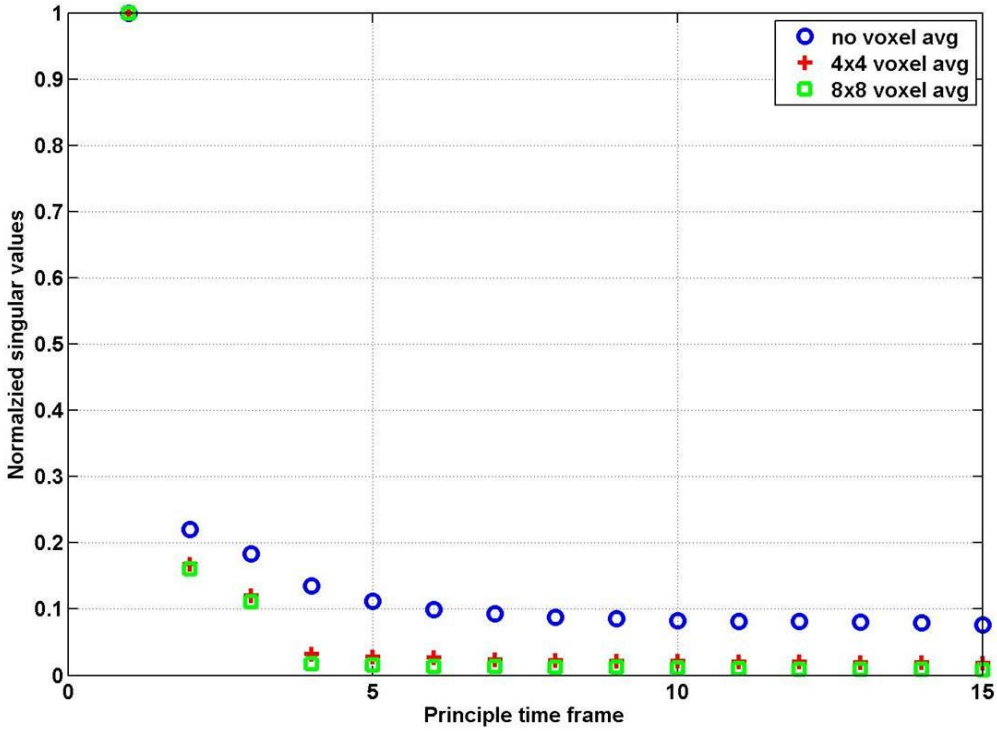

Figure 3.7. Same as figure 3.5 except for noisy (case III) dataset. In comparison to figure 3.5 and 3.6, the second and the third normalized singular values are much lower.

3.3 Singular Value Decomposition: 2 underlying kinetics

Until now, SVD is applied to datasets that consists of three factors (or three kinetics) and identified three distinctive singular values regardless of the noise level and the PVE. Figure 3.8 shows the effect of having only two unique TAC's in the noisy (case II) dataset. As expected, there are only two large singular values (out of 15 values) that represent the two underlying kinetics of the dataset. Similar as before, the normalized singular values corresponding to the noise are significantly reduced by applying the 4×4 and the 8×8 VA techniques.

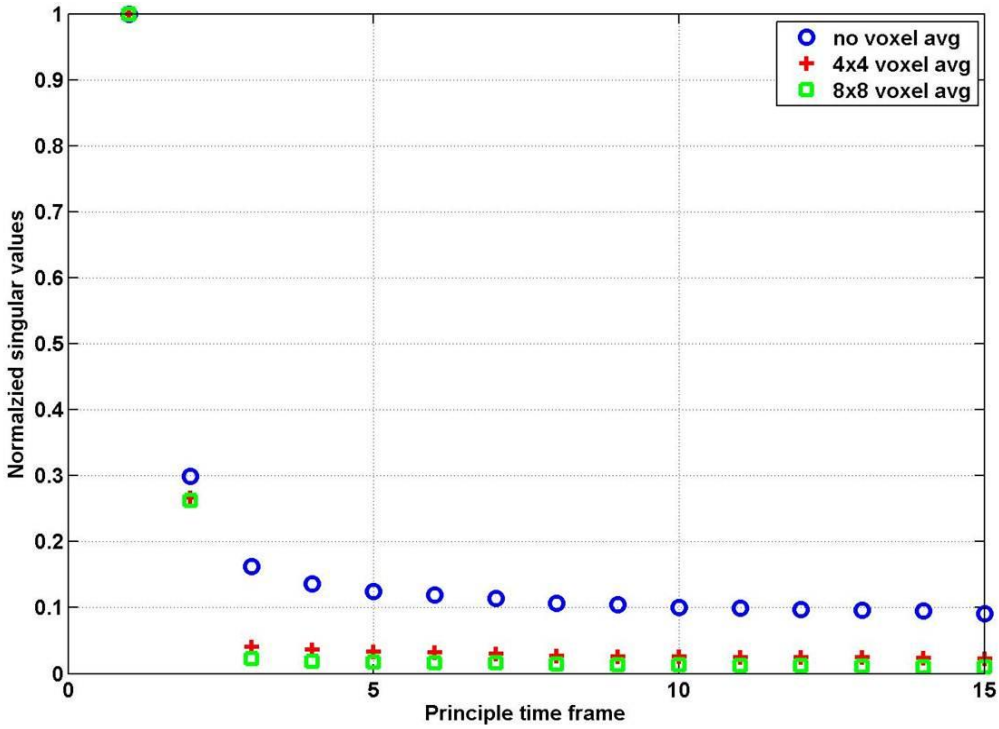

Figure 3.8. The two large singular values represent the two underlying kinetics in the noisy (case III) dataset. The figure format is the same as figure 3.5. Notice that the normalized singular values corresponding to the noise are significantly reduced after the application of the 4×4 and 8×8 VA techniques. With the larger size of VA, greater noise suppression can be achieved.

3.4 SVD-based noise reduction

Another important aspect of SVD in this study is its application to noise reduction. Figure 3.9 shows an example images from the noisy (case II) dynamic dataset. The first three images in the top row represent the first three TF's and in the bottom row the images corresponding to the last three TF's. Figure 3.10 depicts the fifteen principle images obtained by SVD, and it is clear that the first three principle images contain the signal in the dynamic dataset, where as the remaining 12 images are significantly dominated by the noise of the dynamic dataset. By using the three principle images from the figure 3.10, noise-reduced dynamic images are produced (see figure 3.11). The SNR's of the dynamic images are significantly im-

proved after the application of the SVD-based noise-reduction. Samples of noisy and noise-reduced TAC's from the center pixels of the three compartments of the noisy (case II) dynamic datasets (in figure 3.9) are compared against the true TAC's (see figure 3.12). The maximum value of each curve is normalized to one for ease of comparison. The red, blue and green lines indicate TAC's for the compartment 1, 2 and 3 (e.g. tTAC1, tTAC2, and tTAC3). The dotted and dash-dotted curves represent the original (nTAC's) and noise-reduced TAC's (nrTAC's), respectively. Notice that the noise-reduced TAC's are much closer to the true TAC's.

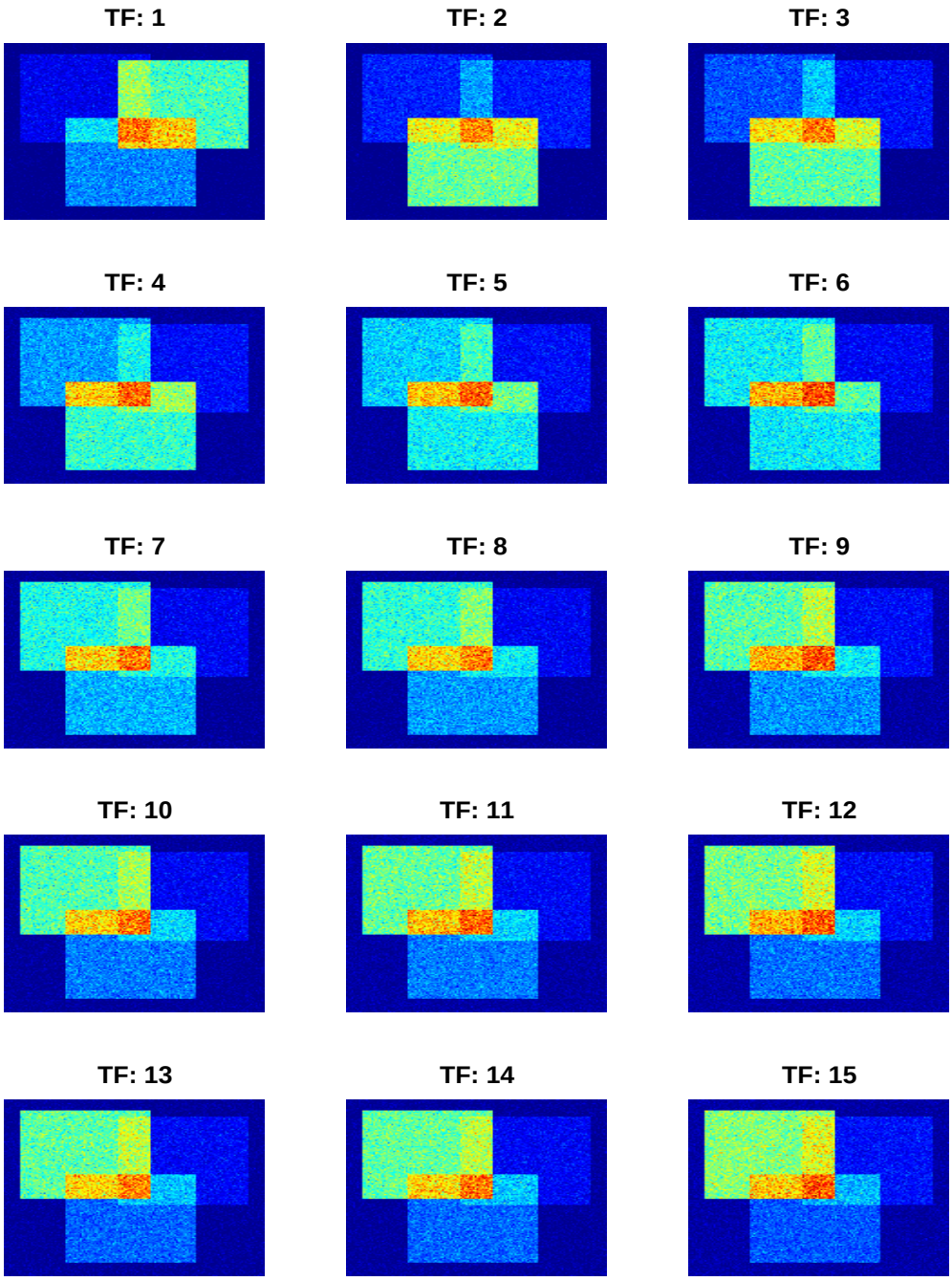

Figure 3.9. Shown are the dynamic images (a total of 15 TF's) from the noisy (case II) dynamic dataset.

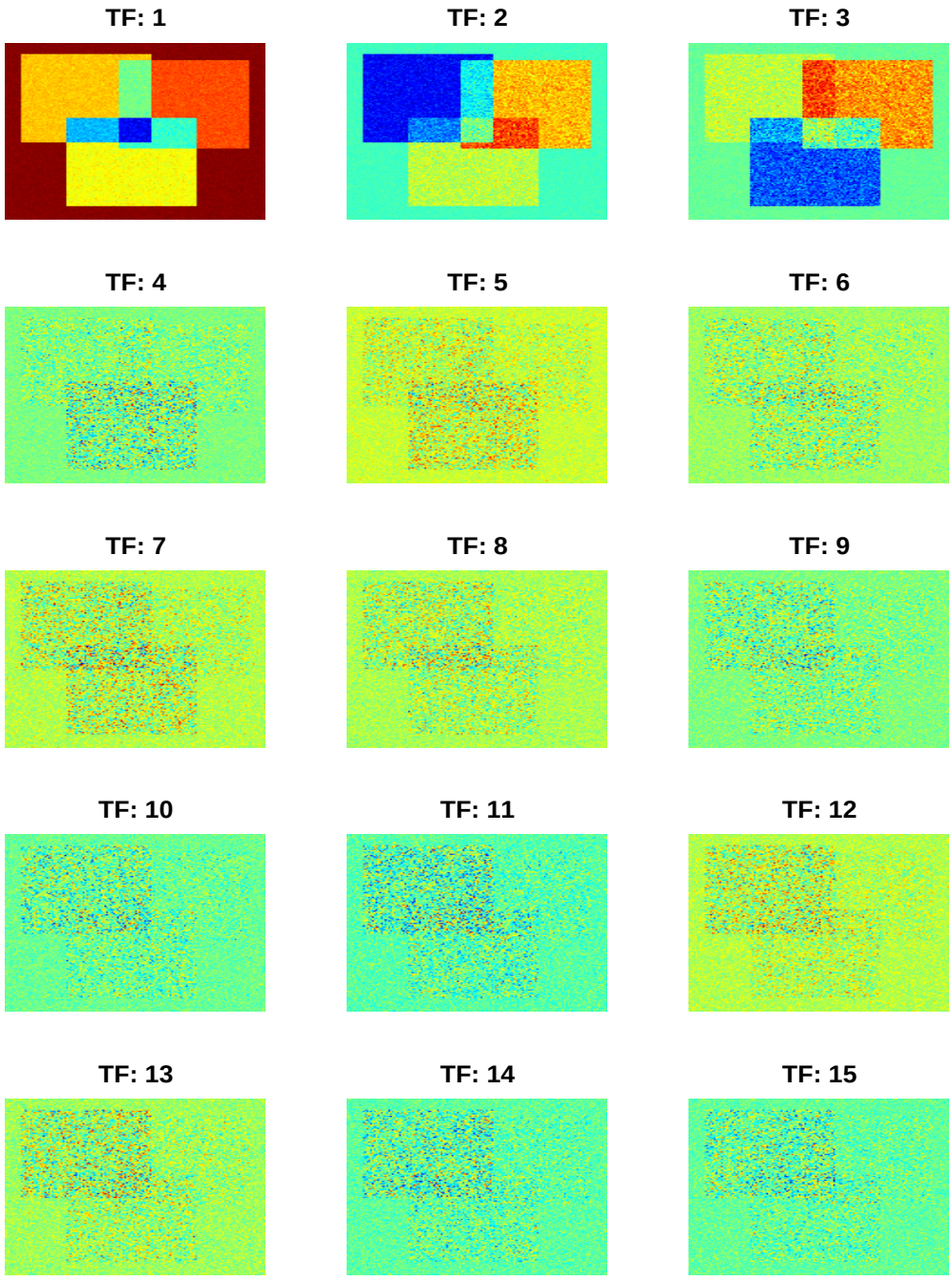

Figure 3.10. Shown are the SVD-based principle images of the dynamic dataset (see figure 3.9). The figure format is the same as figure 3.9. See text for details.

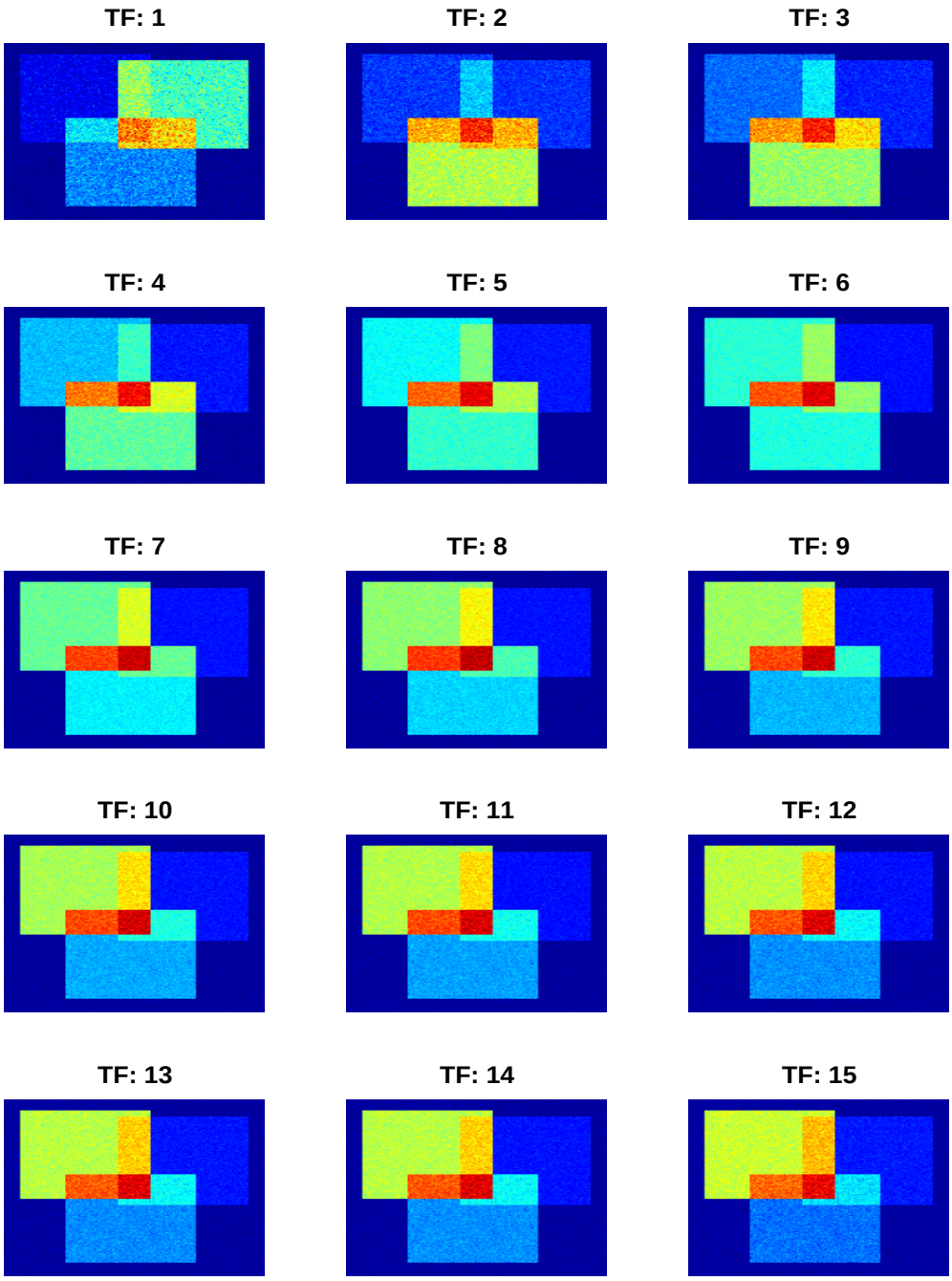

Figure 3.11. Shown are the noise-reduced images after applying the SVD-based noise reduction to the dynamic images shown in figure 3.9. The figure format is the same as figure 3.9. Notice that images appear less noisy in comparison to the original dynamic images (see figure 3.9).

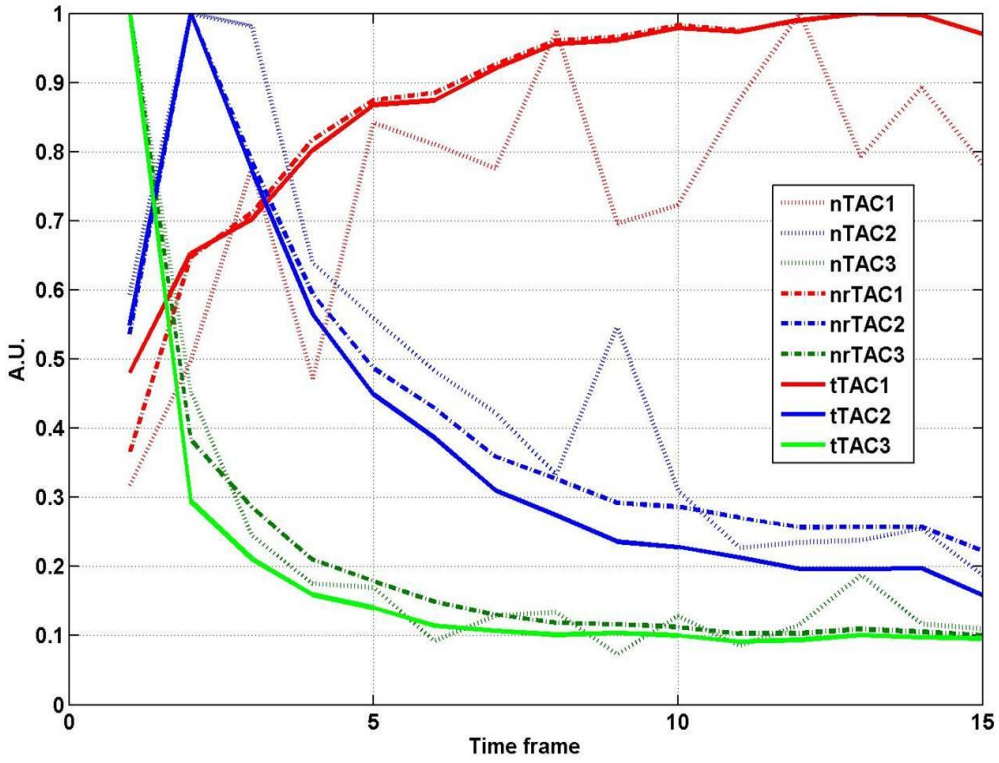

Figure 3.12. This figure shows samples of TAC's from the three compartments of the noisy (case II) dynamic dataset (see figure 3.9). Each curve is normalized to unity for ease of comparison. The red, blue and green curves indicate TAC's for compartment 1, 2 and 3 (e.g. tTAC1, tTAC2 and tTAC3). The dotted and dash-dotted curves represent the original (nTAC's) and the noise-reduced TAC's (nrTAC's), respectively.

3.5 Factor Analysis of Dynamic Structures: effects of partial volume, noise and prior information

As discussed before, the result of the proposed FADS technique is highly dependent on the starting point of the optimization. Figure 3.13 to 3.15 show extracted factor images (FI1, FI2 and FI3) from the noise-free (case I, II and III) dynamic datasets with and without the prior information. In these examples, the 4×4 VA technique is applied to the three datasets prior to running FADS, and the (normalized) sample TAC's (identical to the true TAC's in figure 3.12) from the three compartments (based on the prior information) are used to warm start the optimization of the

FADS algorithm. In figure 3.13, the left image represents the TA slice over 15 TF's. The three images in the top-right side of the figure are produced with the prior information, and the three images in the bottom-right side of the figure are generated with a random starting point. The formats of figure 3.14 and 3.15 are as the same as figure 3.13. The factor imaged produce without prior information does not represent pure structure and their associated TAC's are different from the true TAc's. On the other hand, the factor images generated with prior information represent the pure structures and their TAC's are almost identical to the known TAC's.

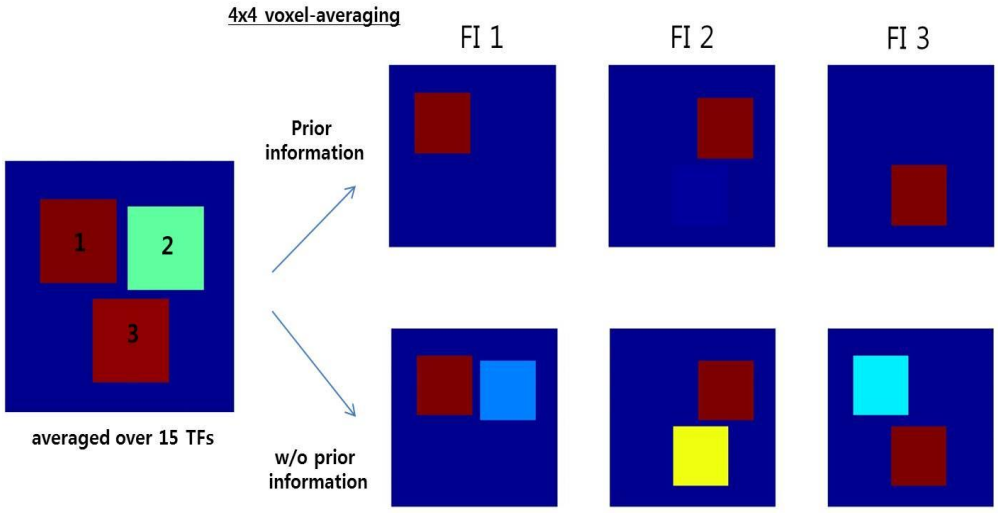

Figure 3.13. Shown are the extracted factor images for the noise-free (case I) dynamic dataset using the proposed FADS technique. The image in the left side shows the TA slice (over 15 TF's). The top three images and bottom three images on the right side of the figure depict the extracted factor images with and without prior information, respectively. It is clear that the FADS result with the prior information is much closer to the ground truth. See text for details.

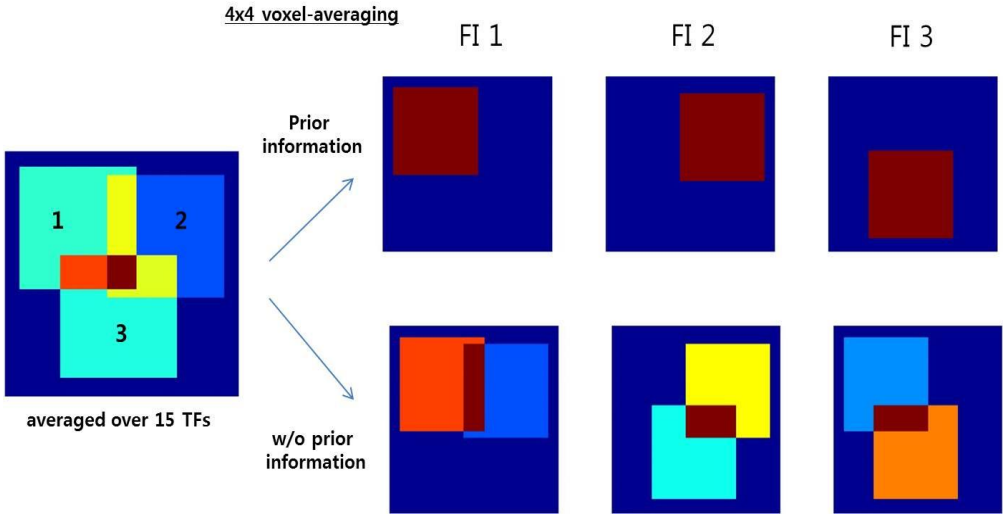

Figure 3.14. Same as figure 3.13 except for the noise-free (case II) dynamic dataset.

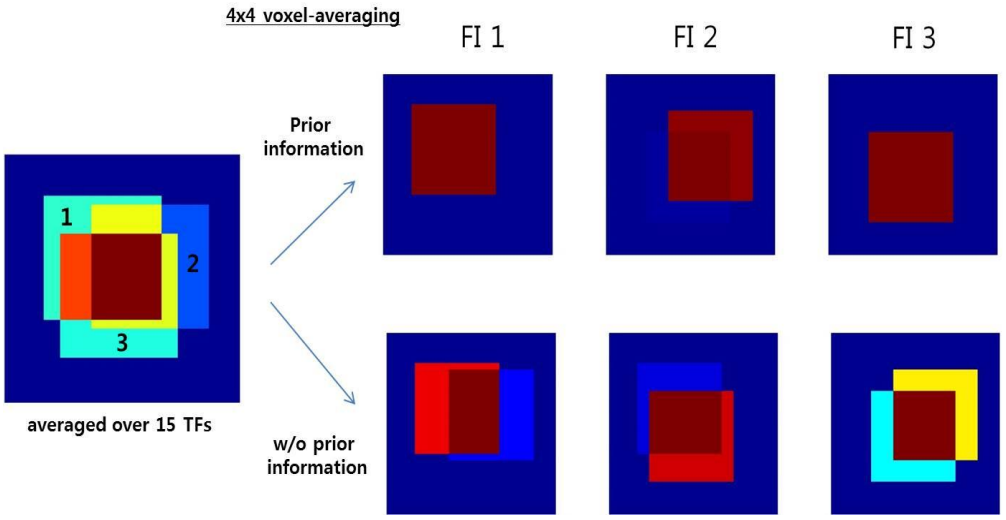

Figure 3.15. Same as figure 3.13 except for the noise-free (case III) dynamic dataset.

Figure 3.16 to 3.18 depict extracted factor images (FI1, FI2 and FI3) and FC's (FC1, FC2 and FC3) from the noisy (case I, II and III) dynamic datasets using the sample TAC's (similar to noise reduced TAC's in figure 3.12). The same 4×4 VA technique and warm starting option are used to produce the factor images and the associated factor curves. Those images and curves are then compared against the

true underlying structures and true TAC's. In figure 3.16, the top and the bottom images on the left side represent the TA (over 15 TF's) and the 5^{th} TF images. The three images in the top row and six curves on the bottom right represent the extracted factor images and the factor curves (with the true TAC's). The formats of figure 3.17 and 3.18 are the same as figure 3.16.

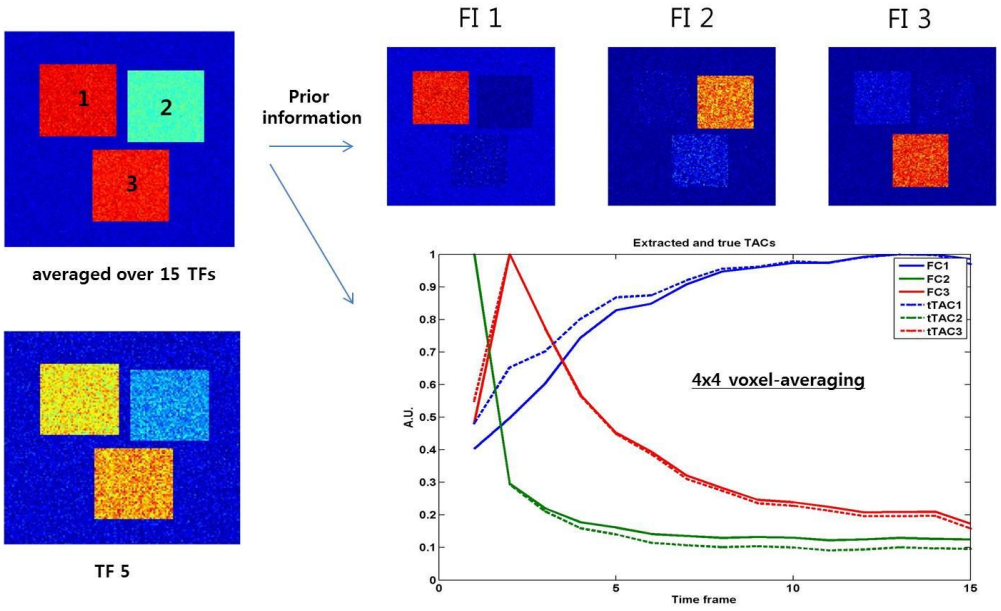

Figure 3.16. Shown are the extracted factor images and FC's for the noisy (case I) dynamic dataset using the FADS technique with the prior information. The top and bottom images in the left side of the figure represent the time-averaged (over 15 TF's) and the 5th TF images. The top three images in the right side of the figure represent the extracted factor images. The bottom right figure contains the extracted FC's (solid curves) and the true TAC's (dashed curves). The FC's and true TAC's are normalized for ease of comparison. See text for details.

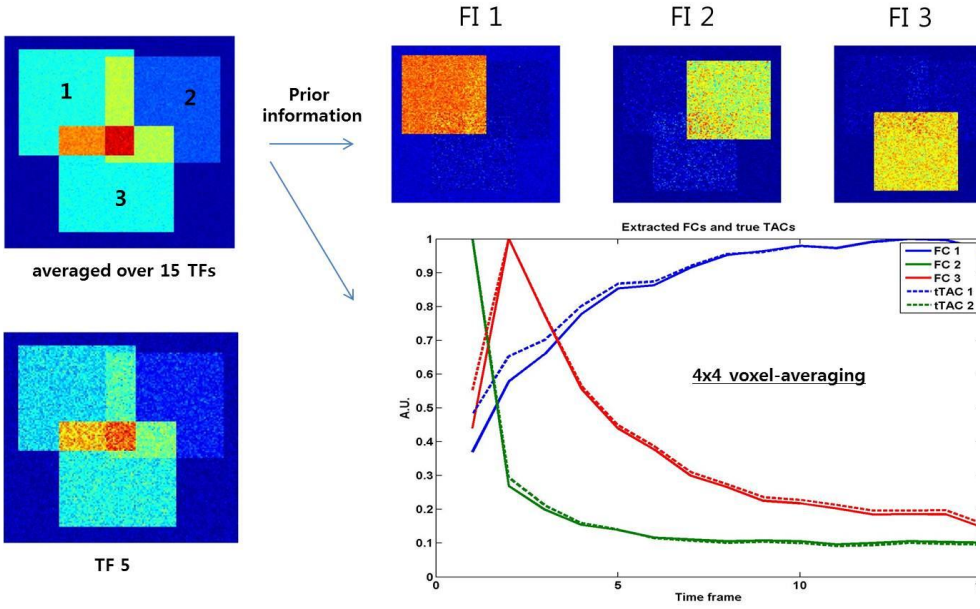

Figure 3.17. Same as figure 3.16 except for the noisy (case II) dynamic dataset.

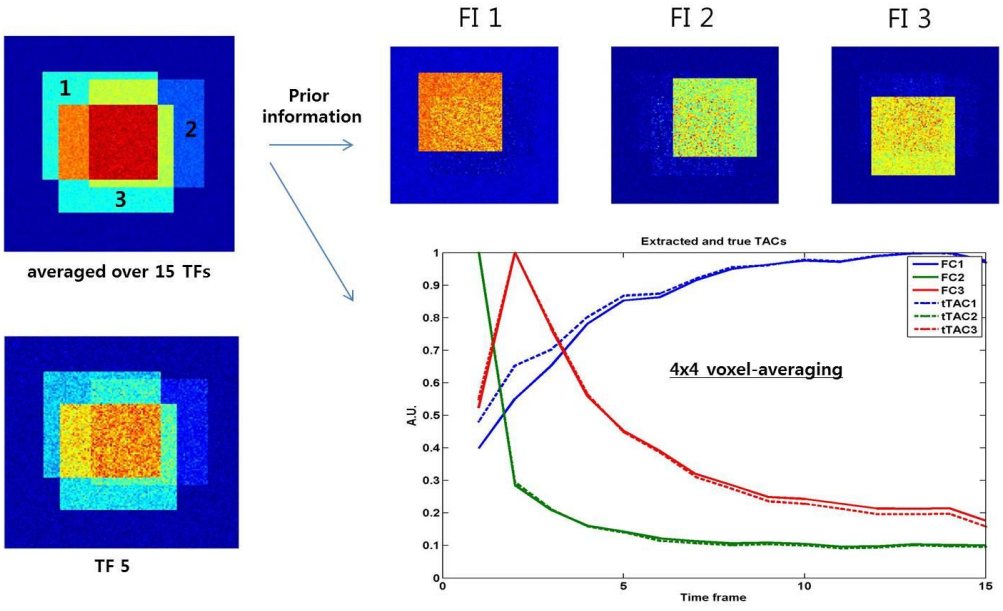

Figure 3.18. Same as figure 3.16 except for the noisy (case III) dynamic dataset.

3.6 Statistical Study: effect of prior information

To better understand the affect of prior information, a statistical study is performed on the accuracy D parameter (defined by equation 2.27) using a total of 5000 noisy (case II) datasets. The FADS technique (with $q = 3$ and 4×4 VA option) is applied to those datasets with and without prior information. Figure 3.19 shows the histograms of accuracy parameter for both the warm (red color) and the random (blue color) starting options. To better illustrate the meaning of D, an example with a D value of 0.1 is selected from the ensemble of the statistical study (see figure 3.19). Figure 3.20 shows the resulting factor images and curves, and they are compared against the known factor images and curves. The figure format is the same as figure 3.16.

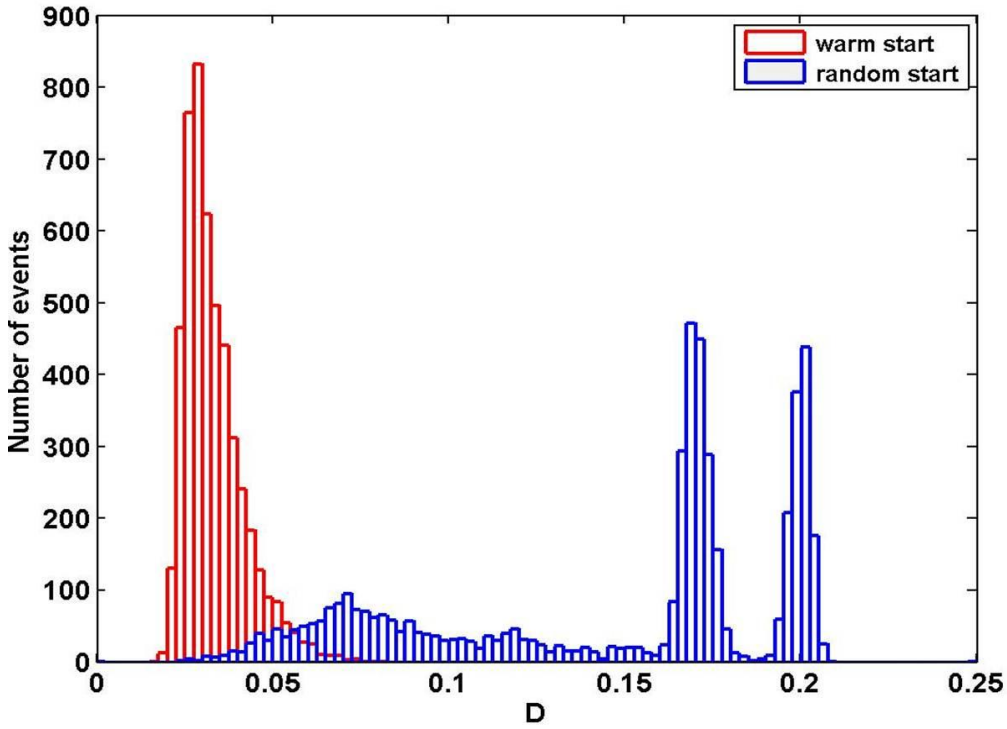

Figure 3.19. Shown is the result of statistical study on the accuracy D (defined by equation 2.27) using a total of 5000 noisy (case II) datasets. The proposed FADS technique (with $q = 3$ and 4×4 VA option) is applied to those datasets with and without the prior information. The red and blue colors indicate warm and random starting options, respectively. The D values for the warm starting case (with prior information) are much lower than those of the random starting case (without prior information). See text for details.

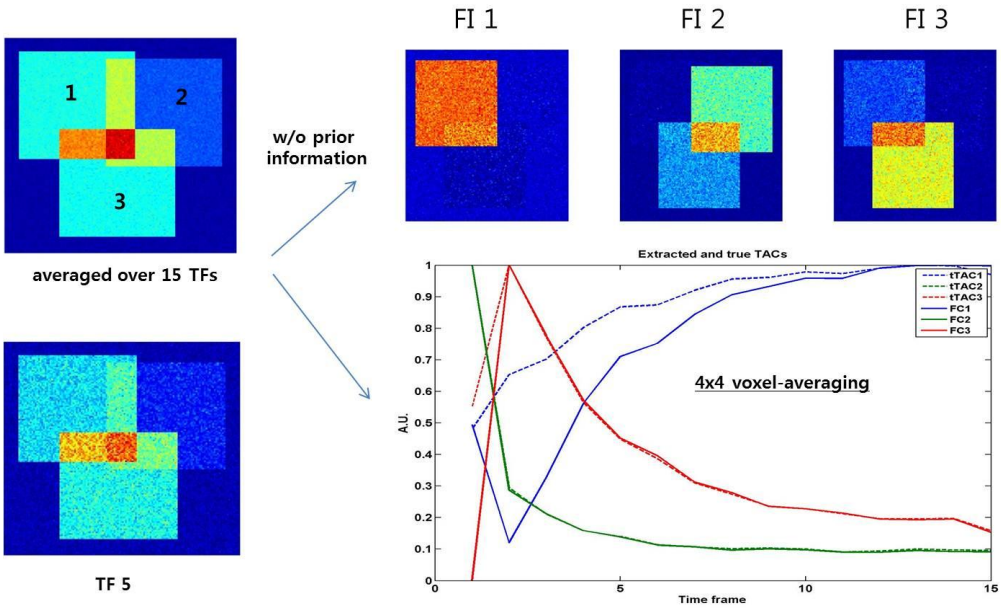

Figure 3.20. Shown is an example of extracted factor images and FC's, corresponding to D value of 0.1, from the ensemble of the statistical study for the noisy (case II) dynamic dataset. The figure format is the same as figure 3.16. See text for details.

3.7 FADS: 2 underlying kinetics

The FADS technique decomposes the dynamic dataset based on the shapes of underlying kinetics (or the different physiological functions). Figure 3.21 illustrates this point by having only two unique TAC's in the noisy (case III) dynamic dataset: compartment 2 is filled with TAC3 at 30% of the maximum intensity to simulate the two underlying kinetics in the dataset. The figure format is the same as figure 3.16 except that there are only two (instead of three) factors present in the dataset. As expected, compartment 2 and 3 are classified as a single factor, but the intensity of compartment 2 is much lower than that of compartment 3. The extracted FC's are comparable to the true underlying kinetics.

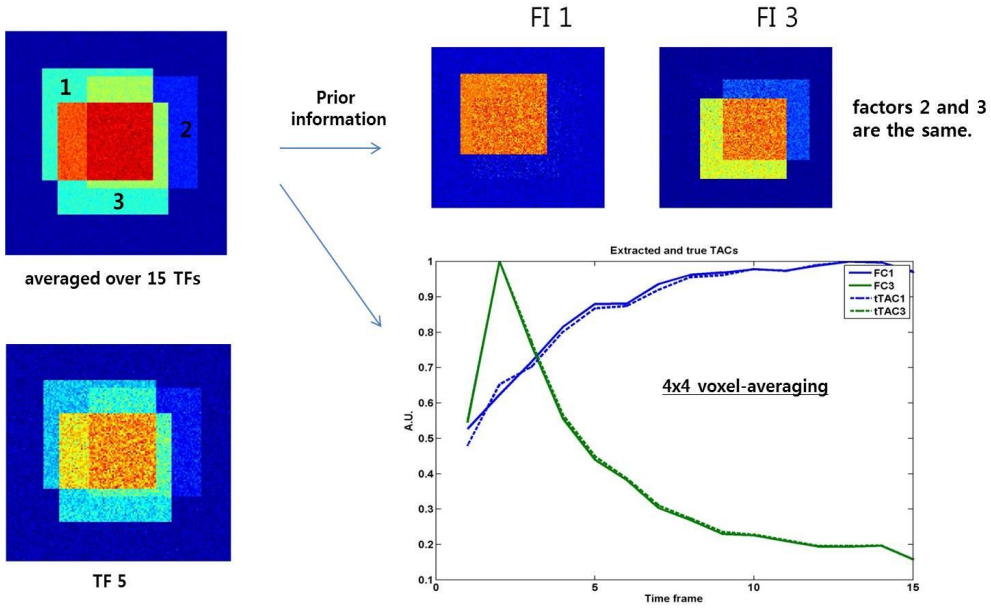

Figure 3.21. Shown are the extracted factor images and FC's for the noisy (case III) dynamic dataset (with only 2 unique underlying kinetics). The figure format is as for figure 3.16 except that there are only 2 factors present in the dataset. The compartment 2 in this phantom is filled with TAC3 (at 30% of its maximum intensity). Notice that the factor 2 image contains both compartments 2 and 3 (with lower intensity). The extracted FCs are comparable to the true underlying TAC's.

3.8 FADS: effect of voxel-averaging size

The proposed FADS technique is applied to the noisy (case II) dynamic dataset as a function of the VA size. The dynamic dataset is assumed to have 3 factors and the sample TAC's used to warm start the optimization are very similar to the noise-reduced TAC's in figure 3.12. Figure 3.22 shows the accuracy values (defined by equation 2.28) as a function of the VA size. Notice that the worst result is obtained without any application of VA technique. The best result is obtained for the 8×8 VA size. Figure 3.23 and 3.24 depicts extracted factor images and associated factor curves for the noisy dataset as a function of VA size, respectively. In figure 3.23, images in each row represent the FI's obtained for different VA size. Notice that the factor images in the top row contain mixed compartments. The FADS results

improves with the application of VA, however, the results degrade if the VA size is too large. For example, the loss of contrast is observed in the factor 1 images for 48 $\times$ 48 and 72 $\times$ 72 VA option. In figure 3.24, plots in each row represent FC's obtained for various VA size. The blue, green, and red curves indicate FC1, FC2, and FC3. In each plot, the true TAC (e.g. tTAC1, tTAC2, and tTAC3) is also displayed in the background. Both FC's and tTAC's are normalized (by the maximum value of each curve) for ease of comparison. Notice that the worst result is obtained without any VA technique. It is also evident that the difference between the FC's and tTAC's becomes noticeable as the VA size gets too large (e.g. 48 $\times$ 48 and 72 $\times$ 72).

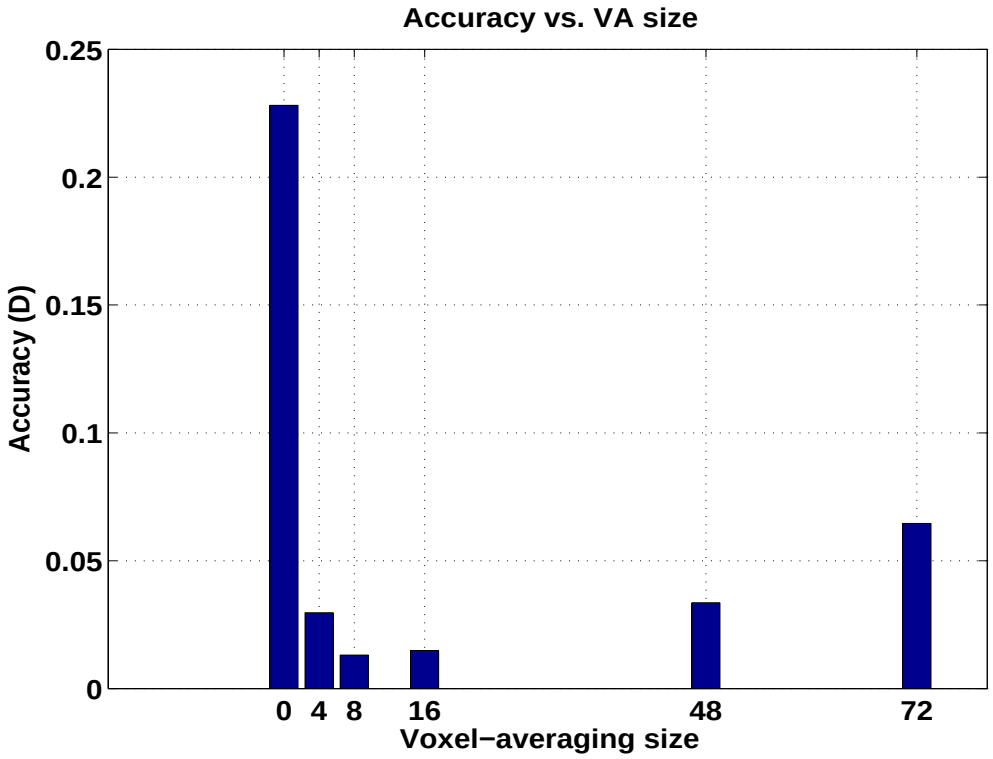

Figure 3.22. Shown is the effect of VA on the accuracy (D) values using the FADS result (with q=3 and prior information) for the noisy (case II) dynamic dataset. Note that the 8 $\times$ 8 VA option produces the best result. See text for details.

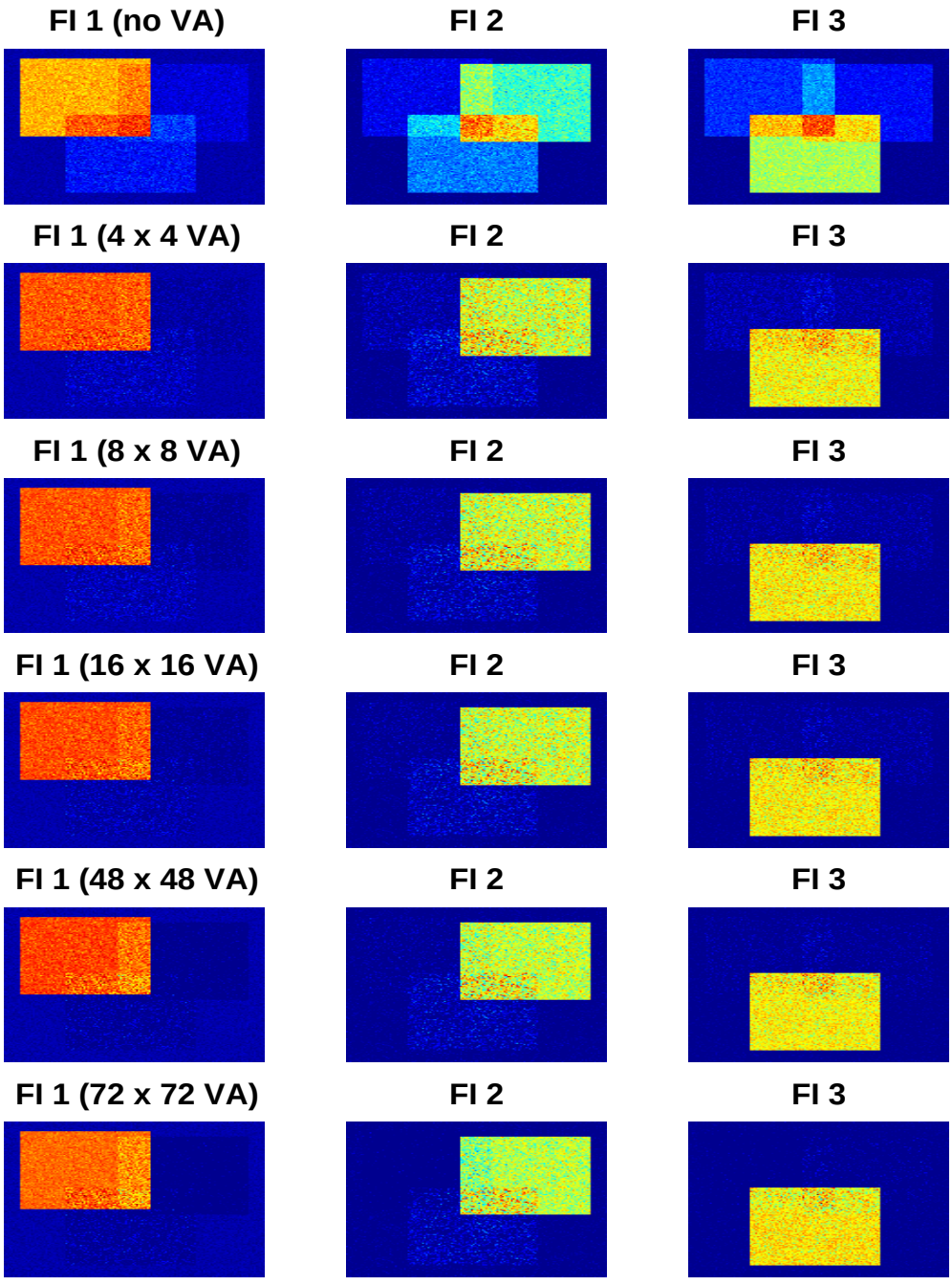

Figure 3.23. Shown is the effect of VA on the FADS result (i.e. factor images) for the noisy (case II) dynamic dataset. The images in the top and bottom rows represent factor images without VA option and 72 $\times$ 72 VA option, respectively. See text for details.

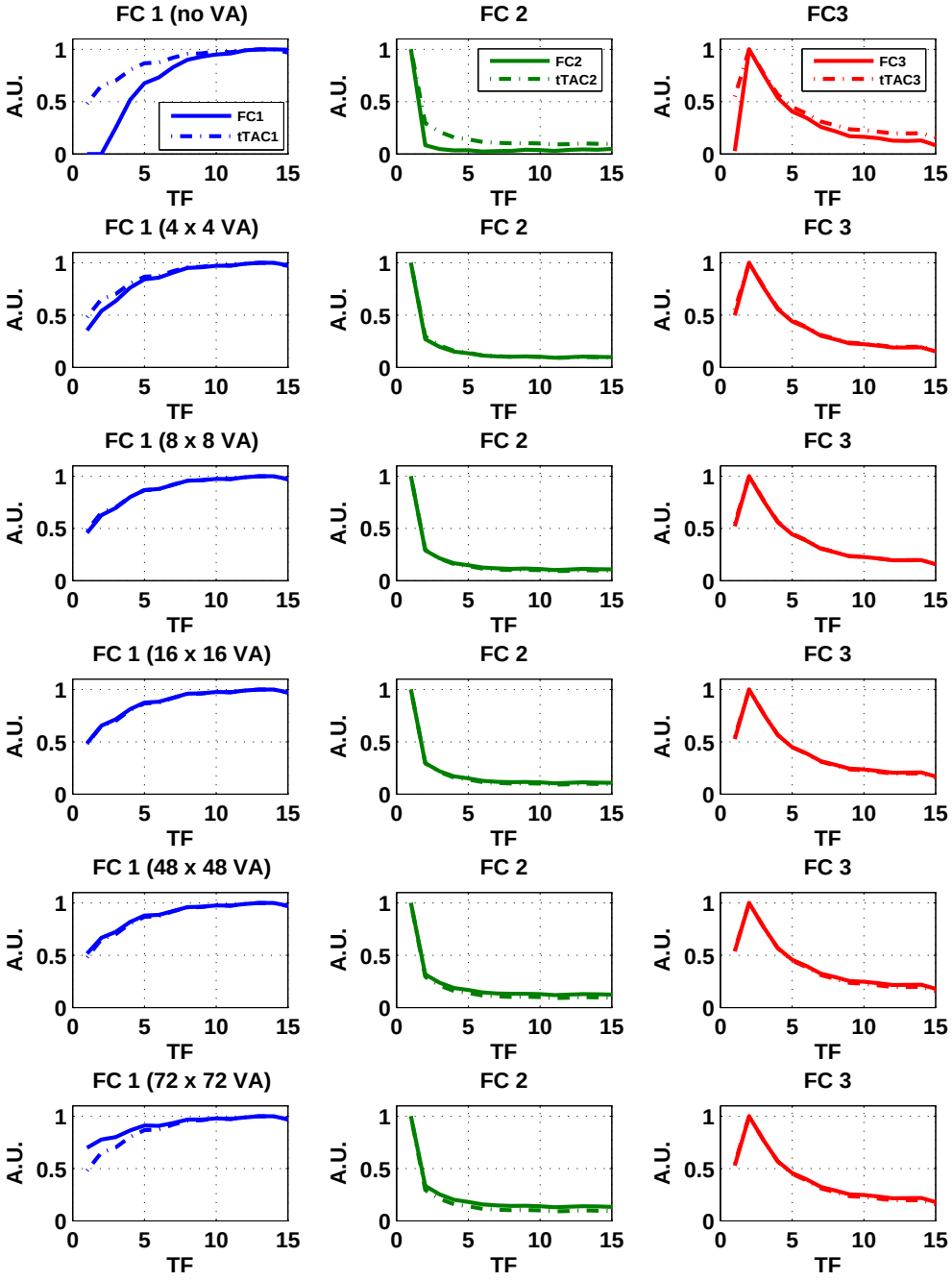

Figure 3.24. Shown is the effect of VA on the FADS result (e.g. factor curves) for the noisy (case II) dynamic dataset. The plots in the top and bottom rows represent factor curves without VA option and 72 $\times$ 72 VA option, respectively. See text for details.

3.9 FADS: improper estimation of *q*

Proper estimation of q for the factor model is crucial step for the successful FADS analysis. In this study, the proposed FADS technique is applied to the noisy (case II) dynamic dataset assuming q=4. The 4 $\times$ 4 VA option and the sample TAC's (similar to nrTAC's in figure 3.12) are used. Figure 3.25 shows the extracted FI's (top four images) and the associated FC's (bottom right plot). The initial starting point for the extra factor is produced using a random number generator (see bottom left plot). It is evident that the extra factor represents noise in the dataset. The first three FC's resemble the true TAC's. In figure 3.26, the format is same as figure 3.25 except the sample TAC for the fourth factor (e.g. obtained from the different region in the compartment 3). Notice that the nrTAC3 and nrTAC4 in the bottom left plot are very similar. By comparing the extracted factor images and factor curves against the known images and the true TAC's it is evident that the factors 3 and 4 are the same.

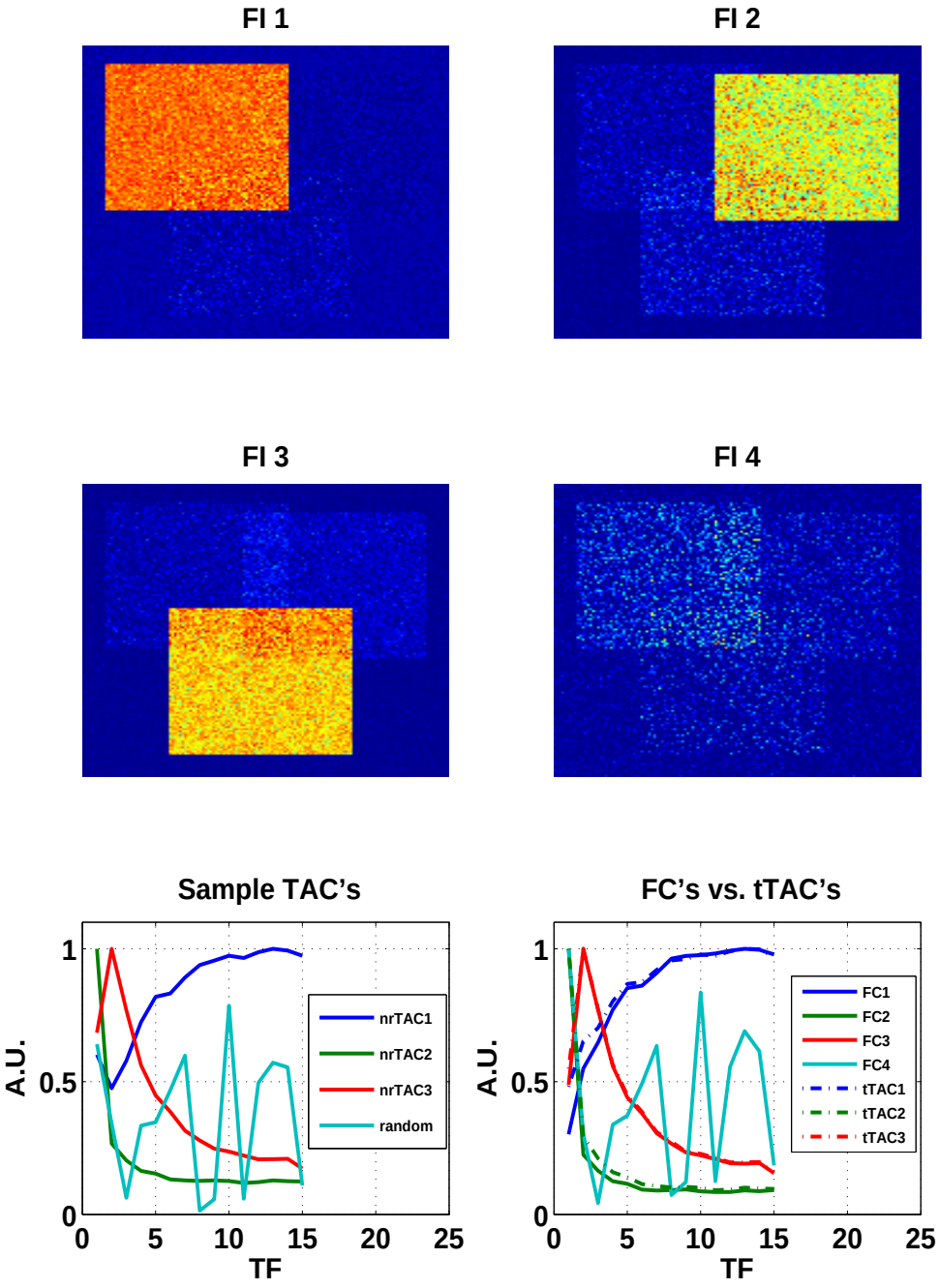

Figure 3.25. Shown is the effect of VA on the accuracy (D) values using the FADS result (with prior information) for the noisy (case III) dynamic dataset.

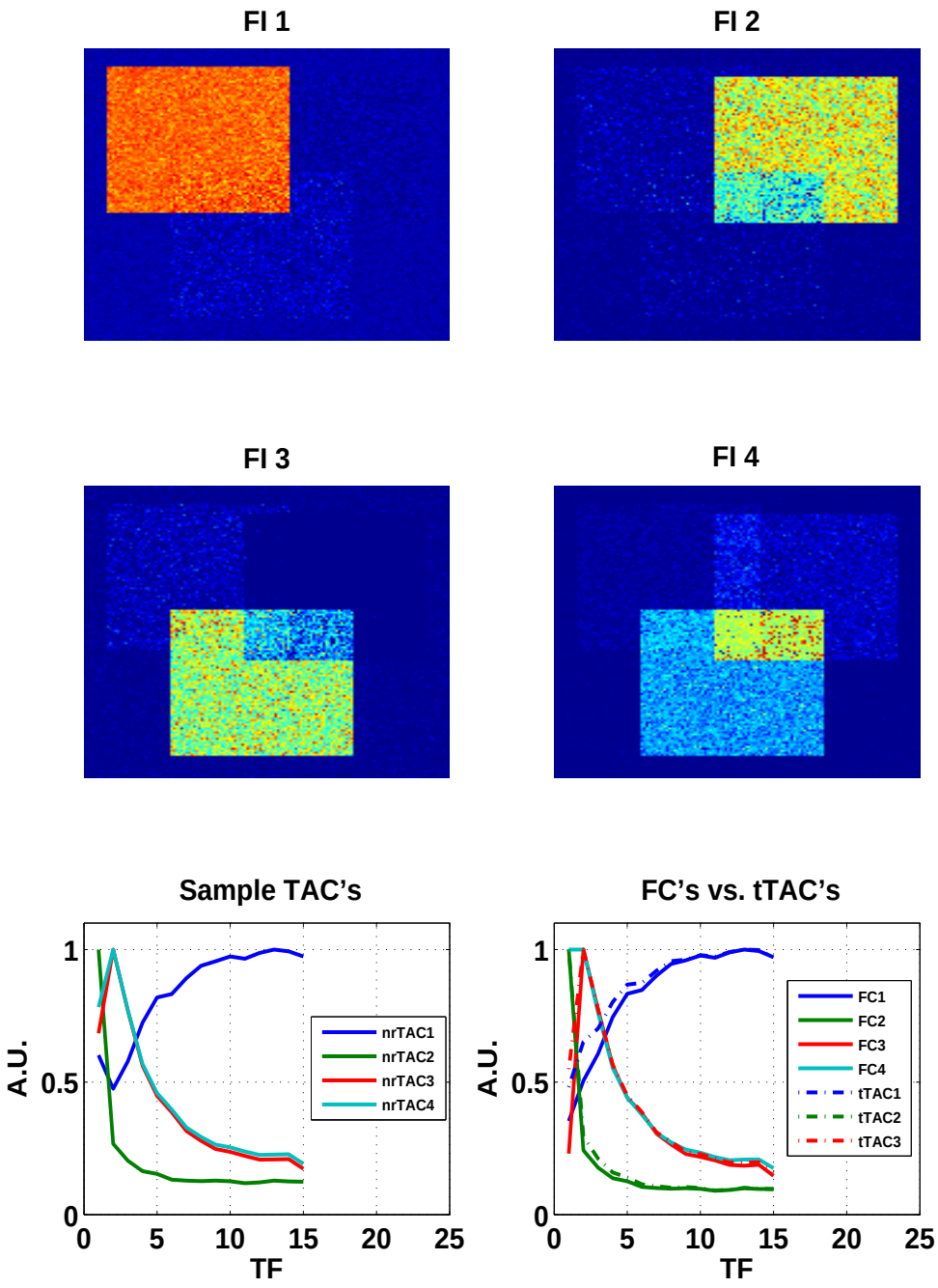

Figure 3.26. Shown is the effect of VA on the accuracy (D) values using the FADS result (with prior information) for the noisy (case III) dynamic dataset.

3.10 Least-Square Error: effect of voxel-averaging size

Finally, the least square error (defined by equation 2.5) is computed as a function of the VA size using the noisy (case II) dataset with and without prior information. Since the most time consuming and important part of the algorithm is finding the optimum factor curve matrix in the first stage of the optimization, the investigation is focused on the first stage optimization. Table 3.1 summarizes the result. By increasing the size of VA, the SNR of the dataset is improved, and the least square error is reduced.

Table 3.1. Shown are the least square errors (defined by equation 2.5) as a function of the size of VA using the noisy (case II) dynamic dataset. The computed errors are only from the first-stage of the dual-stage optimization. See text for details.

	4×4 VA	8×8 VA	16×16 VA	48×48 VA
Warm start	4.286E-4	1.220E-6	4.928E-7	2.989E-9
Random start	4.440E-4	1.412E-6	7.318E-8	3.238E-9

Figure 3.27 depicts the least-squares errors of the first-stage optimization for the noisy (case II) dataset (assuming $q = 3$ with 4×4 VA option) as a function of iteration number for both the random and the warm starting options. The red and the blue curves represent the random (without prior information) and the warm (with prior information) starting options, respectively. The least-square error decreases nearly exponential for both starting options.

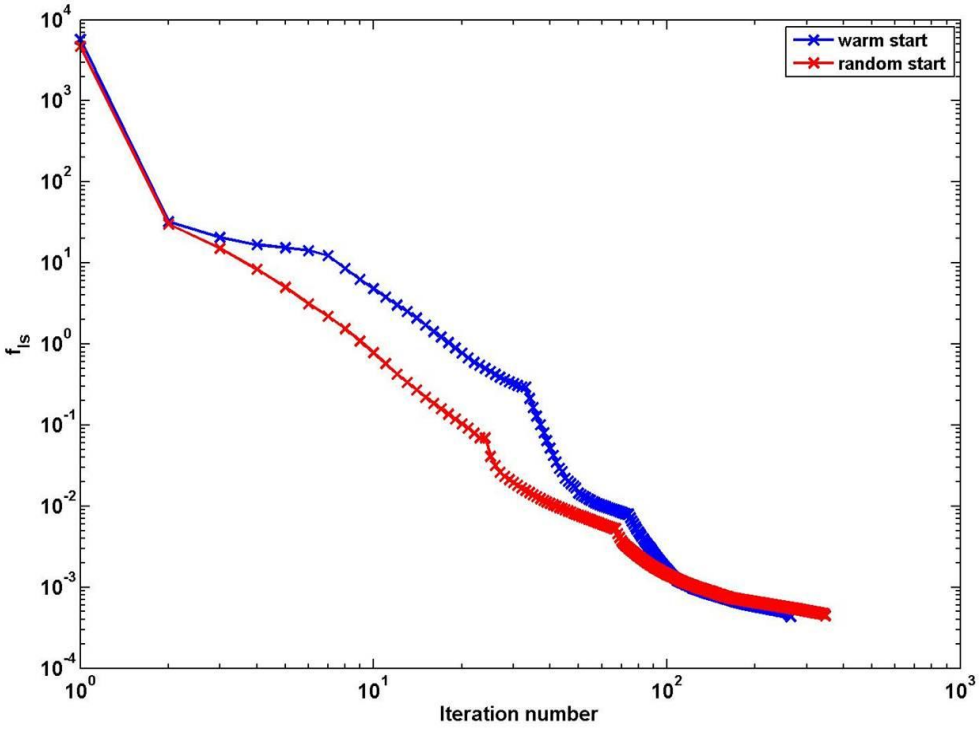

Figure 3.27. Shown are the least-square errors of the first stage optimization for noisy (case II) dataset as a function of iteration number. The red and the blue curves represent the random and the warm starting options, respectively.

Chapter 4

Results II (Clinical Study)

4.1 Parkinson's Disease (PD)

A total of 60 subjects (20 healthy and 40 diagnosed with PD) will undergo dynamic PET scans with [^{11}C]-Dihydrotetrabenzine (DTBZ) radio-tracer. At the time of writing this thesis, only 10 dynamic PET datasets (4 healthy and 6 diseased subjects) were available for analysis. However, two subject datasets (dtbz5 and dtbz7) were removed from FADS analysis in this work due to a quality control failure that only became apparent after the subject's datasets were acquired. Each dataset consists of 720 images (45 slices $\times$ 16 TF's). These datasets are analyzed by the FADS technique. First, the results of FADS (extracted FV's and FC's) from the two dynamic datasets in the healthy and diseased groups are shown and explained in detail. Then, the results from the rest of the DTBZ datasets are discussed and summarized. Figure 4.1 shows a slice of (DTBZ) dynamic PET brain scan for a healthy subject and a cartoon of anatomical structures for the corresponding slice in the brain. The intense uptake of the radiotracer is observed in the tissues of Nucleus caudatus and Putamen. Dopaminergic neurons are mainly located in these tissues and they are collectively refereed to as the striatum tissues.

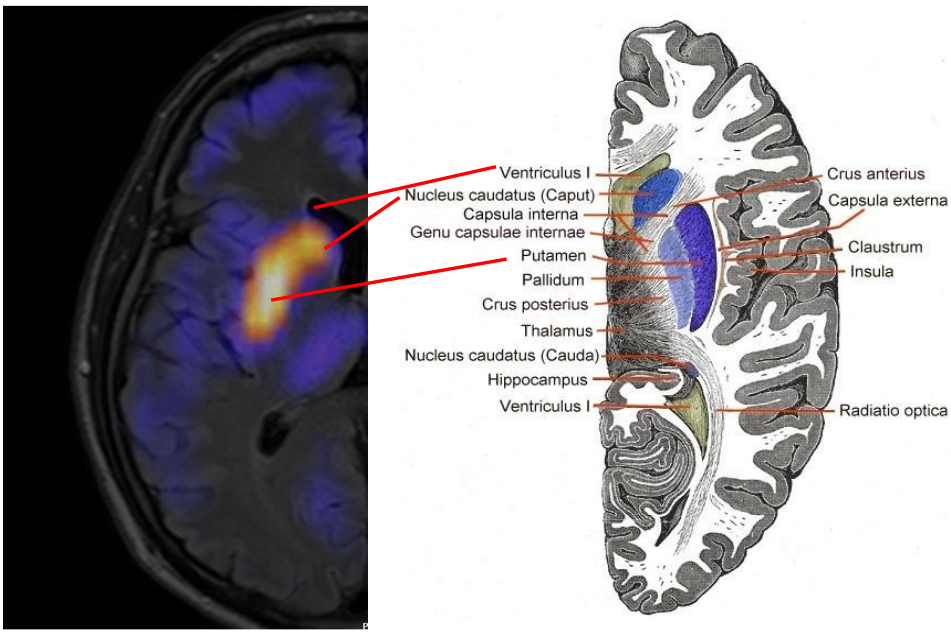

http://en.wikipedia.org/wiki/caudate_nucleus

Figure 4.1. This figure depicts a slice of (DTBZ) dynamic PET brain scan for a healthy subject and a cartoon of anatomical structures for the corresponding slice in the brain. See text for details.

Figure 4.2 and 4.3 show images of time-averaged (transverse) slices of the brain (near substantia nigra) for the healthy and diseased subjects, respectively. The time-averaged (TA) PET volumes are normalized to one, and only six (out of 45) TA slices are shown from each group. In figure 4.2, two nearly identical (left and right) intense lobes in the mid-region of the brain are observed. The two intense lobes and the surrounding tissues around the lobes represent the striatum and non-striatum tissues, respectively. For a healthy subject, the striatum tissues are easily identifiable. For a diseased subject, it is quite difficult to identify the region corresponding to the striatum tissues (see Figure 4.3). Current methodology [62, 63] to detect patients with early PD involves the manual identification of the striatum and non-striatum tissues. The placement of multiple ROI's in those regions are highly undesirable because the analyst has to go through multiple slices to identify a single structure.

Clearly, such a process can be complex, time-consuming and operator-dependent. In comparison to figure 4.2, the relative uptake of the non-striatum tissues for the diseased subject is significantly higher than that for the healthy subject.

Figure 4.4 shows images of slice 21, as a function of TF's (or scan time in minutes) for a healthy subject (dtbz6), see figure 4.2. To be consistent with the other figures, the dynamic PET volume is normalized to one. The uptake of striatum tissues begins to appear at TF 3, and reaches a maximum intensity value near TF 8. The relative uptake of the non-striatum tissues, in comparison to the striatum tissues is much lower for almost all TF's. Figure 4.5 depicts images of slice 27, as a function of TF's (or scan time in minutes) for the diseased subject (see figure 4.3). The figure format is the same as figure 4.4. For the diseased case, there is inconsistent uptake pattern in the dynamic images. The identification of the striatum tissues from the non-striatum tissues is quite difficult due to the following reasons: the non-striatum tissues have relatively high uptake; the two lobes in the substantia nigra have distorted shapes with varying intensities. The non-striatum tissues have higher uptake of the tracer during the early TF's (4-8) and lower uptake of the tracer at the later TF's (13-16). These facts can make the quantitative analysis of dynamic [^{11}C]-DTBZ datasets very difficult (especially for diseased datasets).

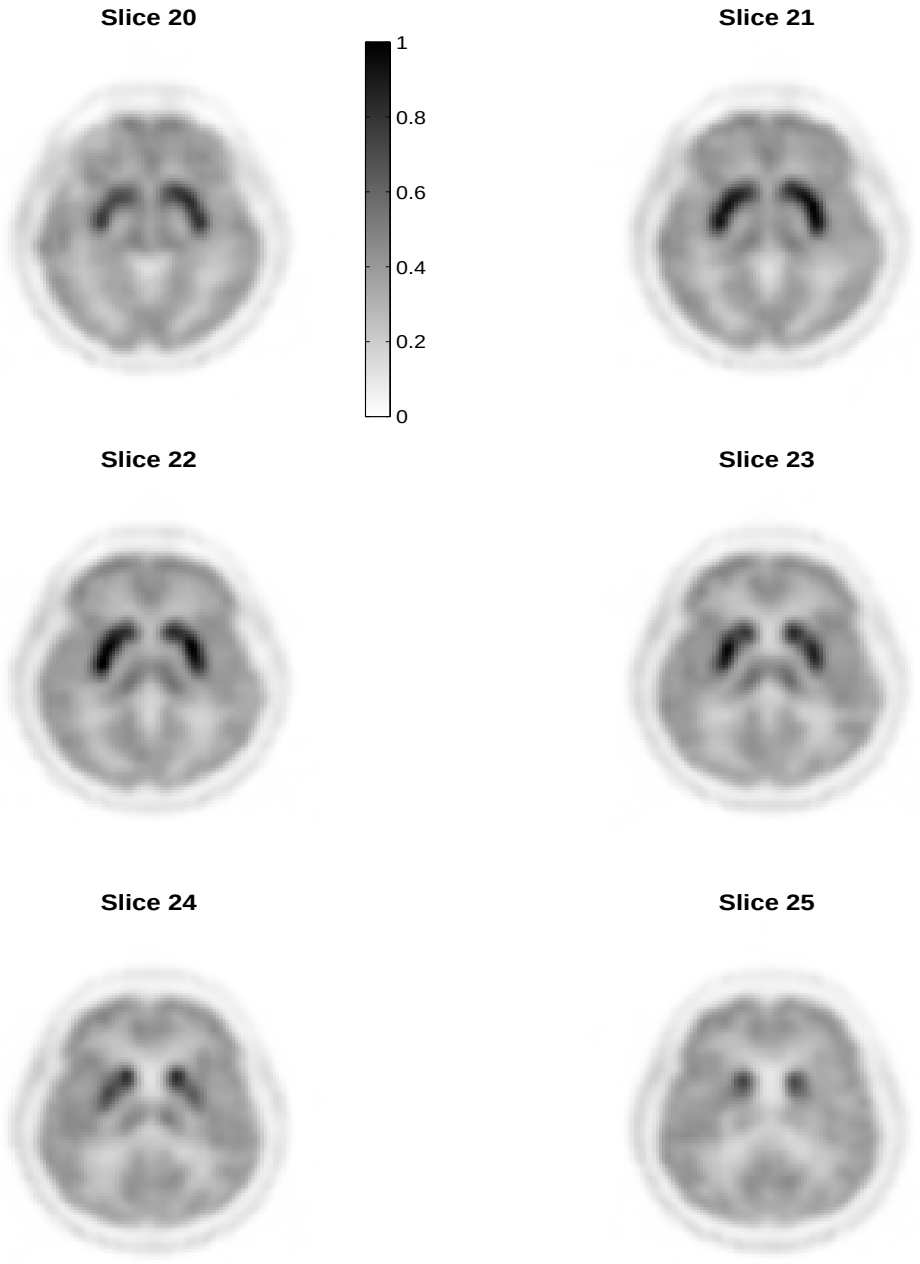

Figure 4.2. Shown are the images of time-averaged (transverse) slices near substantia nigra in the center of brain for a healthy subject (dtbz6). The TA PET volume is normalized to one, and only six (out of 45 TA) slices are shown. Notice that the presence of two nearly identical (left and right) intense lobes in the mid-region of the brain. The uptake in the striatum tissues stands out from the non-striatum tissues.

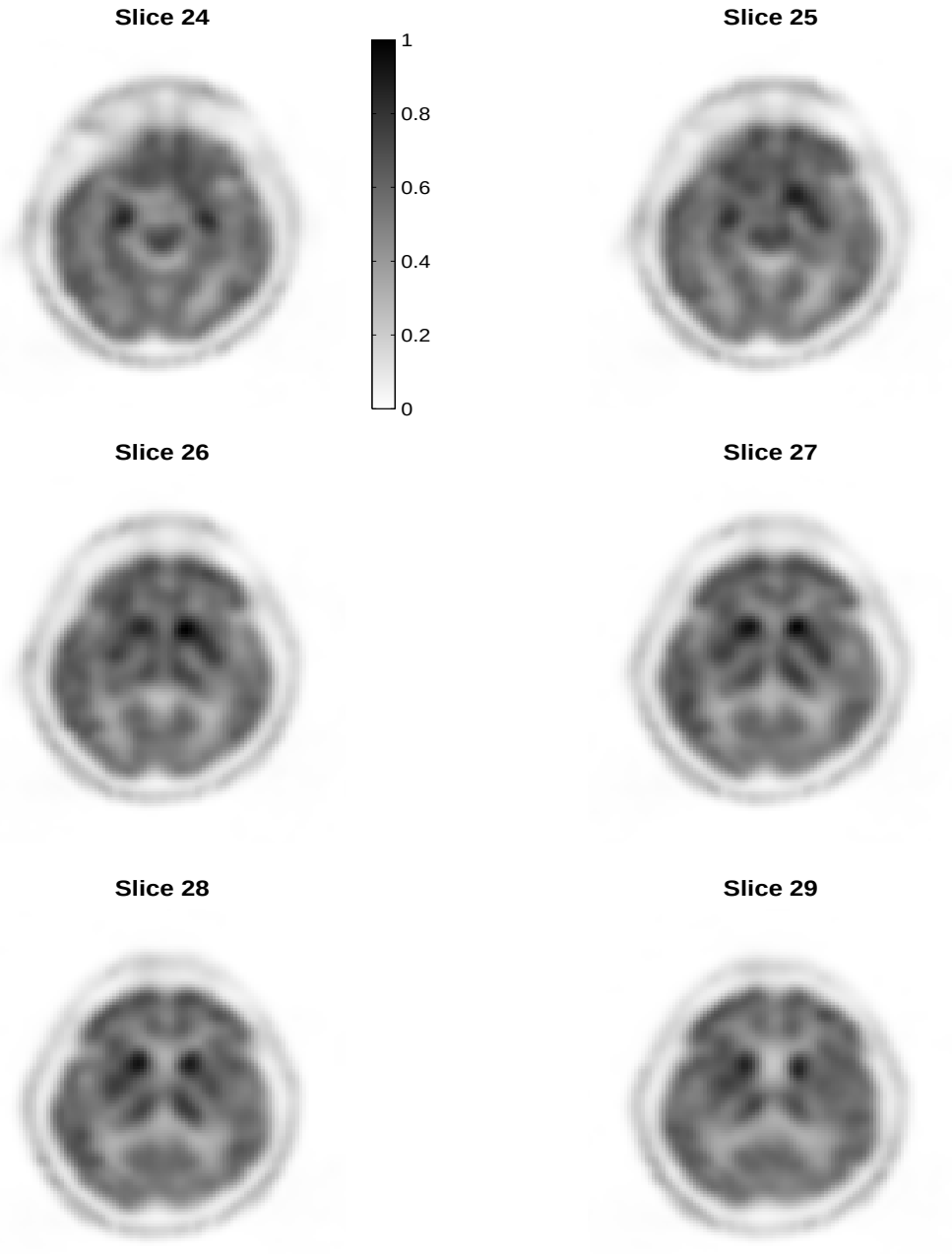

Figure 4.3. Same as figure 4.1 except for a diseased subject (dtbz8). Unlike figure 4.1, it is difficult to identify two nearly identical (left and right) lobes in the mid-region of the brain. The uptake of the non-striatum tissues is relatively high, in comparison to that of the striatum tissues.

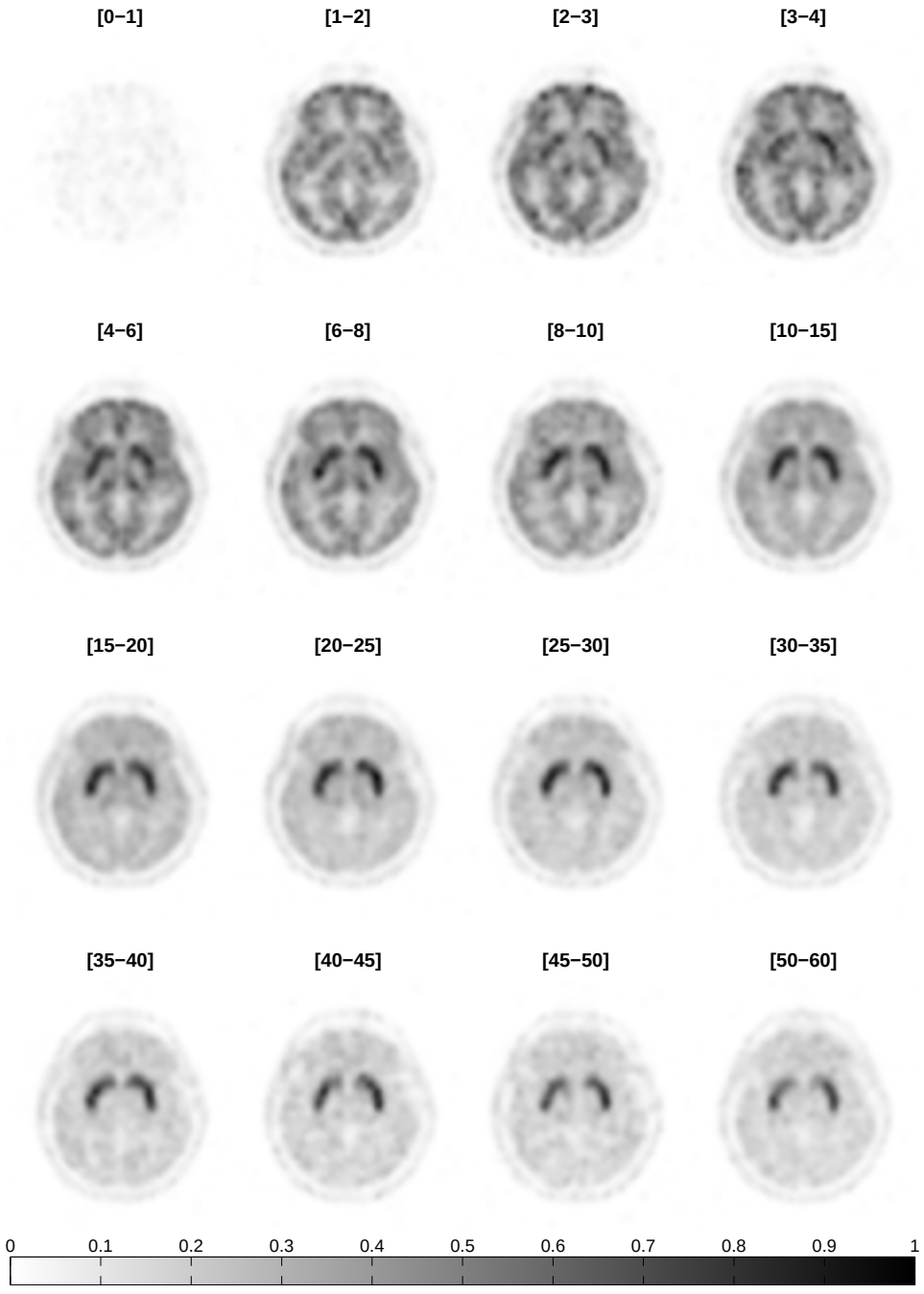

Figure 4.4. Shown are images of (transverse) slice 21, as a function of TF's for a healthy subject (dtbz6), see figure 4.1. The uptake of the striatum tissues begins to appear at TF 3, and reaches maximum intensity around TF 8. Notice that the uptake of the non-striatum tissues in comparison to that of the striatum tissues is relatively low.

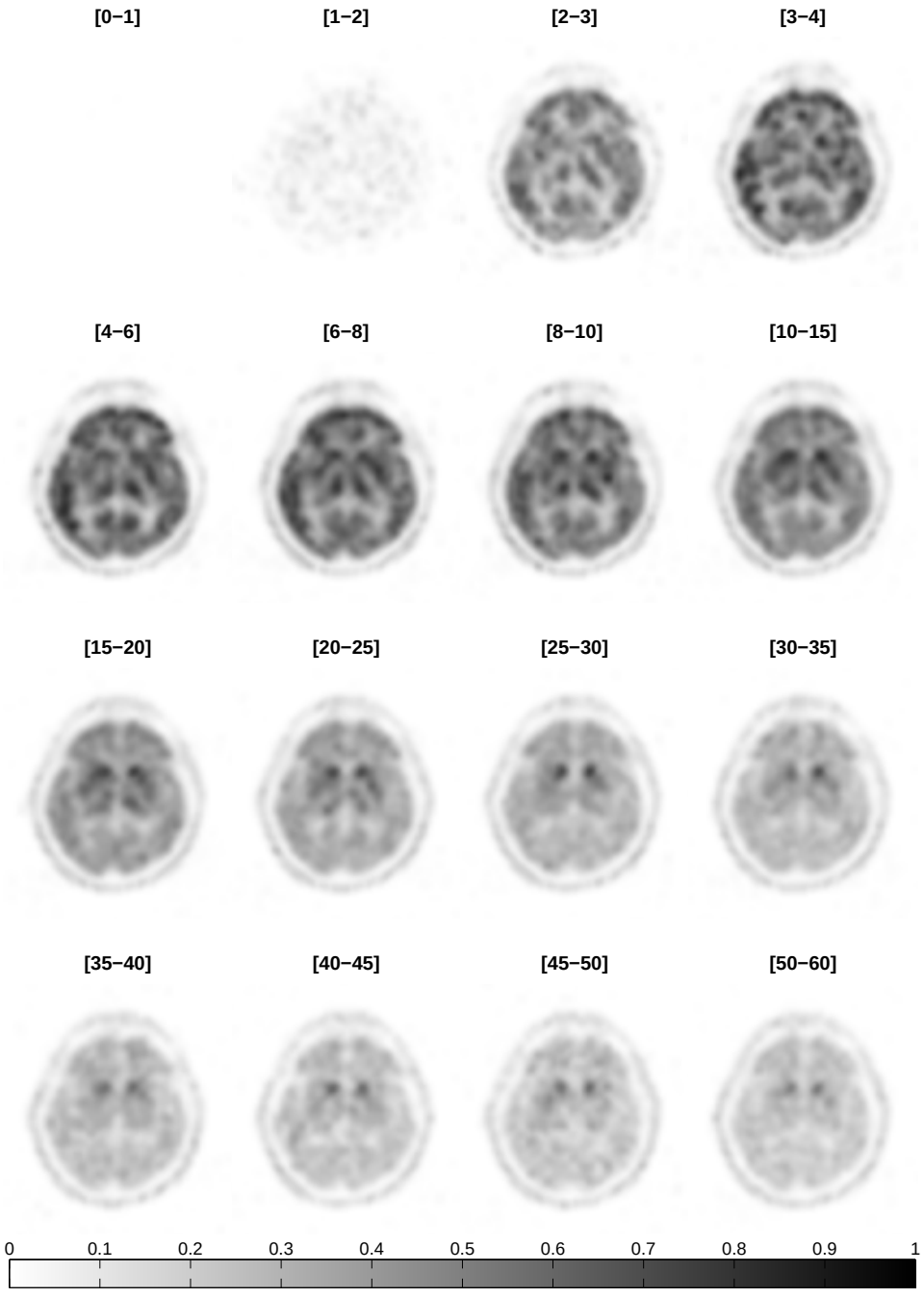

Figure 4.5. Same as figure 4.3 except for a diseased subject (dtbz8), see figure 4.2. Unlike figure 4.3, the uptake of the striatum tissues (two nearly identical left and right lobes) is nearly non-existent. The uptake of the non-striatum tissues in comparison to that of the striatum tissues is relative high. Clear identification of the striatum tissues is nearly impossible, and there is very low uptake of the tracer in the images at the later TF's (13-16).

4.2 Estimation of q by SVD

Figure 4.6 shows the normalized singular values for a healthy (magenta X's) and a diseased (blue O's) datasets. To improve the SNR's of the datasets, the $2 \times 2 \times 1$ (in-plane) VA technique is applied to the datasets before performing SVD. For both datasets, two distinct singular values ($q = 2$), corresponding to the two different factors. As discussed before, proper estimation of the factor number (q) is a crucial step for successful FADS.

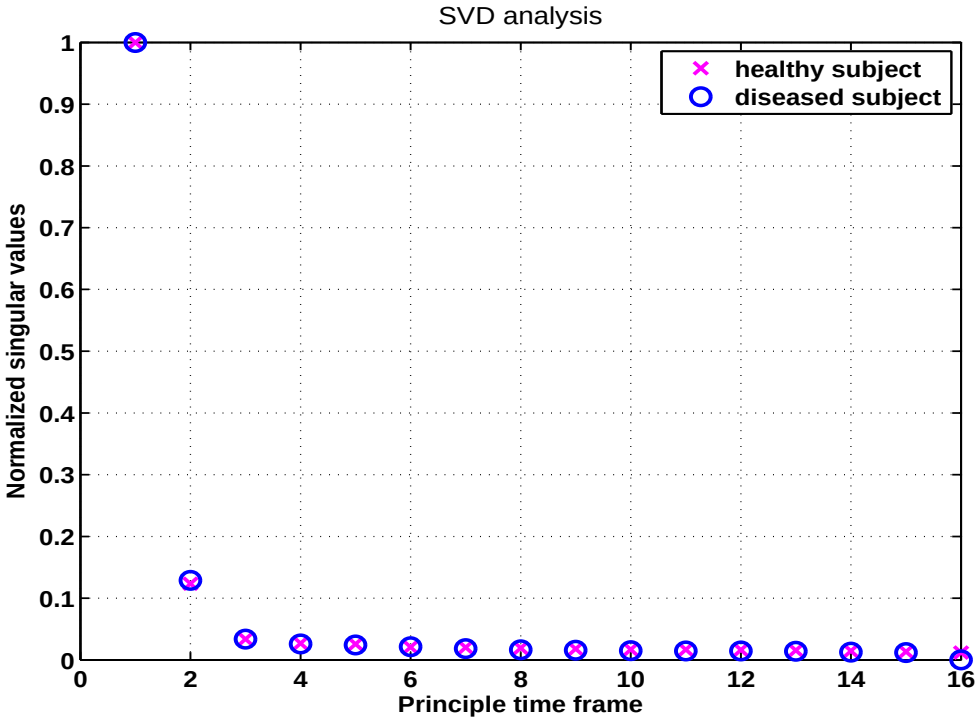

Figure 4.6. Shown are the normalized singular values from datasets for a healthy (magenta X's) and a diseased (blue O's) subjects. Notice that two distinct singular values ($q = 2$), corresponding to the two different factors.

4.3 Prior Information

One major difference between the proposed FADS algorithm and other well-known FADS techniques is the use of prior information. In the proposed FADS algorithm, well-known information about the dataset is used to warm start the first stage of the

dual-stage optimization. This has the effect of reducing the number of possible solutions, and the obtained solution is much closer to the global minimum (see section 3.5 and 3.6). According to figure 4.6, the two ^{11}C-DTBZ datasets can be modelled assuming 2 factor system, and for each dataset, two sample TAC's are obtained from the noise-reduced and time-averaged PET volume using prior information (e.g. the striatum and non-striatum tissues). Figure 4.7 shows normalized sample TAC's produced by the standard ROI method from the striatum and the non-striatum tissues for both a healthy (dashed curves) and a diseased (solid curves) subject. The blue and the red curves represent the striatum and the non-striatum tissues, respectively. From our experience the algorithm is rather insensitive to the position and the size of the ROI's for the striatum and the non-striatum tissues. For example, the ROI's for the striatum and the non-striatum tissues can contain mixed tissue information. However, the sample TAC's should not be identical to avoid the stalling of the optimization.

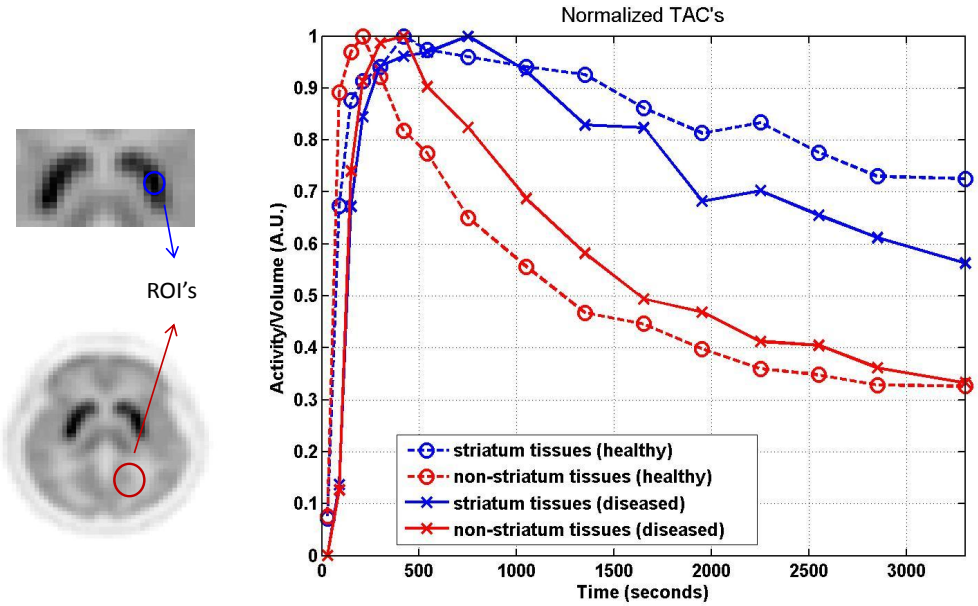

Figure 4.7. Shown are normalized sample TAC's produced by the conventional ROI method (based on prior information) from the striatum and the non-striatum tissues for both a healthy (dashed curves) and a diseased (solid curves) subject. The blue and the red curves represent the striatum and the non-striatum tissues, respectively.

4.4 FADS (extracted FV's and associated FC's)

The standard ROI method for extracting accurate TAC's from different physiological structures is cumbersome and can be very complex. For instance, time-averaged PET volume has to be used to identify and delineate different (often 3-dimensional) physiological structures to create masks and then these masks are applied to each time frame to obtain time activity curves. During this process it is critical to exclude voxels that contain mixed tissue information and this step can be quite difficult for an operator. Due to a finite voxel size (64 mm^3) of the PET scanner, the PVE's and spillover effects exist and can be significant in the dynamic PET datasets. As a result, the extraction of "pure" TAC's from the dataset is often difficult to obtain. Fortunately, the proposed FADS technique automatically handles the partial volume effect. Figure 4.8 and 4.9 show images of the time-averaged (transverse)

slices and corresponding FV's produced by the FADS technique (assuming $q = 2$ with $2 \times 2 \times 1$ in-plane VA and two sample TAC's based on the prior information) for the healthy and diseased subjects, respectively. Since the PD is directly related to the tracer-uptake in the striatum tissues (region inside the substantia nigra) only slices that best represent these structures are shown. In figure 4.8, images in the left column show the time-averaged [20-24] slices, and the images in the center and the right columns show the associated factor 1 and 2 images, respectively. For ease of comparison, the time-averaged (TA) PET volume and FV's are normalized to one. It is clear that factors 1 and 2 represent the striatum and the non-striatum tissues, respectively. In factor 1 images, the uptake of the non-striatum tissues is relatively low in comparison to that of the striatum tissues. The format of figure 4.9 is the same as figure 4.8 but for a diseased subject, and the striatum tissues are located in slices [24-28]. In comparison to figure 4.8, the main difference in the uptake pattern of the factor 1 images is the distortion of the two lobes and relatively high uptake in the background (or non-striatum) tissues. As a result, manual identification of the striatum tissues is quite difficult, time-consuming and operator-dependent. In addition, the accurate placement of an ROI's around the tissue structure is likely to be inaccurate. The FC's associated with the healthy and diseased subjects (see figure 4.8 and 4.9) are displayed in the (left and right) plots in the third row of figure 4.10, respectively. The blue and the red curves represent the striatum and the non-striatum tissues, respectively. The uptake patterns of the non-striatum tissues between the two groups are comparable. However, for the healthy subject, the area under FC1 is much larger than that under FC2. For the diseased subject, areas under FC1 is slightly larger than that under FC2.

Figure 4.11 to 4.16 show images of the time-average (transverse) slices and the corresponding FV's produced by the FADS (using $q = 2$, $2 \times 2 \times 1$ (in-plane) VA technique and two sample TAC's based on the prior information) for the healthy and the diseased subjects. For all of the DTBZ datasets, the FADS technique produces

two FV's (corresponding to the striatum and non-striatum tissues) and two associated FC's. The format of each figure is the same as figure 4.8, and different slices from each dataset are chosen to best represent the near substantia nigra region. Figure 4.11, 4.15, and 4.16 represent factor images for the diseased subjects and their factor curves are shown in the top-left, bottom-left, and bottom-right plots of figure 4.10. Figure 4.12, 4.13, and 4.14 represent factor images for the healthy subjects and their factor curves are displayed in the top-right plot and (left and right) plots in the second row of figure 4.10.

In summary, both healthy and diseased datasets are decomposed into two factor volumes (corresponding to the straitum and the non-striatum tissues) and associated factor curves. For healthy subjects, intense uptake of the radiotracer in the striatum tissues (i.e. two left and right lobes) is consistently observed in the images of factor 1 volume. For diseased subjects, mild uptake of the radiotracer in the striatum tissues (e.g. area with intense uptake of the radiotracer varies among different diseased datasets) is consistently observed in the images of factor 1 volume. The main difference in the images of factor 1 volumes between the two groups is the relatively high background uptake of the radiotracer in the images of factor 1 volume for the diseased subject. The area under FC1 is much larger than that under FC2 for the healthy subjects whereas the are under FC1 is slightly larger than that under FC2 for the diseased subjects. Within each group, the extracted FC's are consistent and comparable. For diseased subjects, identification of the striatum tissues and the extraction of TAC's for the striatum tissues can be quite difficult. In addition, it is also likely that many of the voxels will consist of mixed tissue information (i.e. boundary of the striatum and the non-striatum tissues).

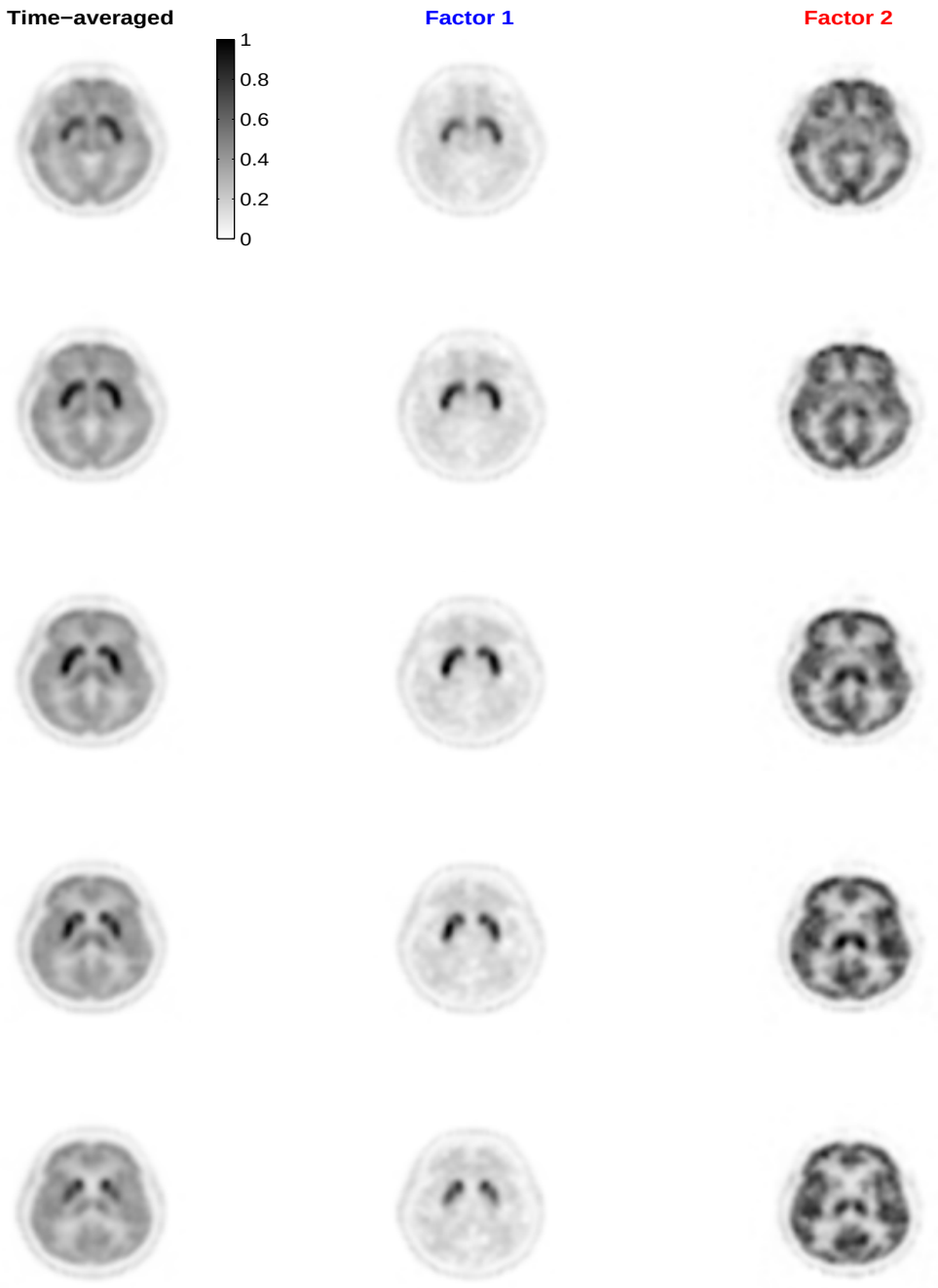

Figure 4.8. Shown are images of the time-averaged (transverse) slices and corresponding slices from the FV's for a healthy subject (dtbz6). Images in the left column show the time-averaged [20-24] slices, and the images in the center and the right columns show the associated factor 1 and 2 images, respectively. Associated FC's are displayed in figure 4.10. See text for details.

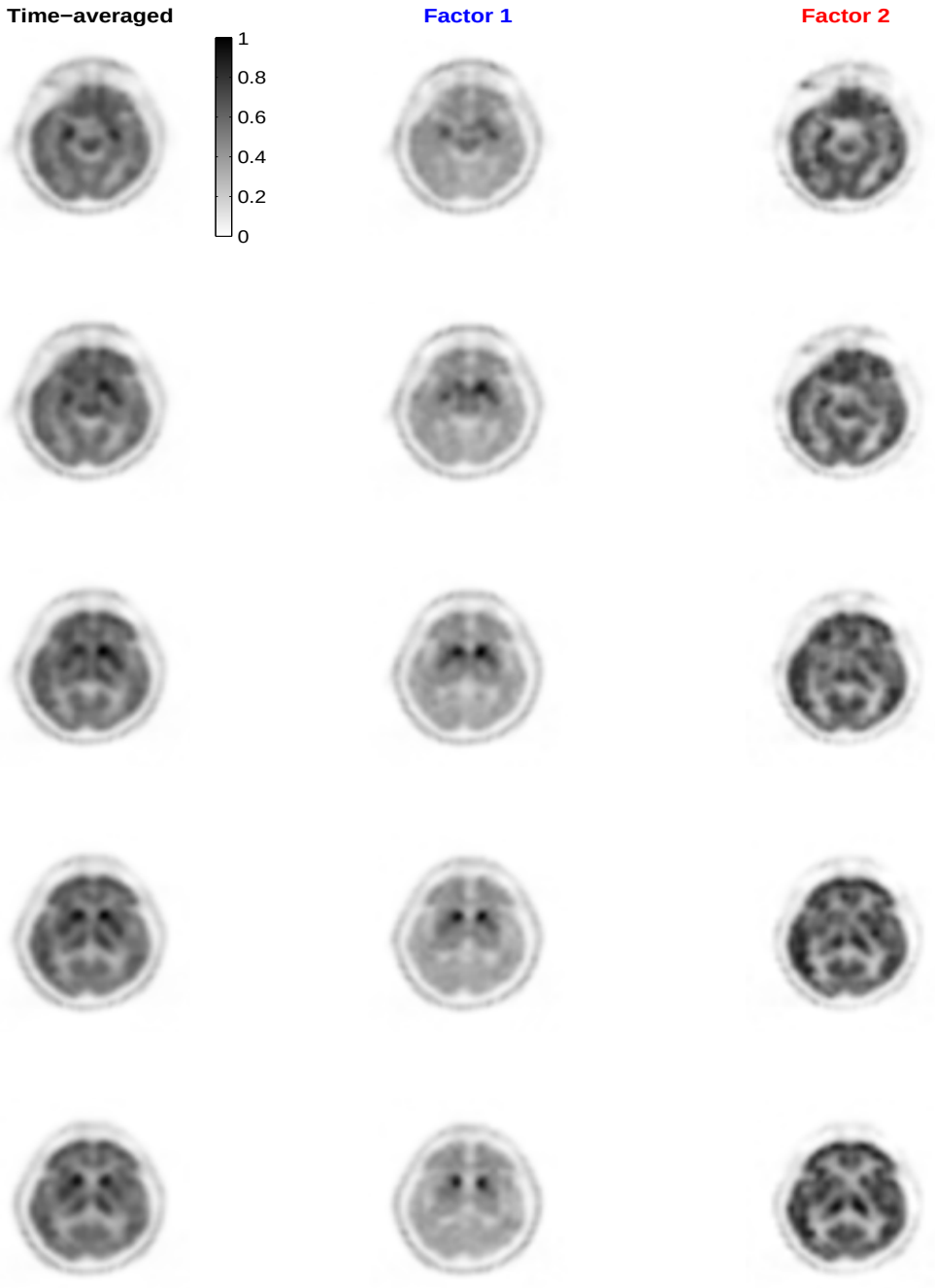

Figure 4.9. Same as figure 4.8 except for a diseased subject (dtbz8) with [20-24] slices. Factors 1 and 2 represent the striatum and the non-striatum tissues, respectively. In comparison to figure 4.8, there is clear distortion of the two lobes and relatively high uptake of the background tissues in the images of the factor 1 volume. Associated FC's are displayed in figure 4.10.

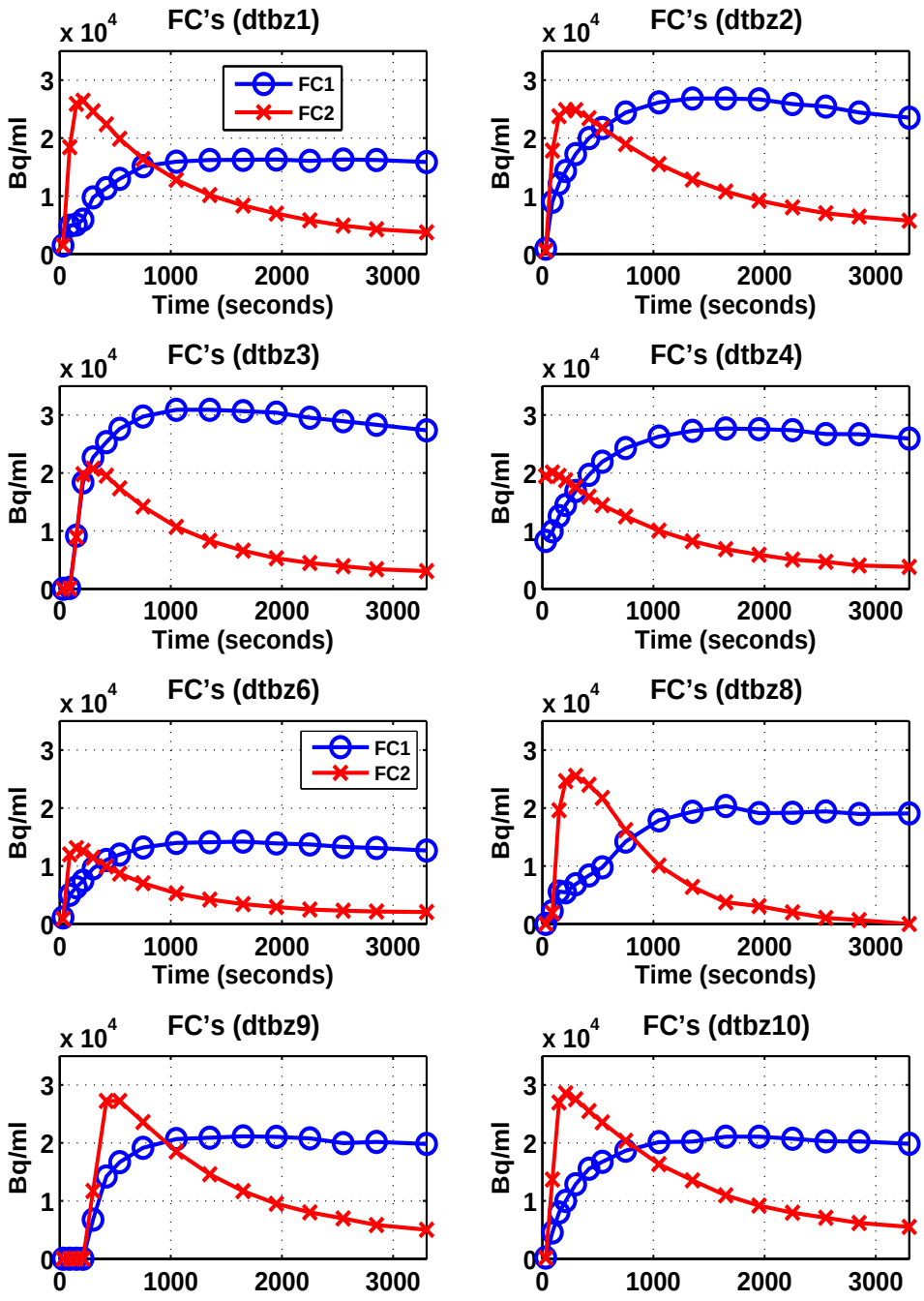

Figure 4.10. Shown are extracted FC's for the healthy (dtbz2-4 and dtbz6) and the diseased (dtbz1 and dtbz8-10) subjects. The blue and the red curves represent the striatum and the non-striatum tissues, respectively. The uptake patterns for the non-striatum tissues between the two groups are very similar. For the healthy subject, the areas under FC1 are much larger than that under FC2. For the diseased subject, the areas under FC1 are slightly larger than the areas under FC2.

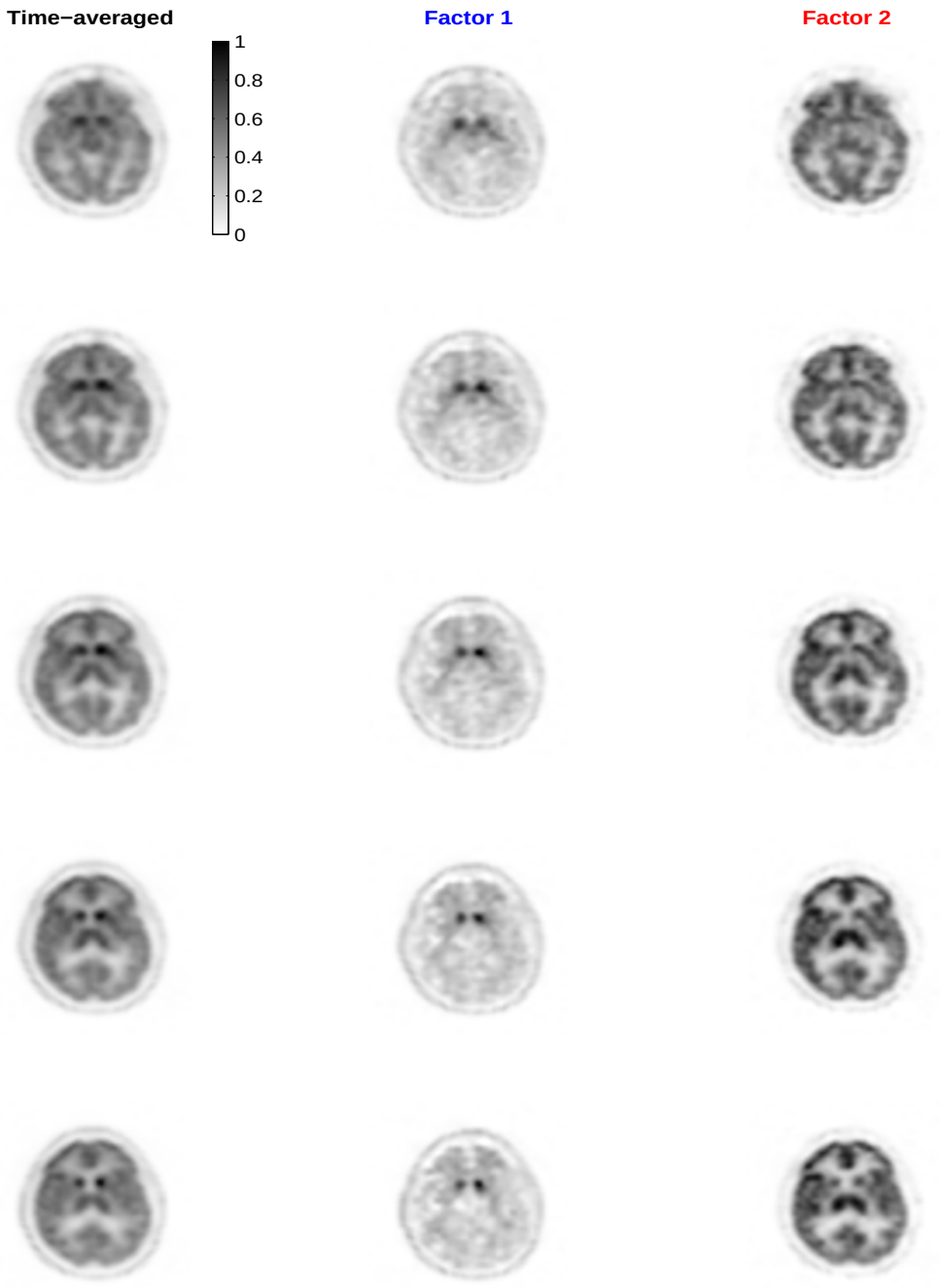

Figure 4.11. Same as figure figure 4.8 except for a diseased subject (dtbz1) with [21-25] slices. In comparison to figure 4.8, there are clear differences in the uptake pattern (e.g. distortion of the two lobes and relatively high background uptake) in the images of the factor 1 volume. Associated FC's are shown in figure 4.10.

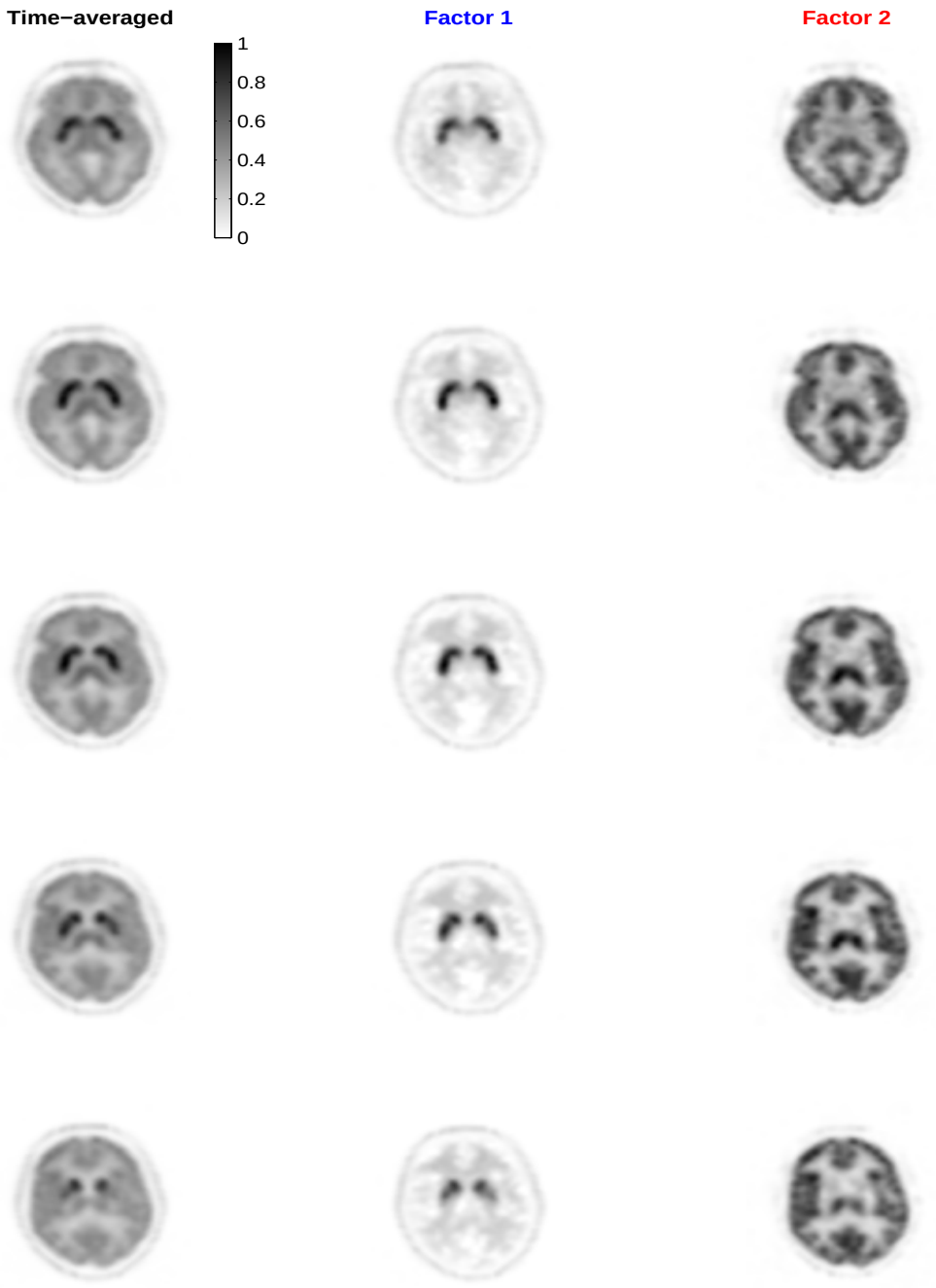

Figure 4.12. Same as figure 4.8 except for a healthy subject (dtbz2) with [22-26] slices. In comparison to figure 4.8, similar uptake pattern (e.g. shape of the two lobes and low background uptake) is observed in the images of the factor 1 volume. Associated FC's are shown in figure 4.10.

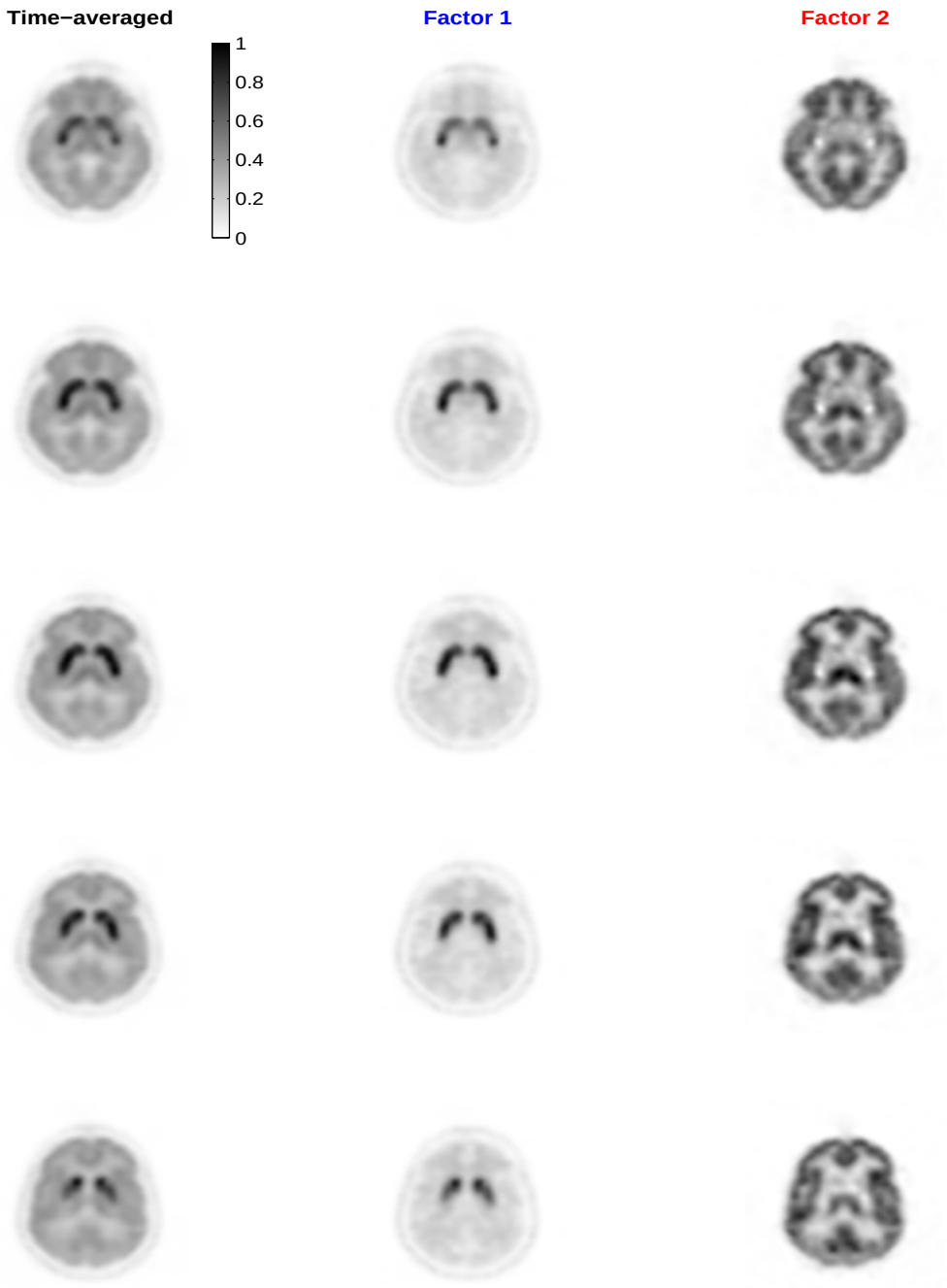

Figure 4.13. Same as figure 4.8 except for a healthy subject (dtbz3) with [24-28] slices. In comparison to figure 4.8, similar uptake pattern (e.g. shape of the two lobes and low background uptake) is observed in the images of the factor 1 volume. Associated FC's are shown in figure 4.10.

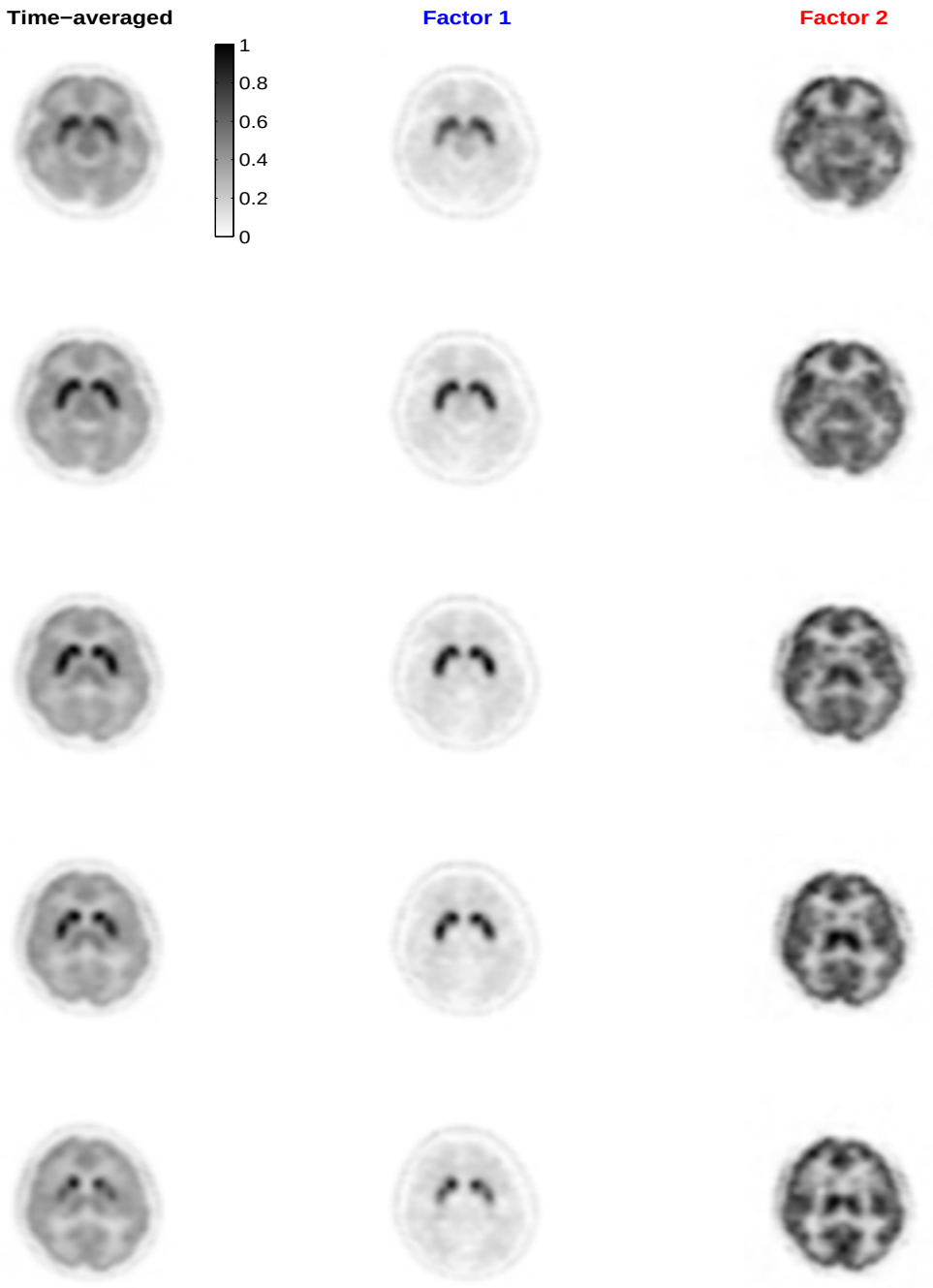

Figure 4.14. Same as figure 4.8 except for a diseased subject (dtbz4) with [23-27] slices. In comparison to figure 4.8, similar uptake pattern (e.g. shape of the two lobes and low background uptake) is observed in the images of the factor 1 volume. Associated FC's are shown in figure 4.10.

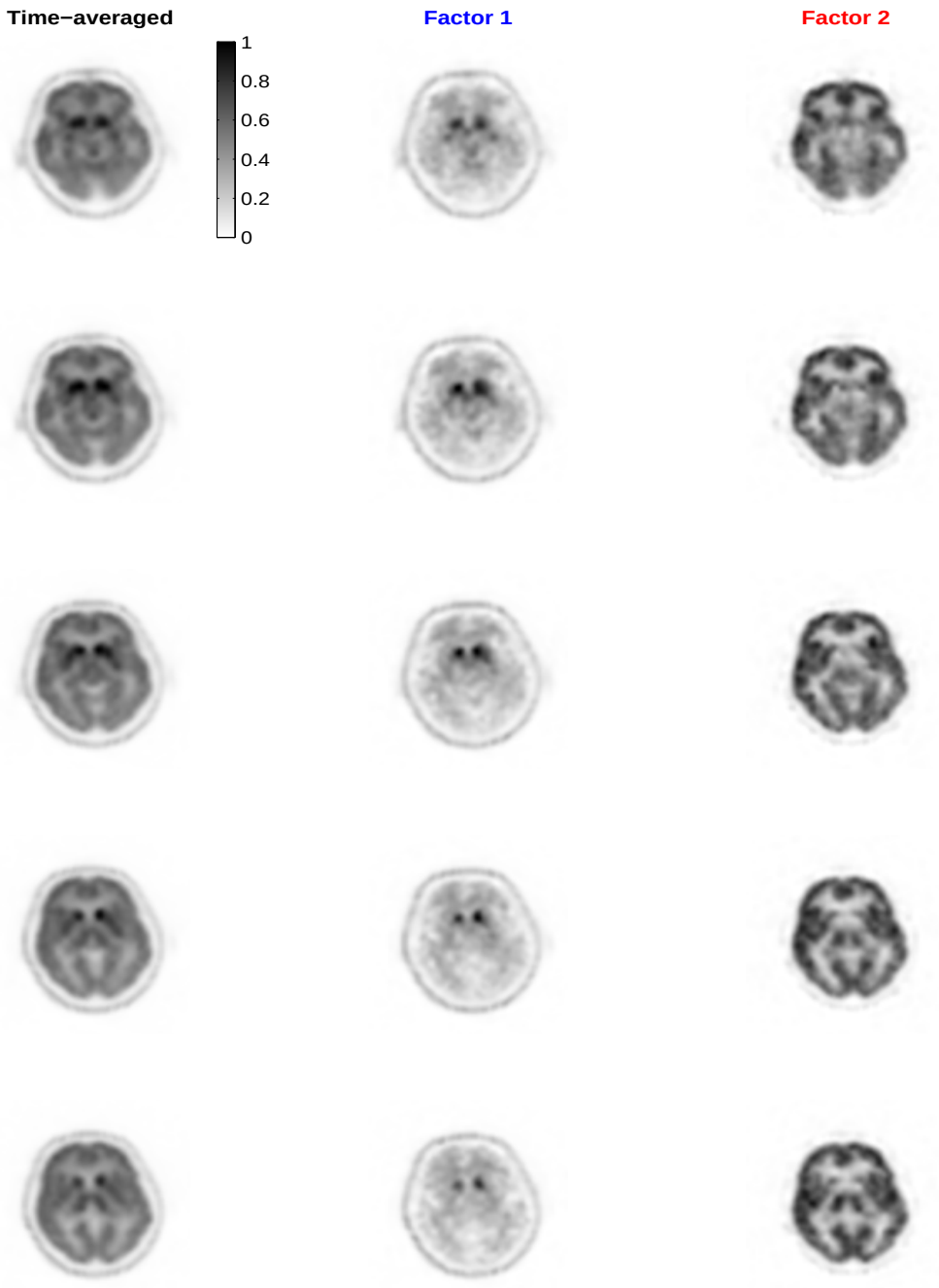

Figure 4.15. Same as figure 4.8 except for a diseased subject (dtbz9) with [23-27] slices. In comparison to figure 4.8, there are clear differences in the uptake pattern (e.g. distortion of the two lobes and the relatively high background uptake) in the images of the factor 1 volume. Associated FC's are shown in figure 4.10.

Figure 4.16. Same as figure 4.8 except for a diseased subject (dtbz10) with [22-26] slices. In comparison to figure 4.8, there are clear differences in the uptake pattern (e.g. distortion of the two lobes and the relatively high background uptake) in the images of the factor 1 volume. Associated FC's are shown in figure 4.10.

4.5 Factor-based Metric

A factor-based metric (or ratio A_1/A_2), defined by equation 2.29 to 2.31, is developed to stratify subjects with early PD from the healthy subjects. For each DTBZ dataset, the FADS result (FV's and FC's) is used to compute the ratio (A_1/A_2). Figure 4.17 shows the ratios for the eight DTBZ datasets, as a function of the threshold value for voxels in the factor 1 volume. For example, voxels with lower value coefficients in the factor 1 volume are deselected by increasing the threshold value. It is clear from the figure that there exists two distinct groups within the population studied. The healthy (X's) and the diseased (O's) groups are well separated by threshold values greater than 0.2. The optimum threshold value might be anywhere between 0.4 and 0.9.

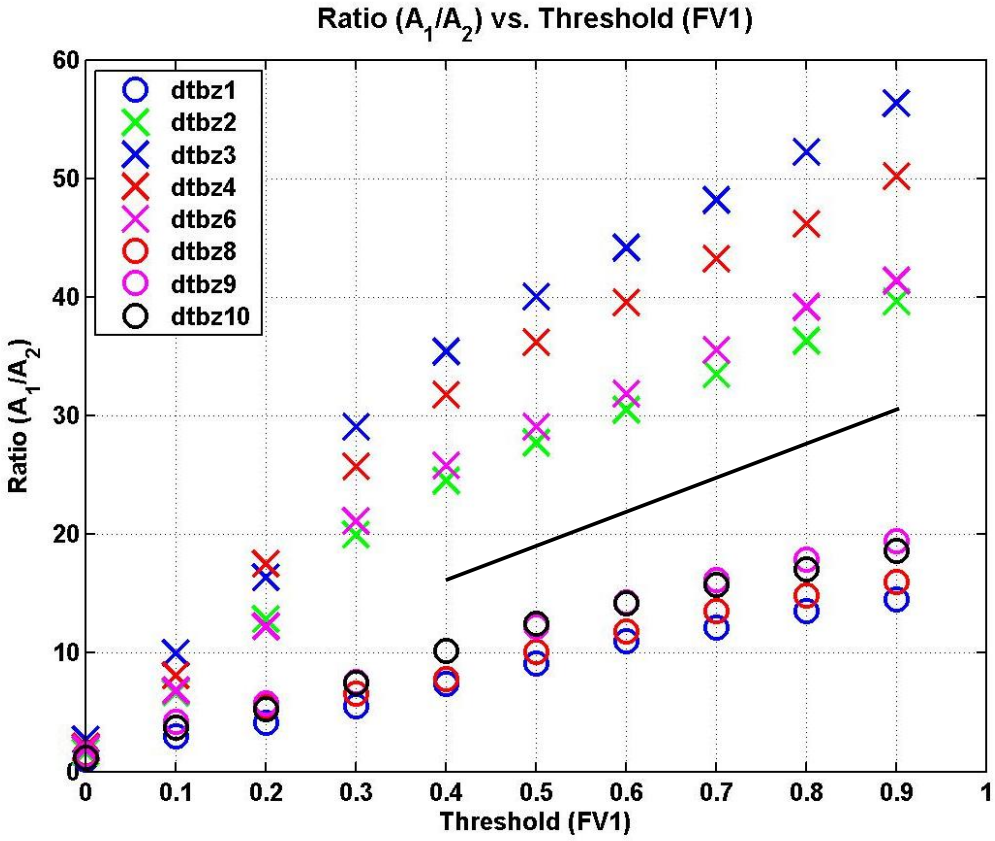

Figure 4.17. Shown is the factor-based metric (A_1/A_2), defined by equation 2.29 to 2.31, as a function of the threshold value for voxels in the factor 1 volume. Notice that the healthy (X's) and the diseased (O's) subjects are clearly separated by threshold values greater than 0.2. The optimum threshold value can be anywhere between 0.4 and 0.9.

The factor-based metric does not make explicit use of factor 2 volumes because there are no unique features in the images of the factor 2 volumes between the healthy and diseased groups. Table 4.1 summarizes the FADS results for the eight DTBZ datasets and shows activity (in MBq), summed over all voxels and averaged over 16 TF's for the dynamic dataset (A_{tot}), for factor 1 (A_{tot1}) and factor 2 (A_{tot2}). Each row in the table represents a DTBZ dataset (dtbz1-4, dtbz6, and dtbz8-10). To compute the activity for each dataset, the extracted FC's and FV's are used from

the eight DTBZ datasets. For each dataset, the sum of activity in the second and third columns is very close to the activity in the first column for all DTBZ datasets. Notice that taking the simple ratio of A_{tot1} to A_{tot2} does not provide reliable metric to stratify the two groups. The factor-based metric for stratifying subjects with and without early PD is compared against the medical diagnosis by clinicians (see the last two columns). The letters D and H represent the diseased and the healthy subjects, respectively. The diagnostic results in the last two columns suggest that the factor-based metric is useful for identifying early PD patients from the healthy subjects.

Table 4.1. The first three columns of this table show the activity (in MBq), summed over all voxels and averaged over 16 TF's for the dynamic dataset (A_{tot}), for factor 1 (A_{tot1}) and factor 2 (A_{tot2}). The extracted FC's and FV's are used from the eight DTBZ datasets to compute the activity. The factor-based metric for stratifying subjects with and without early PD is compared against the medical diagnosis by clinicians (see the last two columns). The letters D and H indicate the diseased and the healthy subjects, respectively. The perfect agreement between factor-based metric and the clinical diagnosis is obtained for the eight DTBZ datasets.

	A_{tot} (MBq)	A_{tot1} (MBq)	A_{tot2} (MBq)	Metric	Diagnosis
dtbz1	21.80	8.62	13.18	D	D
dtbz2	20.13	7.29	12.84	H	H
dtbz3	15.52	9.05	6.47	H	H
dtbz4	17.70	7.21	10.49	H	H
dtbz6	11.39	5.27	6.12	H	H
dtbz8	21.32	11.12	10.20	D	D
dtbz9	21.25	11.29	9.96	D	D
dtbz10	23.53	10.79	12.74	D	D

Chapter 5
Discussion

5.1 Simulation Study

The three-compartment model is used to simulate a dynamic PET dataset. Each dataset consists of three rectangular structures (see figure 3.1) which simulates varying degrees of PVE's. Each compartment is homogeneous and tissue-specific, filled with arbitrarily shaped TAC's. To make the dataset more realistic, Poisson and White noise is used to introduce the quantum and electronic noise to the dynamic datasets. A total of 6 dynamic datasets (case I, II and III for noise-free and noisy datasets) are used for the simulation study, and each dataset consists of 144 $\times$ 144 $\times$ 16 voxels. These simulated datasets are then used to investigate various factors affecting SVD and FADS results, as well as to validate the proposed FADS technique.

Before the FADS technique can be applied to a dataset, the factor number q (i.e. the number of pure underlying kinetics) must be determined. SVD is used to determine the singular values that are well above the level of noise. Figure 3.2 to 3.4 illustrates the SVD results for the three noise-free dynamic datasets (case I, II, and III). In each case, the fourth and higher singular values are all zero, indicating that there are only three principle components (without the presence of noise). The effects of 4 $\times$ 4 and 8 $\times$ 8 VA techniques on the SVD results are negligible for the noise-free datasets. However, the effects of VA techniques are noticeable for the noisy datasets. Figure 3.5 to 3.8 shows that the VA techniques significantly reduces the amount of noise in the dataset (e.g. suppression of singular values corresponding to the noise). Greater noise suppression can be achieved by increasing the size of VA. However, too much VA can have a negative impact on the SVD result because increasing the size of VA has the same effect as increasing the amount of overlap between the compartments. The number of voxels with "pure" TAC's in

the dataset is decreased, and the accurate estimation of factor number q may be difficult in the presence of noise. As a result, the relative contribution of non-dominant principle components gets reduced with the increased amount of structure-overlap. Thus, the VA technique should be applied to the dynamic dataset to improve the image quality and reduce the data size; but, the optimum size of VA depends on the type of dataset and should be determined by trial and error.

If q is not estimated properly then the result of FADS can be meaningless. For example, underestimating q will produce a meaningless result, but over-estimating q can produce a meaningful result (e.g. extra factors may represent noise in the dataset). From our experience, the latter is very unlikely even though it is theoretically possible, and the result often does not make any physical sense. Thus, the operator can easily discard such results and perform the FADS technique again with a different q value. As discussed before, proper estimation of the factor number is a crucial step for the successful application of FADS.

With the appropriate q value, the SVD-based noise reduction technique is applied to the dataset in order to reduce the amount of noise present in the dataset and to improve the image quality (see figure 3.9 and 3.11). For this dataset, the three principle images corresponding to the three largest singular values are expected, and the remaining principle images represent the noise in the dataset (refer to figure 3.10). It is clear that the noise reduced TAC's (dash-dotted curves) are much closer to the true TAC's (solid curves) in figure 3.12. Therefore, the noise reduction technique should always be performed to the dataset prior to running the proposed FADS technique.

The effect and importance of prior information on the FADS results can be seen in figure 3.13 to 3.18. Prior information is used to obtain sample TAC's from the noise-reduced dynamic dataset using the standard ROI method. These sample TAC's are then used to warm start the first stage of the two-stage optimization (in the FADS algorithm) in order to reduce the number of possible solutions and to

obtain the solution that is in close proximity to the true solution. Note that the sample TAC's can contain mixed tissue information and they should not be identical to avoid stalling of the optimization. Without the prior information, the resulting factor images and associated factor curves are quite different from the known factor images and curves (e.g. factor images consist of mixed tissue information and the curves do not represent the pure underlying kinetics). These results suggest that there are several local minima present even for the noise-free cases and the number of local minima will probably increase for the datasets in the presence of noise. Figure 3.19 illustrates the distribution of possible solutions with and without the prior information. For the warm start case, the histogram follows the Gaussian distribution and is skewed to the right. The most likely value of D in this case is approximately 0.025. For the random starting case, the distribution contains at least two normal distributions, and the likely D values are 0.17 and 0.2. The observed D values for the random starting case are much larger than those for the warm starting case. The D values for the random starting case are widely distributed (0.025-0.21). As an example, figure 3.20 clearly shows that most solutions with the random start are far from the known solution. Therefore, the prior information should be always used to obtain sample TAC's from the different physiological structures in the dynamic dataset prior to running the proposed FADS technique. To avoid stalling of the optimization and faster convergence of the technique, the obtained sample TAC's should not be identical.

One major disadvantage of the FADS technique is that the solution is not mathematically unique, and various authors have proposed different techniques to solve this problem but with only limited success. For some datasets, the problem of non-uniqueness is almost non-existent whereas, for other datasets, the problem becomes significant. Unfortunately, FADS techniques proposed by those authors are less practical: they often depends on the type of dataset; they have relatively slow convergence; they require pre-estimation of penalty parameters; some of the meth-

ods are invasive (e.g. requiring blood samples). In contrast, our proposed technique - that utilizes the sample TAC's from the q physiological structures (based on the known information about the dataset) - is robust (see figure 3.27) and produces the solution that is in close proximity to the global minimum (see figure 3.19). In addition, the technique does not require pre-determination of parameters that depend on the type of datasets. However, the proposed technique does not guarantee finding the global minimum for the optimization problem, as is true also for other FADS techniques. Nevertheless, the solution produced by the proposed FADS technique produces good results when compared with the standard ROI method. The technique has further been verified and validated using the simulated phantom study in Chapter 3.

The application of VA technique reduces the dataset size while improving the SNR of the dataset (see Table 3.1). However, it can also have a negative impact on the FADS result if the size of VA is too large. With the larger size of VA, there are reduced number of voxels with "pure" TAC's in the dataset. This has the same effect as increasing the amount of compartment-overlap. When two or more structures are in complete or near-perfect overlap, the proposed FADS technique fails to produce accurate FV's and FC's. Figure 3.22, 3.23, and 3.24 shows the effect of large VA on the FADS result. This example clearly illustrates the potential shortcoming of the VA technique, and the optimum size of VA should be determined by the trial and error.

A critical first step to successful FADS analysis is the proper estimation of factor number q. If its value is chosen inaccurately the FADS technique will probably produce meaningless result. For example, if q-1 value is used for the factor model instead of q then the result is meaningless (see equation 2.4). If q+1 value is used for the factor model instead of q then multiple scenarios can occur: first, the extra factor represents noise in the dataset (see figure 3.25); second, the extra factor is basically the same as one of the other factors (see figure 3.26). From our experience,

improper estimation of q usually produce results that are not physically meaningful (e.g. extracted FC's oscillate). Generally speaking, it is pretty obvious for an operator to discard these results and the operator can perform the FADS analysis again with different q value.

The main computing efficiency of our FADS algorithm arises from the utilization of equation 2.18 and 2.19 to estimate the step sizes for solving the sub-problems (equation 2.10 and 2.11). By converting equation 2.14 into equation 2.17, the computational cost is significantly reduced by avoiding the large matrix multiplication. Without this step the algorithm will take much longer to converge and obtain a solution, rendering the technique less attractive.

5.2 Clinical Study

The proposed FADS algorithm is applied to the eight sets of ^{11}C-DTBZ datasets (4 healthy subjects and 4 diagnosed with early PD). Each dataset is decomposed into FV's and associated FC's assuming a two factor system. One factor represents the striatum tissues, and the other factor represents the non-striatum tissues. Prior to running the FADS algorithm, two sample TAC's are obtained by the conventional ROI method (based on the prior information) in order to warm start the first stage of the dual-stage optimization in the FADS algorithm. The transverse VA technique (2 $\times$ 2 $\times$ 1) is used to improve the SNR of the dataset and to reduce the dataset size. For healthy subjects, the tracer uptake patterns of the striatum tissues in the factor 1 volumes are consistent and comparable between the different datasets. The tracer uptake in the striatum tissues (or two nearly identical lobes) are intense and easily identified from the images of the time-averaged (TA) slices (see figure 4.8, 4.12 to 4.14). In addition, the relative uptakes of the background (or the non-striatum) tissues in the factor 1 volumes are low. For diseased subjects, the tracer uptake patterns of the striatum tissues in the factor 1 volumes are irregular. Manual identification of the striatum tissues from the images of the TA slices is quite difficult

(see figure 4.9, 4.11, 4.15, and 4.16). The relative uptakes of the background (or the non-striatum) tissues in the factor 1 volumes are much higher than those in the factor 1 volumes for the healthy subjects.

There are no distinctive features in the tracer uptake of the non-striatum tissues in factor 2 volumes for either healthy or diseased subjects; however, a clear difference in the shape of the FC's between the two groups is observed (see figure 4.10). For healthy subjects, the area under the factor 1 curve (e.g. associated with the striatum tissues) is much larger than the area under the factor 2 curve (i.e. associated with the non-striatum tissues). For diseased subjects, areas under the factor 1 curves are slightly larger than those under the factor 2 curves. The factor 1 curves within the healthy group are very similar, and the factor 2 curves within the diseased group are also comparable to each other. For factor 1 curves, there are dissimilarities between the two groups. For factor 2 curves, there are similarities between the two groups.

Based on the similarities and dissimilarities in FV's and FC's from the eight DTBZ datasets, a factor based metric (A_1/A_2, defined by equation 2.29-2.31) is developed to automatically stratify early PD patients from the healthy subjects. The proposed metric clearly separates the healthy subjects from the diseased subjects (see figure 4.17). The optimum threshold for the metric can be identified by analyzing a larger number of the DTBZ datasets.

Table 4.1 depicts comparison between the proposed technique and the medical diagnosis performed by clinicians to stratify the early PD patients from the healthy subjects. Even though both methods produce the same diagnostic results, the proposed technique is computationally very efficient (e.g. a single dataset in this study usually takes less than 5 minutes), is semi-automatic, and is operator-independent. The technique does require sample TAC's from q physiological structures (based on the prior information) in the dataset using the standard ROI method. However, the optimization in our technique is insensitive to the starting point and the sample

TAC's are allowed to contain mixed tissue information. The proposed technique has the potential to significantly aid the physicians with the review process (by providing accurate FV's and FC's that represent the striatum and the non-striatum tissues) and thereby can improve the quality of medical diagnosis. Most importantly, our technique allows for researchers and clinicians to perform quantitative analysis on the dynamic studies.

Chapter 6

Conclusion and Future Directions

6.1 Conclusion

In this thesis, the optimization-based factor analysis of dynamic structure (FADS) technique that utilizes the prior information is developed to decompose dynamic PET dataset into parts-based factor volumes (FV's) and associated factor curves (FC's). The technique can greatly simplify the complex datasets and has the potential to significantly aid the review process (performed by physicians). The extracted FV's represent the underlying physiology, and associated FC's describe kinetic information of those FV's. The optimization technique is based on the projected gradient method (PGM) and alternating non-negative least squares (ANLS) method. By combining the two techniques, the solution space is reduced and the convergence speed is improved. Due to the nature of the problem there exist many possible solutions. To minimize the number of possible solutions and obtain a solution close to the global minimum, the first stage of dual-stage optimization is warm started based on the prior information of the dataset. From the simulation study (see Chapter 3), the effect of prior information on the FADS result is investigated (i.e. accuracy of the extracted FC's and FV's). Another important factor for the successful FADS is proper estimation of factor number (q) by SVD. After the proper estimation of the factor number, it is straightforward to obtain q sample TAC's by the traditional ROI method from the q physiological structures in the dynamic dataset. The SVD technique is also used to reduce the amount of noise present in the dataset. In addition, a simple (in-plane) VA technique is used to further improve the SNR of the dataset and increase the convergence speed of the FADS algorithm. The VA technique is very useful for the FADS technique if the optimum size of VA is applied to the dataset. However, it can produce inaccurate FC's and FV's if the size of VA is made too large. In essence, this has the same effect as increasing the amount of structure-

overlap. The optimum size of VA depends on the type of dataset and should be determined by trial and error. With the optimum q value and VA size, the proposed FADS technique with prior information can extract valuable and clinically-relevant information about the underlying physiology (see Chapter 4).

After the validation of the FADS technique using the computer generated phantoms, the technique is applied to the eight DTBZ datasets (4 healthy and 4 diagnosed with early PD). The technique decomposed each dynamic dataset into the two FV's (representing the striatum and the non-striatum tissues) and associated FC's. Similarities in the images of the factor 1 volumes between the healthy subjects (e.g. nearly identical two intense lobes in the center of brain and low non-striatum tissue uptake) are observed. For diseased subjects, inconsistent uptake patterns of the striatum tissues are observed, and relatively high non-striatum tissue uptake in the images of the factor 1 volumes is observed. Similarities and differences in the extracted FC's between the two groups are also observed: for healthy subjects, the area under the factor 1 curve is significantly larger than that under the factor 2 curve; for diseased subjects, the area under the factor 1 curve is slightly larger than that under the factor 2 curve. Based on the extracted FV's and FC's from each dataset, in-house factor-based metric is developed to stratify early PD patients from the healthy subjects. The metric clearly separates the eight subjects into the two groups, and the classification results are in perfect agreement with the clinical diagnosis. The method is computationally robust and operator-independent, and it requires the minimum amount of work. This technique makes the quantitative analysis of the DTBZ datasets possible and has the potential to significantly aid the review process of dynamic datasets performed by physicians.

6.2 Future Directions

In this thesis, the FADS algorithm is applied to dynamic PET ^{11}C-DTBZ datasets, but the technique can be applied to other sequences of dynamic medical images (i.e.

dynamic microPET images and dynamic contrast enhanced MRI images). The proposed technique can be also applied to dynamic PET images / volumes generated with different radio-tracers (e.g. [^{18}F]-Fludeoxyglucose, [^{18}F]-Fluorothymidine and Fluoroazomycin arabinoside). Another 50 DTBZ datasets are also planned to be acquired and will be analyzed with this technique.

In this study, a simple SVD-based noise reduction technique that does not account for the noise characteristics of the dataset - is used. More sophisticated noise model could be employed to reduce the noise in the dataset and then apply the FADS technique to possibly obtain more accurate FV's and associated FC's, representing the underlying physiology.

Finally, the extracted FV's can be fused with Computed Tomography (CT) or Magnetic Resonance Imaging (MRI) images for ease of visualizing the underlying physiology and accurate localization of physiological function for the tissues or organs of interest.

Bibliography

[1] H. Levi, "George von Hevesy memorial lecture. George Hevesy and his concept of radioactive indicators-in retrospect", Eur. J. Nucl. Med. **1**, 3–10 (1976).

[2] H. Schirrmeister, A. Guhlmann, and *et al.*, "Sensitivity in Detecting Osseous Lesions Depends on Anatomic Localization: Planar Bone Scintigraphy Versus ^{18}F PET", **40**, 1623–1629 (1999).

[3] M. Di Carli and V. Murthy, "Cardiac PET/CT for the Evaluation of Known or Suspected Coronary Artery Disease", RadioGraphics **31**, 1239–1254 (2011).

[4] G. Garcea, S. L. Ong, and G. J. Maddern, "The current role of PET-CT in the characterization of hepatobiliary malignancies", HPB **11** (2009).

[5] M. Broome, "Thyroid scintigraphy in hyperthyroidism", Clin. Tech. Small. Anim. Pract. **21**, 10–16 (2006).

[6] H. A. Ziessman, J. P. O'Malley, and J. H. Thrall, *Nuclear Medicine*, 3rd edition (Mosby) (2006).

[7] R. A. Powsner and E. R. Powsner, *Essential Nuclear Medicine Physics*, 2nd edition (Wiley-Blackwell) (2006).

[8] G. H. Knoll, *Radiation Detection and Measurement* (John Wiley & Sons) (1999).

[9] G. B. Saha, *Basics of PET Imaging: Physics, Chemistry, and Regulations*, 2nd edition (Springer) (2010).

[10] D. L. Bailey, D. W. Townsend, P. Valk, and M. N. Maisey, eds., *Positron Emission Tomography: Basic Sciences*, 1st edition (Springer) (2005).

[11] H. Zaidi, *Quantitative Analysis in Nuclear Medicine Imaging*, 1st edition (Springer) (2006).

[12] P. Grangeat and J. Amans, *Three-Dimensional Image Reconstruction in Radiology and Nuclear Medicine*, 1st edition (Springer) (1996).

[13] D. Barber, "The use of principal components in the quantitative analysis of gamma camera dynamic studies", Phys. Med. Biol. **25**, 283 (1980).

[14] J. P. Bazin and R. D. Paola, "Advances in factor analysis application in dynamic function studies", Nucl. Med. Biol. **I**, 35–38 (1982).

[15] J. P. Cavailloles, A. Bazin, H. Capderou, J. L. Valette, and R. D. Paola, "Automated processing of first-pass radionuclide angiocardiography by factor analysis of dynamic structures", Nucl. Med. Comm. **8**, 375–387 (1987).

[16] P. Schmidlin, "Quantitative evaluation and imaging of functions using pattern recognition methods", Phys. Med. Biol. **24**, 385 (1979).

[17] R. Di Paola, J. Bazin, F. Aubry, A. Aurengo, F. Cavailloles, J. Herry, and E. Kahn, "Handling of dynamic sequences in nuclear medicine", IEEE Trans. Nucl. Sci. **29**, 1310–1321 (1982).

[18] A. Houston, "The effect of apex-finding errors on factor images obtained from factor analysis and oblique transformation (nuclear medicine)", Phys. Med. Biol. **29**, 1109 (1984).

[19] A. Houston and K. Nijran, "Constraint problems in factor analysis of dynamic structures in nuclear medicine", in *Image Processing and its Applications, 1989., Third International Conference on*, 333–337 (IET) (1989).

[20] M. Samal, H. Karny, H. Surova, E. Penicka, E. Marikova, and Z. Dienstbier, "On the existence of an unambiguous solution in factor analysis of dynamic studies", Phys. Med. Biol. **34**, 223–238 (1989).

[21] G. E. Fakhri, A. Sitek, B. Guerin, M. F. Kijewski, M. F. Carli, and S. C. Moore, "Quantitative dynamic cardiac 82Rb-PET imaging using generalized factor and compartment analysis", J. Nucl. Med. **46**, 1264–1271 (2005).

[22] K. Nijran and D. Barber, "Towards automatic analysis of dynamic radionuclide studies using principal-components factor analysis", Phys. Med. Biol. **30**, 1315 (1985).

[23] K. Nijran and D. Barber, "Factor analysis of dynamic function studies using a priori physiological information (nuclear medicine)", Phys. Med. Biol. **31**, 1107 (1986).

[24] J. Buvat, H. Benali, F. Frouin, J. Basin, and R. D. Paola, "Target apex-seeking in factor analysis of medical image sequences", Phys. Med. Biol. **38**, 123 (1993).

[25] I. T. Jolliffe, *Principle Component Analysis*, 2nd edition (Springer) (2002).

[26] W. H. Press, S. A. Teukolsky, W. T. Vetterling, and B. P. Flannery, *NUMERICAL RECIPES IN C: The Art of Scientific Computing*, 2nd edition (Cambridge) (1992).

[27] F. Pedersen, M. Bergstrom, E. Bengtsson, and B. Langstrom, "Principle component analysis of dynamic positron emission tomography images", Eur. J. Nucl. Med. **21**, 1285–92 (1994).

[28] A. Sitek, G. Gullberg, and R. Huesman, "Correction for ambiguous solutions in factor analysis using a penalized least squares objective", IEEE Trans. Med. Imag. **21**, 216–225 (2002).

[29] A. Sitek, E. Di Bella, and G. Gullberg, "Factor analysis with a priori knowledge-application in dynamic cardiac SPECT", Phys. Med. Biol. **45**, 2619 (2000).

[30] A. Sitek, E. DiBella, and G. Gullberg, "An improved factor analysis method for cardiac dynamic SPECT studies by using a priori information", in *Nuclear Science Symposium, 1999. Conference Record. 1999 IEEE*, volume 2, 1014–1016 (IEEE) (1999).

[31] M. Nakamura, Y. Suzuki, and S. Kobayashi, "A method for recovering physiological components from dynamic radionuclide images using the maximum entropy principle: a numerical investigation", IEEE Trans. Biomed. Eng. **36**, 906–917 (1989).

[32] A. Sitek, E. Di Bella, and G. Gullberg, "An unique factor analysis of dynamic SPECT imaging using maximum entropy principle", in *Nuclear Science Symposium, 1998. Conference Record. 1998 IEEE*, volume 3, 1776–1780 (IEEE) (1998).

[33] K. Sasaki, S. Kawata, and S. Minami, "Constrained nonlinear method for estimating component spectra from multicomponent mixtures", Appl. Opt. **22**, 3599–3603 (1983).

[34] K. Sasaki, S. Kawata, and S. Minami, "Estimation of component spectral curves from unknown mixture spectra", Appl. Opt. **23**, 1955–1959 (1984).

[35] C. Schiepers, C. K. Hoh, J. Nuyts, H. M. Wu, M. E. Phelps, and M. Dahlbom, "Factor analysis in prostate cancer: delineation of organ structures and automatic generation of in-and output functions", IEEE Trans. Nucl. Sci. **49**, 2338–2343 (2002).

[36] M. A. Macleod and A. S. Houston, "Factor analysis of dynamic structures (FADS) in the diagnosis of renal disease", Eur. J. Nucl. Med. **15**, 601–604 (1989).

[37] B. E. Oppenheim and C. R. Appledorn, "Functional renal imaging through factor analysis", J. Nucl. Med. **22** (1981).

[38] A. S. Houston and W. F. D. Sampson, "A quantitative comparison of some FADS methods in renal dynamic studies using simulated and phantom data", Phys. Med. Biol. **42**, 199–217 (1997).

[39] F. Cavailloles, J. P. Bazin, and R. Di Paola, "Factor analysis in gated cardiac studies", J. Nucl. Med. **25**, 1067 (1984).

[40] H. M. Wu, C. K. Hoh, Y. Choi, H. R. Schelbert, R. A. Hawkins, M. E. Phelps, and S. C. Huang, "Factor analysis for extraction of blood time-activity curves in dynamic FDG-PET studies", J. Nucl. Med. **36**, 1714–1722 (1995).

[41] C. Billotey, A. Aurengo, Y. Najean, E. Sarfati, J. L. MORETTI, M. E. TOUBERT, and J. D. RAIN, "Identifying abnormal parathyroid glands in the thyroid uptake area using technetium-99m-sestamibi and factor analysis of dynamic structures", (1994).

[42] P. C. Gillette and J. L. Koenig, "Noise Reduction via Factor Analysis in FT-IR Spectra", Appl. Spectrosc. **36** (1982).

[43] H. M. Wu, S. C. Huang, V. Allada, P. J. Wolfenden, H. R. Schelben, M. E. Phelps, and C. K. Hoh, "Derivation of input function from FDG-PET studies in small hearts", J. Nucl. Med. **37**, 1717 (1996).

[44] M. Bentourkia, D. Lapointe, V. Selivanov, I. Buvat, and R. Leconte, "Determination of blood curve and tissue uptake from left ventricle using FADS in rat FDG-PET studies", in *Nuclear Science Symposium, 1999. Conference Record. 1999 IEEE*, volume 2, 1124–1127 (IEEE) (1999).

[45] J. Kim, P. Herrero, T. Sharp, R. Laforest, D. J. Rowland, Y. C. Tai, J. S.

Lewis, and M. J. Welch, "Minimally invasive method of determining blood input function from PET images in rodents", J. Nucl. Med. **47**, 330 (2006).

[46] R. Laforest, T. L. Sharp, J. A. Engelbach, N. M. Fettig, P. Herrero, J. Kim, J. S. Lewis, D. J. Rowland, Y. C. Tai, and M. J. Welch, "Measurement of input functions in rodents: challenges and solutions", Nucl. Med. Biol. **32**, 679–685 (2005).

[47] H. Wu, C. Hoh, D. Buxton, W. Kuhle, H. Schelbert, Y. Choi, R. Hawkins, M. Phelps, and S. Huang, "Quantification of myocardial blood flow using dynamic nitrogen-13-ammonia PET studies and factor analysis of dynamic structures", J. Nucl. Med. **36**, 2087 (1995).

[48] G. El Fakhri, A. Sitek, R. E. Zimmerman, and J. Ouyang, "Generalized five-dimensional dynamic and spectral factor analysis", Med. Phys. **33**, 1016 (2006).

[49] Y. Su, M. J. Welch, and K. I. Shoghi, "The application of maximum likelihood factor analysis (MLFA) with uniqueness constraints on dynamic cardiac microPET data", Phys. Med. Biol. **52**, 2313 (2007).

[50] P. Paatero and U. Tapper, "Positive matrix factorization: A non-negative factor model with optimal utilization of error estimates of data values", Environmetrics **5**, 111–126 (1994).

[51] D. D. Lee and H. S. Seung, "Algorithms for non-negative matrix factorization", Advances in neural information processing systems **13** (2001).

[52] M. W. Berry, M. Browne, A. N. Langville, V. P. Pauca, and R. J. Plemmons, "Algorithms and applications for approximate nonnegative matrix factorization", Computational Statistics & Data Analysis **52**, 155–173 (2007).

[53] C. J. Lin, "Projected gradient methods for nonnegative matrix factorization", Neural Computation **19**, 2756–2779 (2007).

[54] P. Hoyer, "Non-negative matrix factorization with sparseness constraints", The Journal of Machine Learning Research **5**, 1457–1469 (2004).

[55] R. Bro and S. De Jong, "A fast non-negativity-constrained least squares algorithm", J. Chemom. **11**, 393–401 (1997).

[56] M. Chu, F. Diele, R. Plemmons, and S. Ragni, "Optimally, computation, and interpretation of nonnegative matrix factorizations", SIAM JOURNAL OF MATRIX ANALYSIS (2004).

[57] P. H. Calamai and J. J. More, "Projected gradient methods for linearly constrained problems", Math. Program. **39**, 93–116 (1987).

[58] D. P. Bertsekas, *Nonlinear Programming*, 2nd edition (Athena Scientific) (1999).

[59] C. Lin and J. J. More, "Newton's method for large-scale bound constrained problems", SIAM Journal on Optimization **9**, 1100–1127 (1999).

[60] N. I. Bohnen, R. L. Albin, R. A. Koeppe, K. A. Wernette, M. R. Kilbourn, S. Minoshima, and K. A. Frey, "Positron emission tomography of monoaminergic vesicular binding in aging and Parkinson disease", J. Cereb. Blood Flow Metab. **26**, 1198–1212 (2006).

[61] F. S. and E. R., "Unified Parkinson's disease rating scale", Technical Report, , Florham Park, NJ: Macmillan Healthcare Information, in: *Recent developments in parkinson's disease* (Fahn S, Marsden CD, Calne DB, Goldstein M, eds).

[62] G. L. Chan, J. E. Holden, and *et al*, "Reproducibility studies with 11C-DTBZ, a monoamine vesicular transporter inhibitor in healthy human subjects", J. Nucl. Med. **40** (1999).

[63] C. S. Lee, A. Samii, and *et al*, "In vivo positron emission tomographic evidence for compensatory changes in presynaptic dopaminergic nerve terminals in Parkinson's disease", Ann. Neurol. , 493–503 (2000).

[64] W. R. Martin, M. Wieler, J. Stoessl, and M. Schulzer, "Dihydrotetrabenazine Positron Emission Tomography Imaging in Early, Untreated Parkinson's Disease", Ann. Neurol. **63**, 388–94 (2008).

APPENDIX

Neuroanatomical Correlates of Dopamine Responsive and Non-responsible Galt and Balance Impairment in the Parkinson's Disease

This appendix contains the following documents:

1. INFORMATION SHEET – CONTROL SUBJECTS
2. INFORMATION SHEET – PARKINSON'S PATIENTS
3. CONSENT FORM
4. ETHICS APPROVAL FORM – DELEGATED REVIEW
5. Re-Approval Form

INFORMATION SHEET – CONTROL SUBJECTS

TITLE: Neuroanatomical Correlates of Gait and Balance Impairment in Parkinson's Disease

PRINCIPAL INVESTIGATOR: W.R. Wayne Martin, MD, FRCPC
CO-INVESTIGATORS: Marguerite Wieler, BScPT, MSc 780-735-8809
Richard Camicioli, MD, FRCPC 780-735-8805

PURPOSE:
You are being asked to participate in a research study to further our understanding of the changes that occur in walking, balance and the brain in Parkinson's disease (PD). The study involves clinical evaluations, magnetic resonance (MR) brain scans and a positron emission tomography (PET) scan. AS someone without PD, you will act as a control subject.

PROCEDURES:
This study involves visits to the Movement Disorders Clinic at the Glenrose Rehabilitation Hospital, the *Peter S. Allen MR Research Centre* at the University Hospital and at the *Cross Cancer Institute* at the University of Alberta.

***Visits at the Glenrose Rehabilitation Hospital*:**
At this visit:

- Tests of your movements will be done.
- Tests of your memory, thinking and concentration will be completed.
- Your walking will be assessed. You will walk on a mat that detects many things about how you walk.
- Your balance will be tested on a special machine. You will be asked to stand on a special platform that can move. You will wear a harness to make sure you don't fall.

This visit will last about 1.5 hours

***Visit at the Peter S. Allen MR Research Centre*:**
Within one month of the visits to the Clinic, you will be asked to go to the *Peter S. Allen MR Research Centre* at the University of Alberta Hospital. You will have several different MR scans done on two different MR machines. During these scans, you will be asked to lie quietly on your back within the MR machine. Your head will be carefully positioned with the aid of a low power laser which projects a light beam on the side of your head. Your head will then be gently restrained to limit head movement during the scan. During the scan itself, you will be asked to remain quiet, and to keep your head as still as possible. Each MR scan will last from about 45-60 minutes. The total time involved will be about 2 hours.

***Visit at the Cross Cancer Institute*:**
Within one month of the visits to the Clinic, you will be asked to go to the PET scan facility at the *Cross Cancer Institute*. The PET scan will be used to determine the activity of the dopamine nerve cells affected in PD. A test substance labeled with a tiny amount of radioactivity will be

infused into your arm. The PET scanner detects this radioactivity in the brain. The test substance to be administered is radioactively labeled tetrabenazine. This chemical labels the storage area for dopamine deep in the brain. Dopamine is a natural substance in the brain that certain nerve cells use to send messages. Dopamine is reduced in PD.

POSSIBLE BENEFITS:
We do not expect a direct benefit to you from this study. However, we do expect improved knowledge regarding PD that may ultimately help in the development of more effective treatments.

POSSIBLE RISKS:
During the tests of your balance, you may lose your balance. A harness will keep you from falling.

There are no known risks associated with the MR procedure. Some people find it uncomfortable to lie on their back in the enclosed space of the MR scanner for the time required. Sometimes claustrophobia is a problem. Dr. Martin may prescribe a mild, temporary anti-anxiety pill (Ativan) to help you relax during the scan, if you wish. You may need someone to drive you home after the scans, if you take the Ativan. You will be asked to sign a separate consent form for the MR which lists conditions that might exclude someone from participating in this test.

There is a small amount of radiation exposure involved with the PET scan. The long-term effects of exposure to this amount of radiation are unknown. The radiation doses in this study are comparable to those from routine brain scans such as CT. They are much lower than the yearly dose permitted to radiation workers. There may be some discomfort, bruising, or inflammation at the site of the intravenous lines inserted for the PET scans.

CONFIDENTIALITY:
Personal records relating to this study will be kept by Dr, Martin. Only staff involved in the study will have access to them. The Health Research Ethics Board, representatives of the Michael J. Fox Foundation (study sponsor) or Health Canada may see them, if necessary. You are not named in any report published about this study. In order for the PET scan to be done, you must be registered at the Cross Cancer Institute. All information will be treated with the confidentiality of a medical record. You will **not** be entered into the Cancer Registry.

You may withdraw from this study at any time. Your medical care will not be affected in any way. If you do not take part in the study, or if the study is discontinued, your medical care will not be affected. You will be informed if any knowledge gained from this study becomes available which could affect your decision to continue in the study.

If you have any questions or concerns regarding this project please contact:

- Dr. Wayne Martin, Movement Disorder Clinic, 735-8805
- Marguerite Wieler, Movement Disorders Clinic, 735-8809

If you have concerns about this research please contact Alberta Health Services Patient Relations Office for at 1-866-931-2931.

INFORMATION SHEET – PARKINSON'S PATIENTS

TITLE: Neuroanatomical Correlates of Gait and Balance Impairment in Parkinson's Disease

PRINCIPAL INVESTIGATOR: W.R. Wayne Martin, MD, FRCPC 780-735-8805
CO-INVESTIGATORS: Marguerite Wieler, BScPT, MSc 780-735-8809
Richard Camicioli, MD, FRCPC 780-735-8805

PURPOSE:

You are being asked to participate in a research study to further our understanding of the changes that occur in walking, balance and the brain in Parkinson's disease (PD). The study involves clinical evaluations, magnetic resonance (MR) brain scans and a positron emission tomography (PET) scan.

PROCEDURES:

This study involves visits to the Movement Disorders Clinic at the Glenrose Rehabilitation Hospital, the *Peter S. Allen MR Research Centre* at the University Hospital and at the *Cross Cancer Institute* at the University of Alberta.

The drug(s) you take for PD may change your walking and balance. The walking and balance exams will be done twice. The first exam will be done with you taking your regular drug(s). The second exam will be 12 hours after the drug(s) have been stopped.

Visits at the Glenrose Rehabilitation Hospital:

Visit 1: At this visit:

- Your PD symptoms will be assessed and questionnaires about your quality of life will be completed.
- Tests of your mood, memory, thinking and concentration will be done.
- Your walking will be assessed. You will walk on a mat that detects many things about how you walk.
- Your balance will be tested on a special machine. You will be asked to stand on a special platform that can move. You will wear a harness to make sure you don't fall.

This visit will last about 1.5 hours

Visit 2: This visit will be done 12 hours after all PD drug(s) have been stopped.

- Your walking will be assessed again. You will walk on a mat that detects information about how you walk.
- Your balance will be tested again on a special machine. You will be asked to stand on a special platform that can move. You will wear a harness to make sure you don't fall.

This visit will last about 1 hour.

Visit at the Peter S. Allen MR Research Centre:

Within one month of the visits to the Clinic, you will be asked to go to the *Peter S. Allen MR Research Centre* at the University of Alberta Hospital. You will have several different MR scans done on two different MR machines. During these scans, you will be asked to lie quietly on your back within the MR machine. Your head will be carefully positioned with the aid of a low power laser which projects a light beam on the side of your head. Your head will then be gently restrained to limit head movement during the scan. During the scan itself, you will be asked to remain quiet, and to keep your head as still as possible. Each MR scan will last from about 45-60 minutes. The total time involved will be about 2 hours. You will NOT be asked to stop your PD drug(s) for these scans.

Visit at the Cross Cancer Institute:

Within one month of the visits to the Clinic, you will be asked to go to the PET scan facility at the *Cross Cancer Institute*. The PET scan will be used to determine the activity of the dopamine nerve cells affected in PD. You will be asked not to take your PD medications for 12 hours before the PET scan. A test substance labeled with a tiny amount of radioactivity will be infused into your arm. The PET scanner detects this radioactivity in the brain. The test substance to be administered is radioactively labeled tetrabenazine. This chemical labels the storage area for dopamine deep in the brain. Dopamine is a natural substance in the brain that certain nerve cells use to send messages. Dopamine is reduced in PD.

POSSIBLE BENEFITS:
We do not expect a direct benefit to you from this study. However, we do expect improved knowledge regarding PD that may ultimately help in the development of more effective treatments.

POSSIBLE RISKS:
You will likely experience a temporary return of your PD symptoms when the PD drug(s) is stopped. These will improve when you take your next dose.

During the tests of your balance, you may lose your balance. A harness will keep you from falling.

There are no known risks associated with MR scans. Some people find it uncomfortable to lie on their back in the enclosed space of the MR scanner for the time required. Sometimes claustrophobia is a problem. Dr. Martin may prescribe a mild, temporary anti-anxiety pill (Ativan) to help you relax during the scan, if you wish. You may need someone to drive you home after the scans, if you take the Ativan. You will be asked to sign a separate consent form for the MR which lists conditions that might exclude someone from participating in this test.

There is a small amount of radiation exposure involved with the PET scan. The long-term effects of exposure to this amount of radiation are unknown. The radiation doses in this study are comparable to those from routine brain scans such as CT. They are much lower than the yearly dose permitted to radiation workers. There may be some discomfort, bruising, or inflammation at the site of the intravenous lines inserted for the PET scans.

CONFIDENTIALITY:

Personal records relating to this study will be kept by Dr, Martin. Only staff involved in the study will have access to them. The Health Research Ethics Board representatives of the Michael J. Fox Foundation (study sponsor) or Health Canada may see them, if necessary. You are not named in any report published about this study. In order for the PET scan to be done, you must be registered at the Cross Cancer Institute. All information will be treated with the confidentiality of a medical record. You will **not** be entered into the Cancer Registry.

You may withdraw from this study at any time. Your medical care will not be affected in any way. If you do not take part in the study, or if the study is discontinued, your medical care will not be affected. You will be informed if any knowledge gained from this study becomes available which could affect your decision to continue in the study.

If you have any questions or concerns regarding this project please contact:

- Dr. Wayne Martin, Movement Disorder Clinic, 735-8805
- Marguerite Wieler, Movement Disorders Clinic, 735-8809

If you have concerns about this research please contact Alberta Health Services Patient Relations Office for at 1-866-931-2931.

CONSENT FORM

TITLE: Neuroanatomical Correlates of Gait and Balance Impairment in Parkinson's Disease

PRINCIPAL INVESTIGATOR: W.R. Wayne Martin, MD, FRCPC 780-735-8805
CO-INVESTIGATORS: Marguerite Wieler, BScPT, MSc 780-735-8809
Richard Camicioli, MD, FRCPC 780-735-8805

	Yes	No
Do you understand that you have been asked to be in a research study?	☐	☐
Have you read and received a copy of the attached Information Sheet?	☐	☐
Do you understand the risks and benefits involved in taking part in this study?	☐	☐
Have you had an opportunity to ask questions and discuss this study?	☐	☐
Do you understand that you are free to withdraw from the study at any time, without having to give reason and without affecting your future medical care?	☐	☐
Has the issue of confidentiality been explained to you?	☐	☐
Do you want the investigator to inform your family doctor that you are participating in this research study?	☐	☐

Who explained this study to you? _____

	Yes	No
I agree to take part in this study	☐	☐

Signature: _____

Printed Name: _____

Date: _____

I believe that the person signing this form understands what is involved in the study and voluntarily agrees to participate. They will receive a signed and dated copy of this consent form.

_____ Date: _____
Signature of Investigator (or Designee)

Health Research Ethics Board

308 Campus Tower
University of Alberta, Edmonton, AB T6G 1K8
p. 780.492.9724 (Biomedical Panel)
p. 780.492.0302 (Health Panel)
p. 780.492.0459
p. 780.492.0839
f. 780.492.7808

ETHICS APPROVAL FORM - DELEGATED REVIEW

Date:	December 21, 2009			
Principal Investigator:	Wayne Martin			
Study ID:	Pro00010566			
Study Title:	Neuroanatomical Correlates of Dopamine Responsive and Non-responsive Gait and Balance Impairment in Parkinson's Disease			
Approval Expiry Date:	December 14, 2010			
Date of Informed Consent:	Approval Date 12/15/2009 12/15/2009 12/15/2009		Approved Document Control Information letter.doc PD Information letter.doc Consent.doc	
Sponsor/Funding Agency	11/5/09	11/5/09	ID00000811	Michael J Fox Foundation

Thank you and your colleagues for submitting the above study to the Health Research Ethics Board (Biomedical Panel). The undated protocol involved in this project has been found to be acceptable within the limitations of human experimentation. The informed consent documents referenced above (all dated simply November 2009) are approved with the proviso that you delete the blank page 3 of the control ICF. There are no outstanding ethical issues and the study is approved.

The ethics approval is valid until December 14, 2010. A renewal report must be submitted next year prior to the expiry of this approval if your study still requires ethics approval. You will receive electronic reminders at 45, 30, 15 and 1 day(s) prior to the expiry date. If you do not renew on or before that date, you will have to re-submit an ethics application.

For studies where investigators must obtain informed consent, signed copies of the consent form must be retained, as should all study related documents, so as to be available to the HREB on request. They should be kept for the duration of the project and for at least seven years following its completion. In the case of clinical trials approved under Division 5 of the Food and Drug Regulations of Health Canada, study records must be retained for 25 years.

Approval by the Health Research Ethics Board does not encompass authorization to access the patients, staff or resources of Alberta Health Services or other local health care institutions for the purposes of research. Enquiries regarding AHS administrative approval, and operational approval for areas impacted by research, should be directed to the AHS Research Administration office, #1800 College Plaza, phone 407-1372.
Sincerely,

J. Stephen Bamforth, MD
Associate Chair, Health Research Ethics Board (Biomedical Panel)

Note: This correspondence includes an electronic signature (validation and approval via an online system).

Health Research Ethics Board

308 Campus Tower
University of Alberta, Edmonton, AB T6G 1K8
p. 780.492.9724 (Biomedical Panel)
p. 780.492.0802 (Health Panel)
p. 780.492.0459
p. 780.492.0839
f. 780.492.9429

Re-Approval Form

Date: December 9, 2011

Principal Investigator: Wayne Martin

Study ID: Pro00010566

Study Title: **Neuroanatomical Correlates of Dopamine Responsive and Non-responsive Gait and Balance Impairment in Parkinson's Disease**

Approval Expiry Date: December 12, 2012

Sponsor/Funding Agency: Michael J Fox Foundation

The Health Research Ethics Board - Biomedical Panel has reviewed the renewal request and file for this project and found it to be acceptable within the limitations of human experimentation.

The re-approval for the study as presented is valid for another year. It may be extended following completion of the annual renewal request. Beginning 45 days prior to expiration, you will receive notices that the study is about to expire. Once the study has expired you will have to resubmit. Any proposed changes to the study must be submitted to the HREB for approval prior to implementation.

All study-related documents should be retained so as to be available to the HREB on request. They should be kept for the duration of the project and for at least five years following study completion. In the case of clinical trials approved under Division 5 of the Food and Drug regulations of Health Canada, study records must be retained for 25 years.

Sincerely,

S.K.M. Kimber, MD, FRCPC
Chair, HREB Biomedical

Note: This correspondence includes an electronic signature (validation and approval via an online system).